Die approbierte Originalversion dieser Dissertation ist an der Hauptbibliothek der Technischen Universität Wien aufgestellt (http://www.ub.tuwien.ac.at).

The approved original version of this thesis is available at the main library of the Vienna University of Technology (http://www.ub.tuwien.ac.at/englweb/).

D I S S E R T A T I O N

Modeling and Simulation of Highly Porous Open Cell Structures – Elasto-Plasticity and Localization *versus* Disorder and Defects

ausgeführt zum Zwecke der Erlangung des akademischen Grades eines Doktors der technischen Wissenschaften unter der Leitung von

Univ.Doz. Dipl.-Ing. Dr.techn. Heinz Pettermann

E317

Institut für Leichtbau und Struktur–Biomechanik

eingereicht an der

Technischen Universität Wien

Fakultät für Maschinenwesen und Betriebswissenschaften

von

Dipl.-Ing. Mathias H. Luxner

9426722

Margaretenstraße 67/2/28

A-1050 Wien

mathias@luxner.cc

TU VIENNA

TECHNISCHE UNIVERSITÄT WIEN

VIENNA UNIVERSITY OF TECHNOLOGY

Wien, im Juni 2006 Mathias H. Luxner

Kurzfassung

Zellulare Materialien stellen eine besondere Klasse von Werkstoffen dar. Sie treten häufig in der Natur auf (Knochen, Holz, Kork, etc.), finden sich aber auch in vielen technischen Anwendungen wieder (Kerne von Sandwichplatten, Aufprallschutz, Verpackung, usw.). Ihre hervorragenden Eigenschaften wie hohes Energieaufnahmevermögen, gute Formbarkeit und ausgezeichnete Dämmung werden hauptsächlich durch ihre Mikrostruktur bestimmt.

Die Möglichkeit, ihre Eigenschaften, d.h. ihre Mikrostruktur, für bestimmte Einsatzgebiete anzupassen, macht sie in hohem Ausmaß für technische Anwendungen interessant. Speziell ermöglicht der Einsatz von Rapid Prototyping Verfahren die Erzeugung zellularer Strukturen mit maßgeschneiderten mechanischen Eigenschaften. Hierfür ist es unumgänglich das mechanische Verhalten von zellularen Strukturen zu verstehen.

Die vorliegende Arbeit beschäftigt sich mit der numerischen Simulation des mechanischen Verhaltens von regelmäßigen und unregelmäßigen offenzelligen Strukturen. Dabei liegt das Hauptaugenmerk auf Strukturen die mittels des Rapid Prototyping Verfahrens hergestellt werden können. In Kapitel 2 werden verschiedene Ansätze für die Modellierung von offenzelligen Strukturen mittels der Methode der Finiten Elemente dargestellt. Unter Verwendung von Kontinuumselementen und Balkenelementen, mit und ohne einer Anpassung der Steifigkeit im Bereich der Strukturknoten, werden die Strukturen als unendliche und endliche Medien betrachtet. Es werden die linear elastischen Eigenschaften verschiedener Strukturen ermittelt und ein Vergleich zu experimentellen Ergebnissen gezogen.

Unter Berücksichtigung von elastisch–plastischem Verhalten des Grundmaterials, großen Verformungen und Lokalisieren der Deformation werden in Kapitel 3 die Untersuchungen auf das nichtlineare mechanische Verhalten ausgeweitet. Unregelmäßige Strukturen werden

durch zufälliges Verschieben der Strukturknoten erzeugt. Der Einfluss dieser strukturellen Unordnung auf die elastische Anisotropie, das nichtlineare mechanische Verhalten, die Verteilung der mechanischen Energie sowie das Lokalisierungsverhalten wird für endliche Strukturen unter einachsiger Kompression untersucht.

Kapitel 4 widmet sich der Frage welchen Einfluss die Form und die Größe der Strukturen auf ihr mechanisches Verhalten haben. Es wird das nichtlineare Verhalten und das Lokalisieren von quaderförmigen und zylindrischen Strukturen unter einachsigem Druck verglichen.

Aufbauend auf die Erkenntnisse der vorangegangenen Kapitel werden in Kapitel 5 neue offenzellige Strukturen mit vorgegebenen mechanischen Eigenschaften entworfen. Dabei ist das Ziel, Strukturen mit hoher Steifigkeit bei gleichzeitiger geringer elastischer Anisotropie zu entwickeln. Weiters wird das nichtlineare Verhalten der vorgeschlagenen Strukturen unter einachsigem Druck betrachtet und ein Vergleich zu experimentellen Ergebnissen präsentiert.

Zum Abschluß werden in Kapitel 6 die Auswirkungen von Defekten in regelmäßigen und unregelmäßigen offenzelligen Strukturen untersucht. Es werden drei verschiedene Klassen von Defekten, die alle die gleiche Anzahl an fehlenden Stäben aufweisen, in zylindrische Strukturen eingebracht und das nichtlineare mechanische Verhalten unter einachsigem Druck verglichen.

Abstract

Cellular materials are a unique class of materials and can be found in nature (bone, wood, cork, etc.) as well as in engineering applications (in the cores of sandwich panels, crash protection, packaging, etc.). Their excellent properties such as high energy absorption potential, good formability, and excellent insulation capability are mainly determined by their microstructure. The possibility of tailoring their overall properties for certain service conditions by controlling their microstructure makes them highly attractive for engineering applications. In this context the introduction of Rapid Prototyping techniques opens the possibility of building cellular structures with predetermined properties. In addition to the ability to control the production process, an understanding of the mechanical behavior of cellular materials is crucial for the success of the designed material.

In the present thesis numerical simulations regarding the mechanical behavior of regular and irregular open cell structures are carried out with the focus on open cell structures fabricated by Rapid Prototyping. In Chapter 2 several approaches regarding the modelling of open cell structures by means of the Finite Element Method are presented. The structures are treated as infinite and finite media, respectively, employing continuum element based models as well as beam element based models with and without an adaption of stiffness in the vicinity of the vertices. The linear elastic properties of various cell architectures are predicted and a comparison to experimental results is shown.

In Chapter 3 the investigations are extended to the nonlinear behavior of open cell materials, taking into account elastic-plastic bulk material behavior, large strain theory, and deformation localization. Disordered structures are generated by randomly shifting the vertex positions of regular structures. The influence of structural disorder on the elastic

anisotropy, the nonlinear mechanical response, the distribution of the mechanical energy, and the deformation localization is investigated for two different finite structures subjected to uniaxial compression.

The influence of the size and the shape of finite cellular structures on their mechanical response is discussed in Chapter 4. The nonlinear response and the deformation localization mechanisms of cuboidal and cylindrical finite samples subjected to uniaxial compression are compared.

Based on the findings of the previous chapters, new open cell structures with predetermined mechanical properties are introduced in Chapter 5. The design goal is high overall stiffness at low elastic anisotropy. Furthermore, their nonlinear properties are discussed and a comparison to experimental results is presented.

Finally, the effect of defects on the mechanical behavior of regular and disordered open cell structures is investigated in Chapter 6. Three different types of defects, all representing the same amount of missing struts, are introduced to cylindrical samples with varying lattice orientations and their nonlinear mechanical responses under uniaxial compression is compared.

Acknowledgements

This thesis was prepared in the course of my stay at the Institute of Lightweight Design and Structural Biomechanics (ILSB) at the Vienna University of Technology. The funding of the Austrian Science Fund (FWF), grant P15852, is gratefully acknowledged. Additionally, I wish to acknowledge the financial support by the Max–Planck–Society and the Vienna University of Technology during my stay at the Max–Planck–Institute of Colloids and Interfaces, Potsdam, Germany.

I wish to express my sincere gratitude to my advisor Univ.Doz. Dr.tech. H. Pettermann for giving excellent guidance and his valuable and precise comments on my work. I also would like to thank my FWF project manager Ao.Univ.Prof. Dr.mont. J. Stampfl for his assistance and for acting as a co-advisor. Furthermore, I wish to acknowledge the fruitful discussions with Prof. P. Fratzl and the members of his department during my stay at the Max–Planck–Institute of Colloids and Interfaces.

Additionally, I would like to express my gratitude to O.Univ.Prof. Dr.techn. F.G. Rammerstorfer and Ao.Univ.Prof. Dr.techn. H.J. Böhm as heads of the ILSB, as well as all members of the ILSB for creating such a friendly and supportive work environment. Special thanks go to T. Daxner and D.H. Pahr who have contributed to this work in many fruitful discussions. Very special thanks go to the “executive officer of the ILSB”, the ILSB system administrator Ing. G. Schneider, for providing an unique work environment.

Finally, I would like to thank the people who indirectly contributed to this work; Linus Torvalds for initiating the development of the Linux operating System, Bjarne Stroustrup for C++, and all people who share their code and knowledge under the GNU General Public License (GPL).

Contents

Nomenclature

General Abbreviations

FEM	Finite Element Method
RP	Rapid Prototyping
DLP	Digital Light Processing
SLS	Selective Laser Sintering

Structures

BCC	Body Centered Cubic (structure(s))
FCC	Face Centered Cubic (structure(s))
GA	Gibson Ashby (structure(s))
KV	Kelvin (structure(s))
RBCC	Reinforced Body Centered Cubic (structure(s))
RSC	Reinforced Simple Cubic (structure(s))
SC	Simple Cubic (structure(s))
WP	Weaire Phelan (structure(s))

Symbols

$\bar{E}_{\mathrm{cyl}}$	Average Young's modulus in axial direction of cylindrical samples
E^*	Effective Young's modulus

$E^*_{\max}$	Maximum effective Young's modulus within a structure
$E^*_{\min}$	Minimum effective Young's modulus within a structure
E_{s}	Young's modulus of the bulk material
$\Sigma_{33,\max}$	Maximum macroscopic stress in 3-direction
$\bar{\Sigma}_{33,\max}$	Average maximum macroscopic stress in 3-direction
ε_{33}	Mesoscopic compressive strain in 3-direction
$\bar{\varepsilon}_{33}$	Mesoscopic compressive strain rate in 3-direction
Γ_{33}	Macroscopic compressive strain in 3-direction
$\bar{\Gamma}_{33,\max}$	Average compressive macroscopic strain in 3-direction at maximum macroscopic stress
u_{el}	Strain energy density
u_{pl}	Plastic dissipation energy density
u_{tot}	Total energy density
U_{element}	Total energy within a Finite Element
U_{overall}	Overall work
ρ_{rel}	Relative density
β	Density exponent
δ	Level of disorder
l	Strut length
$\underline{\phi}$	Direction vector
s	Standard deviation
p	Fraction of elements in energy histograms

Chapter 1

Introduction

1.1 Cellular Materials in Nature and Engineering

Cellular materials are widespread in nature and in engineering applications. Their cellular structure gives rise to excellent properties like high energy absorption, good formability, and excellent insulation. Even when the primary use is not mechanical – the mechanical properties are still important. The possibility of tailoring their mechanical properties for certain service conditions makes them a unique class of materials.

Nature is using cellular materials to build plant bodies or skeletons, where certain mechanical properties have to be achieved with a small amount of material. The microstructure of natural cellular materials is adapted to the prevailing service conditions resulting in structures which are mechanically efficient. Wood, cork, and trabecular bone, see Figure 1.1, are typical examples of natural cellular materials [Wainwright, 1982; Elices, 2000; Currey, 2002; Gibson, 2005; Gibson and Ashby, 1999].

Because of their excellent properties, the principles of cellular materials are copied for engineering applications. Man-made cellular materials in the form of polymeric, ceramic, and metallic foams are used for lightweight structures (in the cores of sandwich panels, for instance), crash protection, packaging, filtration, thermal insulation, and substitute

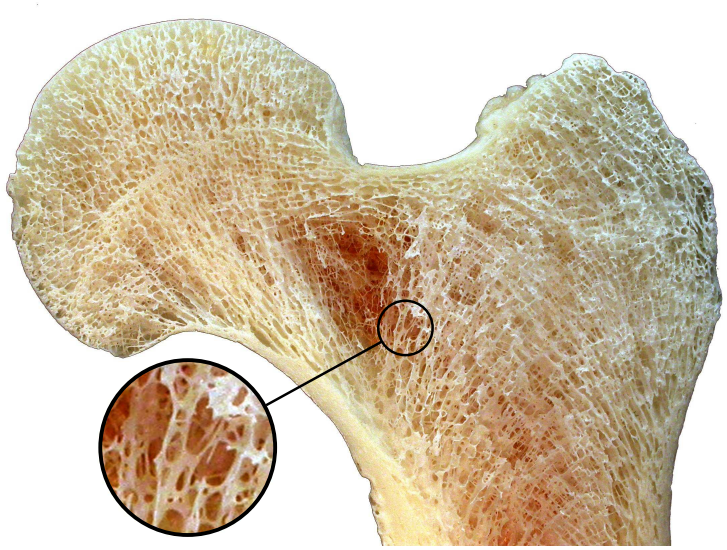

Figure 1.1 Trabecular bone within a human femur as cellular structure.

materials in medical applications. Figure 1.2 shows some typical examples of man-made metallic cellular materials.

Various manufacturing processes for cellular materials have been developed [Banhart, 2001], among which the fabrication by foaming is the most common. However, in the fabrication of man-made cellular materials by foaming it is quite difficult to control the microstructure. Hence, the overall mechanical properties can only be tailored within a certain range.

The introduction of Rapid Prototyping techniques [Jacobs, 1992; Gebhardt, 2000], however, opens the possibility of building cellular structures with exact, predetermined microstructures in high spatial resolution, see Figure 1.3. It opens the possibility of tailoring the mechanical properties of cellular materials to a high degree. This technique may be used either to build cellular materials directly from polymer and metallic bulk materials or to build cellular structures which serve as scaffolds and molds for materials which cannot be handled directly in a Rapid Prototyping process, e.g. ceramics and biological cells. The use of Rapid Prototyping techniques in combination with biodegradeable polymers is gaining increasing importance in the field of medical engineering. Porous scaffolds are designed

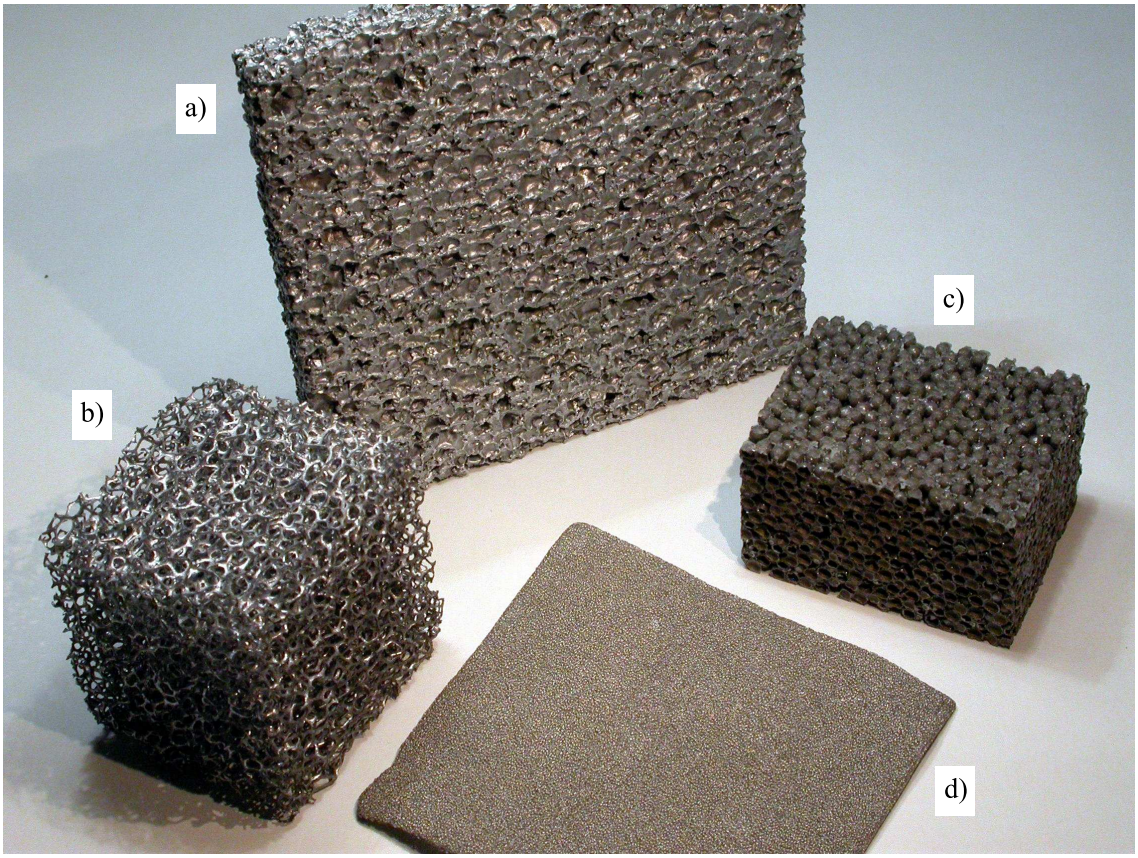

Figure 1.2 Samples of metallic cellular materials for engineering applications. a) closed cell aluminum foam, b) open cell aluminum foam, c) sintered hollow sphere foam, and d) open cell nickel foam.

to mimic the body's extracellular matrix, allowing the attachment and migration of bone cells [Freyman et al., 2001; Charriere et al., 2003; Williams et al., 2005].

1.2 Modeling and Simulation of Cellular Materials

Computational modeling and simulation of materials with a cellular microstructure is a broad field of research that has drawn considerable interest from engineers to biologists. Simulations give the possibility of investigating several aspects of the relations between the parameters of the microstructure and the overall mechanical properties of cellular materials. Two major directions of interest can be distinguished: the understanding of

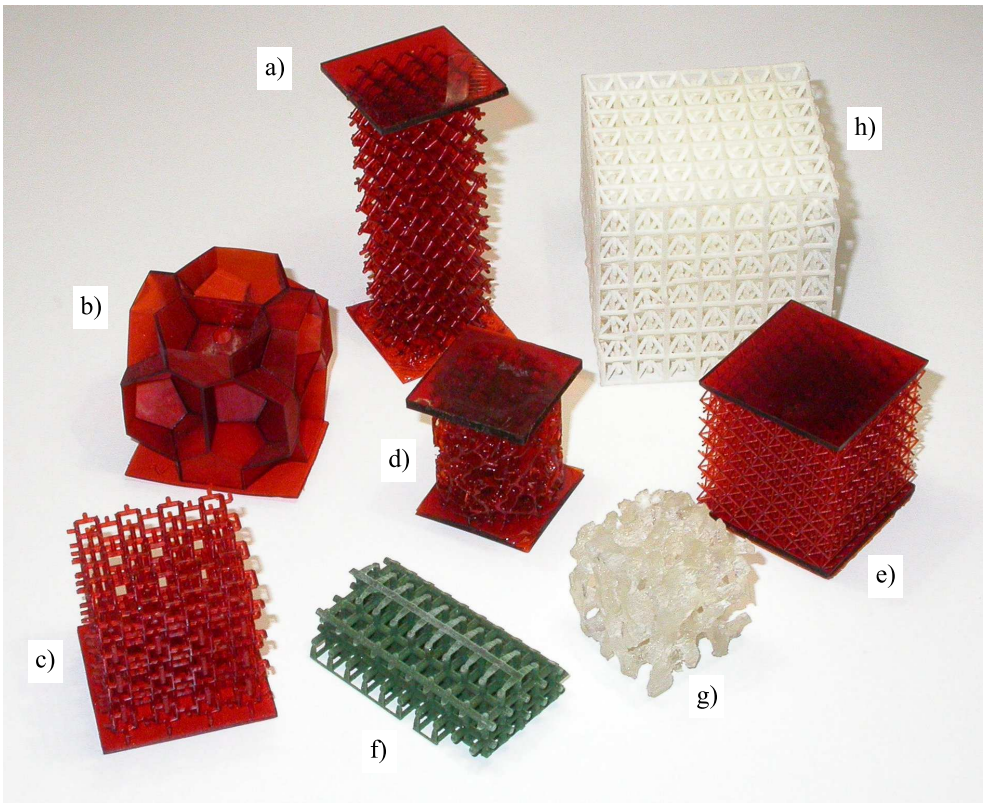

Figure 1.3 Sample structures fabricated by various Rapid Prototyping processes. a–e) fabricated by Digital Light Processing, f–h) fabricated by Selective Laser Sintering.

cellular materials designed by nature and the application of nature's design principles for cellular materials with tailored properties for engineering applications.

The present work deals with the numerical modeling and simulation of the mechanical properties of open cell structures, with the focus on open cell structures fabricated by Rapid Prototyping. The work is embedded within a project, see Figure 1.4, in which new cellular structures are designed, simulated by means of the Finite Element Method (FEM), fabricated by Rapid Protoyping, and tested [Luxner et al., 2004, 2005, 2006a,b; Stampfl et al., 2004; Woesz et al., 2004].

In Chapter 2 various FEM modeling strategies for cellular materials are discussed in terms of the linear mechanical behavior of different cellular structures. The nonlinear mechanical behavior of various open cell structures with the focus on elastic–plastic bulk material,

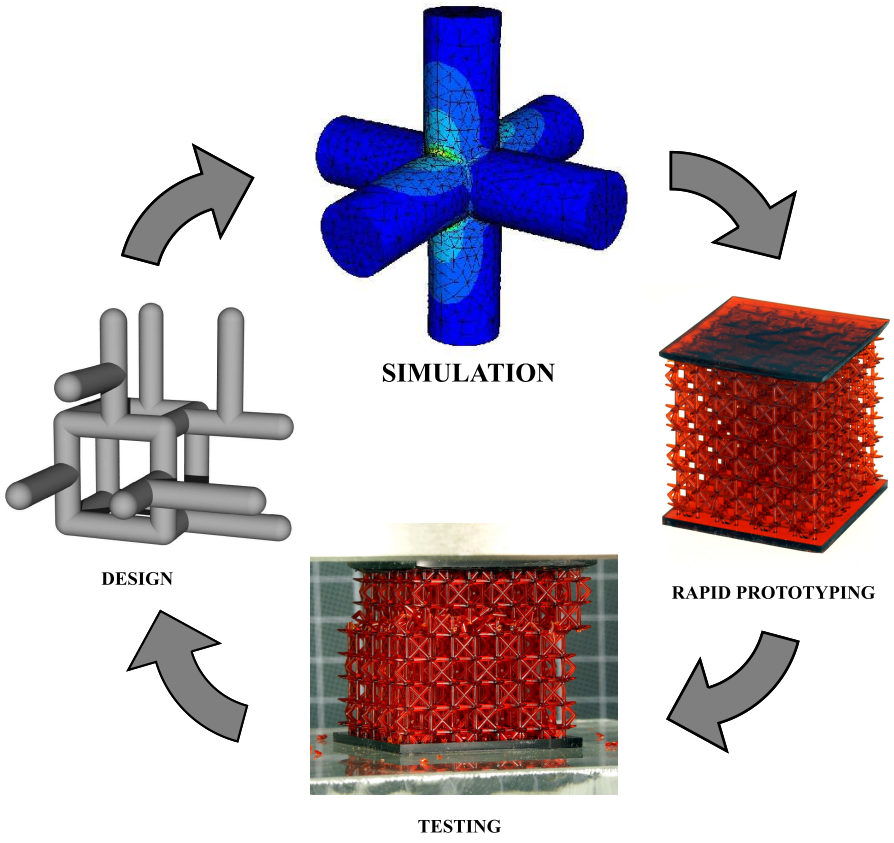

Figure 1.4 Interaction of design, simulation, Rapid Prototyping, and testing in the course of the design of new cellular materials with tailored mechanical properties.

deformation localization, and the influence of structural disorder is presented in Chapter 3. In Chapter 4 the influence of the size and the shape of samples subjected to uniaxial compression on the overall behavior is investigated. Chapter 5 deals with the design of new cellular structures with tailored overall properties. Several structures are introduced to achieve low anisotropy at high stiffness. Since cellular materials fabricated by nature or by a technical production process are not totally periodic and defect-free, the influence of structural disorder and defects on the mechanical behavior is investigated in Chapter 6.

Beside the use of standard commercial simulation packages several additional custom software tools have been developed for the design of the structures, the generation of the FEM models, and the processing of the data for the fabrication by Rapid Prototyping. A short description of the developed tools is given in Appendix A.

Chapter 2

Finite Element Modeling and Linear Elastic Investigations

Within the current chapter various Finite Element modeling concepts for cellular solids are presented. The differences between the various approaches are discussed in terms of linear analyses of four three–dimensional regular open cell solids with different microstructures. Furthermore, the simulation results are compared to experimental results.

2.1 Introduction

Highly porous, cellular solids form the basis of many biological and engineering structures. Their main advantage is the possibility of tailoring their mechanical properties by designing appropriate cell architectures. This requires knowledge on the relationship between their architecture and their overall mechanical response.

Several analytical and numerical approaches have been developed for describing the mechanical behavior of cellular materials. Analytical models based on beam theory are derived by Gibson and Ashby [1988, 1999], giving the effective mechanical properties as functions of the structures' relative density. Various analytical and numerical techniques considering the effective elastic behavior of low density regular cellular solids are presented by Grenest-

edt [1999] and Christensen [2000]. Modeling approaches based on tetrakaidecahedral unit cells have been widely used for studying cellular structures. Analytical methods [Zhu et al., 1997] and simulations employing the Finite Element Method (FEM) [Kwon et al., 2003] are used for analyzing the effective stiffness of open cell metallic foams with tetrakaidecahedral unit cells. In [Kwon et al., 2003] a comparison of numerically, analytically, and experimentally obtained results is reported. In [Sanders and Gibson, 2003] the elastic moduli and initial yield strength of hollow-sphere foams are analyzed using continuum element based Finite Element simulations. Analytical and numerical analysis of the nonlinear-elastic effective stress-strain behavior of two–dimensional model foams in the finite strain regime are presented by Hohe and Becker [2003]. With respect to closed cell metallic foams a comprehensive treatment of simulation methods on both the micro and the macro scale can be found in [Daxner et al., 1999, 2000; Daxner, 2003].

This chapter deals with numerical simulations of three–dimensional regular open cell structures by means of FEM. Various modeling approaches are introduced to analyze four generic three–dimensional structures [Luxner et al., 2004, 2005]. The structures are chosen to cover a wide range of different connectivities (defined as number of vertices over number of struts), presumably leading to different deformation mechanisms.

The smallest periodic unit of a structure will be called “base cell” in the present work. Figure 2.1 shows the base cells of the investigated structures, Simple Cubic (SC), Gibson Ashby (GA), Body Centered Cubic (BCC), and Reinforced Body Centered Cubic (RBCC). The base cells have equal size, being built of struts with circular cross sections. The strut diameter is constant within each individual structure. The indicated directions in Figure 2.1 are herein after referred to as the principal directions of the structures. By repeating these base cells in the three principal directions periodic structures are obtained. All structures are of cubic material symmetry. The bulk material of the structures is a polymer for which within the current chapter isotropic, linear elastic material behavior is assumed.

Three different FEM modeling techniques are utilized and their applicability is assessed with respect to modeling cost and quality of the results. As a computationally cheap approach, higher order beam elements are used for modeling the structures. Straightforward

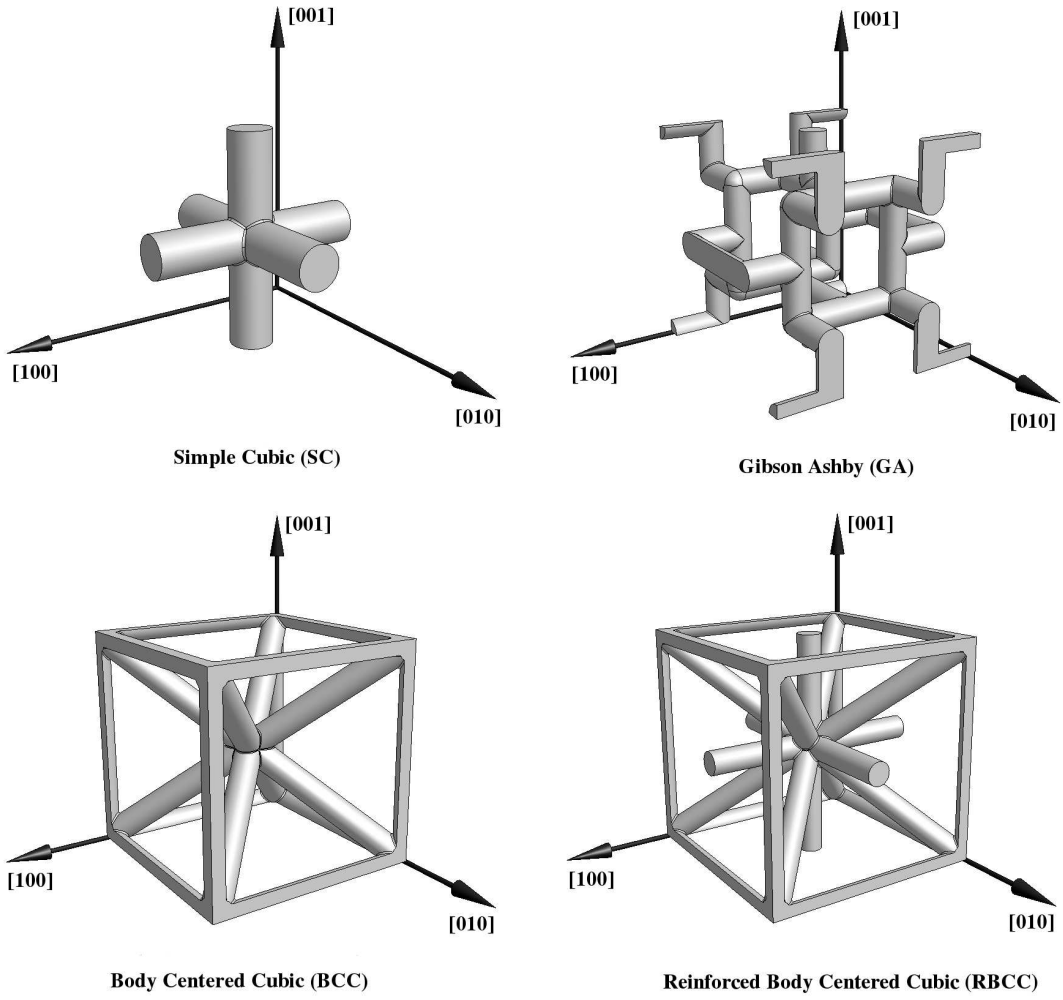

Figure 2.1 Base cells of the investigated structures, all of equal size and relative density of 10%.

discretization by beam elements is used as well as a beam modeling approach adapting the stiffness and the material distribution in the vicinity of the vertices. Continuum element based models are employed for highly detailed analyses, being computationally much more expensive and requiring high modeling effort.

The structures are treated as infinite and finite media, employing unit cell models and finite size models, respectively. The latter are variable in size, being composed of a given number

of base cells. Differences of the modeling approaches are discussed and the comparability of the respective results is evaluated.

Constitutive characterization of the three–dimensional cellular structures for the linear elastic regime is done by determination of the entire elasticity tensors using the unit cell models, from which the directional dependence of the Young's modulus is derived. The density dependence of the Young's modulus is described for different structures and for varying orientations.

Corresponding specimens are fabricated using two different Rapid Prototyping techniques and tested by means of uniaxial compression. The extent of the free surface effects is investigated by simulating finite samples of different size and a comparison of computational predictions with experimental results is shown.

2.2 Finite Element Models

All numerical investigations are carried out by means of the Finite Element package ABAQUS/Standard (*Versions 6.4.3 and 6.5.3, HKS, Pawtucket, RI*). In this section three different FEM modeling techniques are presented. Beam element based models are utilized for unit cell analyses and for the simulation of finite samples. For a highly detailed representation of the structures, continuum element based unit cell analyses are used. They are taken as reference models to assess the applicability of the beam element based models.

2.2.1 Beam Element Models

The beam element approaches employ three–dimensional beam elements for modeling the structures. Timoshenko beam elements with quadratic interpolation functions are used to allow for bending and transverse shear deformations. At least four elements are used for the discretization of a single strut.

Beam element based models are computationally cheap, however, straightforward modeling of a vertex by beam elements suffers from two approximations. First, it does not account

for multiple volumes at overlapping domains. Second, such models do not account for possible constraints in the vicinity of the vertices, caused by the material aggregation in these domains. Thus, the distribution of the material in the intersections of the struts should be considered in terms of stiffness and density.

To find the strut radius matching the desired relative density of the model the material distribution in a vertex is approximated by a sphere with a radius equal to the strut radius. The connected cylindrical struts end at the sphere's surface, which leaves gaps and may create overlaps. This approximation is used throughout this study for vertices connecting more than two struts. The accuracy of this approximation depends on the layout of the vertices.

An adaptation of the stiffness in the vicinity of the vertices is introduced by using very stiff elements within a spherical domain around the vertices with a radius equal to the strut radius. The "rigid" behavior is achieved by setting the Young's modulus 1000 times higher than the polymers' Young's modulus. This adaptation is considered preferable for vertices connecting four or more struts, but not for vertices connecting two or three struts.

Note that in the course of this thesis beam elements are visualized with their "real" diameter using the *Persistence of Vision Raytracer* (*www.povray.org*).

2.2.2 Continuum Element Models

Tetrahedral elements with quadratic interpolation functions are employed for the continuum element based approach. This has the advantage that all features of the structures' geometries are captured in high detail. Unlike the beam element based models, the fillets between the struts, see Figure 2.1, which emerge during the rapid prototyping process, are modeled by the continuum element approach. Furthermore, it is possible to study highly resolved stress and strain fields in the vicinity of the vertices. For all continuum element based models the element edge length is chosen to be not larger than 1/6 of the strut diameter. Additional mesh refinement is done at the vertices (element edge length not larger than 1/12 of the strut diameter). The chosen discretization allows for an accurate representation of the deformation patterns. The considerable modeling effort required and

the high number of degrees of freedom, resulting in high computational cost, set the limit of applicability and size for the continuum element based models.

2.3 Structural Models

In the previous section three different FEM modeling techniques have been presented. This section deals with two different approaches for representing the structures as infinite or finite media, respectively. Treating the structures as infinite media has the benefit that the mechanical behavior of the structures (except structural stability and localization of deformation) can be described by looking only at the periodically repeating part of the structures, resulting in rather small numerical models. To achieve correspondence to the experimental setup, see Section 2.4, the entire specimens are modeled as finite media, consequently, resulting in larger numerical models.

2.3.1 Infinite Medium Models

All investigated structures exhibit spatial periodicity. The mechanical behavior of a three–dimensional infinitely repeated periodic structure can be described by modeling an appropriate space filling three–dimensional unit cell with proper boundary conditions [Pettermann and Suresh, 2000; Böhm, 2004; Pahr, 2003; Anthoine, 1995]. Unit cells of different size and shape may be chosen for each structure. Here, base cells as shown in Figure 2.1 are taken as representative unit cells for the simulations with continuum elements. For the beam element based models struts, which sit in opposite faces of the unit cell boundary cube, are represented only in one of those faces.

Homogenization via a periodic microfield approach is employed for analyzing the effective mechanical behavior of the infinite periodic arrangement under far field mechanical loads. A FEM based homogenization concept, also known as “macroscopic degrees of freedom” (concept of masternodes), is employed, e.g. [Pettermann and Suresh, 2000; Böhm, 2004; Pahr, 2003; Anthoine, 1995]. Appropriate coupling of the degrees of freedom of the unit cell boundaries is applied to the FEM model to achieve spatial periodicity of the deformation

field. Far field mechanical loads are applied to the masternodes. For the FEM modeling of the unit cells the beam element based approach and the continuum element based approach are used. A comparison of the various FEM modeling techniques will be presented in Section 2.5.

In order to characterize the structures by means of their effective mechanical properties the entire overall elasticity tensors of the structures are determined (note that this amounts to interpreting the open cell structures in terms of an equivalent homogeneous medium). For the most general case this can be done by applying six independent load cases to a unit cell model and assembling the overall elasticity tensors from the mechanical responses of the model. From the elasticity tensor the Young's modulus in any spatial direction can be computed.

2.3.2 Finite Medium Models

To assess the comparability of the unit cell predictions to experimentally obtained results, finite structures corresponding to test specimens, see Figure 2.2, are analyzed in addition to the unit cell simulations. By these models free surface effects are captured and the load is applied in a well defined way.

The top boundary conditions are chosen to represent a rigid plate, which remains parallel to the (001) plane, otherwise it can move freely, and rotate around the [001] axis. This is achieved by an appropriate coupling of the top face nodes. The coupling of the nodes within the top face is done by means of a surface based kinematic coupling constraint. This provides coupling between a reference node and nodes lying within a surface, i.e. the nodes of the top face are constrained to the displacements of a masternode. For the loadcase of uniaxial compression in the [001] direction the rotations around the [100] and [010] axes of the masternode are constrained and a negative [001] displacement is applied to the masternode. Furthermore, all degrees of freedom of the bottom face nodes are locked.

Beam element based FEM models are used to keep the number of degrees of freedom in a feasible range. At present, continuum element based FEM models of finite structures with reasonable mesh refinement are beyond computational limits.

2.4 Rapid Prototyping and Experiments

The test specimens consist of 8×8×8 base cells, see Figure 2.2, with the exception of GA, which consists of 4×4×4 base cells. Bottom and top plates allow for a well-defined load application and a clear representation of the boundary conditions in the finite sample FEM models.

Two different Rapid Prototyping (RP) techniques [Stampfl et al., 2004; Woesz et al., 2004] were used for the fabrication of the physical prototypes presented in this work, namely Digital Light Processing (DLP) and Selective Laser Sintering (SLS).

Digital Light Processing is a process based on the polymerization of photosensitive resins using a digital mirror device. By slicing the volume models of the cellular solids into layers of constant thickness, a series of bitmaps is generated. These bitmaps are then projected onto the resin's surface. Where the bitmap is white, the resin will solidify. Black regions of the bitmap leave the resin liquid. In contrast to traditional stereolithography [Jacobs, 1992; Gebhardt, 2000] (which uses an ultraviolet laser beam to cure the resin), DLP is based on using visible light. Therefore special resins, sensitive to visible light, have to be utilized [Liska et al., 2003].

Selective Laser Sintering uses an infrared laser to fuse thermoplastic powder particles. By selectively scanning the surface, the profiles of the object can be fused together. After one layer of the object has been completed, the build platform is coated with another powder layer and the process is repeated. The Young's modulus of the DLP material (a blend of acrylates and epoxy-based resins) was measured to be 2300 MPa, the polyamide powder used for SLS structures exhibits a Young's Modulus of 2400 MPa. The Poisson ratio for both types of materials is assumed to be 0.3.

The utilized DLP system (*Envisiontec Perfactory Mini*) allows to fabricate structures with high feature resolution (pixel size 40 μm) and good surface quality. Minimal wall thicknesses around 0.2 mm are easily achievable. Overhanging geometries can in most cases be fabricated without using support structures. In the case of cellular materials, such support structures would be impossible to remove. SLS is able to fabricate all overhanging geome-

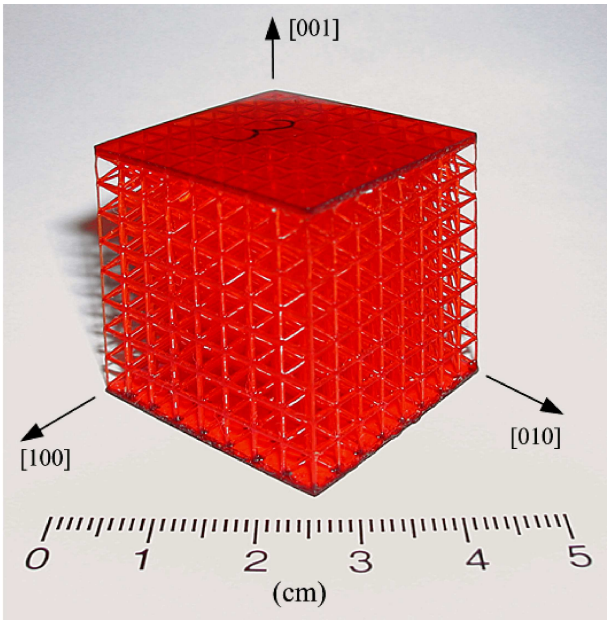

Figure 2.2 8×8×8 BCC test sample, fabricated by Digital Light Processing.

tries, but regarding feature resolution (≈0.1 mm) and minimum wall thickness (≈0.4 mm) SLS is inferior to DLP. DLP as well as SLS offer reasonably high build speeds. Several samples can be built per day, thus enabling the fabrication of four to five samples of each geometry presented in this work.

The fabricated structures were tested using a *Zwick Z250* universal testing machine[1]. The samples were loaded in uniaxial compression, and force as well as crosshead travel were recorded. In order to allow for free movement of the samples in the plane perpendicular to the loading direction, one compression plate was floating on steel balls, see Figure 2.3.

2.5 Results and Discussion

A number of simulations and analyses are performed utilizing the modeling approaches introduced above. The results are interpreted in terms of the elastic behavior. The ap-

[1]Fabrication and testing were performed at the Institute of Materials Science and Technology, Vienna University of Technology, Vienna, Austria.

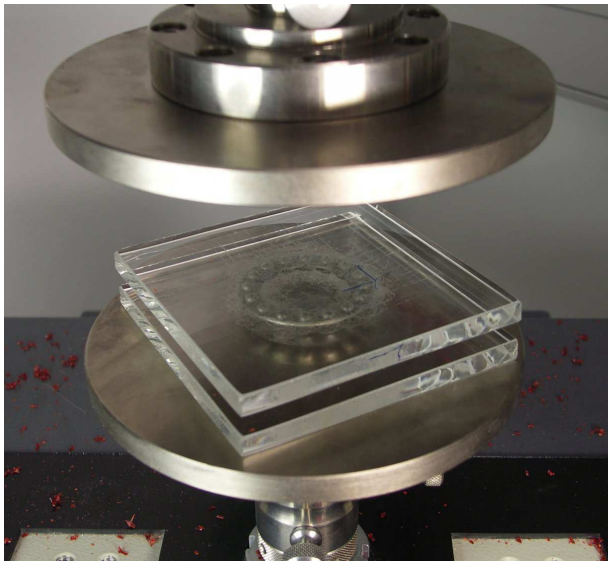

Figure 2.3 Experimental setup (without specimen); one of the compression plates has a floating support and can move in the plane perpendicular to the loading direction.

proaches are compared among each other as well as to experimental data.
For the unit cells, the entire elasticity tensors of the various structures are predicted in order to characterize the constitutive behavior. For the finite samples, the stiffness under uniaxial compression in various directions is predicted.

2.5.1 Density Dependence of the Young's Modulus

The relation between the density and the Young's modulus is discussed by recourse to beam element based unit cell models with straightforward beam modeling. Each of the four different structures is investigated at relative densities (defined as the density of the cellular structure normalized by the density of the bulk material) of 10%, 12.5%, 15%, 17.5%, and 20%. The density vs. Young's modulus data are predicted for three different directions, i.e. aligned with the cubic base cell edge [001], along the surface diagonal [011], and along the cube's diagonal [111]. For each structure and in each direction the data are fitted by the exponential regression function,

$$\frac{E^*(\underline{\phi})}{E_\mathrm{s}} = C\ {\rho_\mathrm{rel}}^{\beta(\underline{\phi})} \qquad , \tag{2.1}$$

according to Gibson and Ashby [1999], where ρ_{rel} is the relative density, E_{s} is the Young's modulus of the bulk polymer, and $E^*(\underline{\phi})$ is the effective Young's modulus of the structure. $\beta(\underline{\phi})$ denotes the density exponent and $\underline{\phi}$ is the considered direction. The resulting density exponents are summarized in Table 2.1. For the factor of proportionality, C, a wide scatter between 0.1 and 0.6 is found. Analyzing the many different influences on that factor is beyond the scope of this study. However, the validity of the exponent data holds, and will be discussed in the following.

It is well known, that the value of the density exponent depends on the governing deformation mechanisms in the considered directions [Gibson and Ashby, 1999; Grenestedt, 1999; Stampfl et al., 2004]. For structures and loading directions where the local deformation of the struts is stretching or shearing, the Young's modulus changes linearly with the density. On the other hand, the Young's modulus changes with the power of the relative density for structures and loading directions with bending dominated strut deformation. From the present results, see Table 2.1, it is obvious that the governing deformation mechanism for SC changes with direction. In the principal directions stretching is the prevailing deformation mechanism, because struts continuously pass through in these directions. For the [011] and [111] directions the density exponent increases, indicating a deformation mechanism dominated by strut bending.

For GA the density exponent is nearly two in the principal directions, reflecting the fact that in these directions the structure is bending dominated. The density exponent decreases for the [011] and [111] directions to 1.74 and 1.76, respectively. Thus, bending is the dominant but not the exclusive deformation mechanism in these directions.

BCC and the RBCC exhibit density exponents close to one for all investigated directions. Stretching is the principal mechanism, as a consequence of the favorably oriented diagonal struts.

2.5.2 Directional Dependence of the Young's Modulus

The directional dependence of the Young's moduli of the structures is derived from the elasticity tensors of the continuum element based unit cells. This is done for structures

Table 2.1 Density exponent, see Equation 2.1, for different structures and different directions in the relative density range between 10% and 20% determined by continuum element based unit cell models.

Structure	[001]	[011]	[111]
SC	1.00	1.83	1.85
GA	1.98	1.74	1.76
BCC	1.03	1.02	1.01
RBCC	1.01	1.02	1.02

with a relative density of 10%. Figure 2.4 shows the directional dependence of the Young's moduli, E^*, normalized by the Young's modulus, E_s, of the bulk material in the (100) (left) and $(1\bar{1}0)$ (right) planes, respectively.

SC exhibits high stiffness in the principal directions governed by axial loading at the struts. For deviations from the principal directions bending deformation of the struts is initiated. The latter mode gives rise to a much more compliant behavior and the normalized Young's modulus decreases rapidly.

For the bending dominated GA the principal directions are the stiffest directions, too. Deviations from the principal directions give rise to deformations of additional struts (the ones aligned with the cube's edges) resulting in lower stiffness. For almost all directions the normalized Young's modulus is much lower compared to the other structures.

Different behavior is shown by BCC, where the stiffest direction of this structure is the [111] direction. For RBCC the direction dependence of the normalized Young's modulus is less pronounced than for all other investigated structures. The directions with the highest value for the normalized Young's modulus are the principal directions. For both structures the more uniform spatial orientation distribution of the struts results in less anisotropy. Such more uniform three–dimensional networks carry loads rather by axial strut forces and prevent local strut bending, as discussed in the previous section.

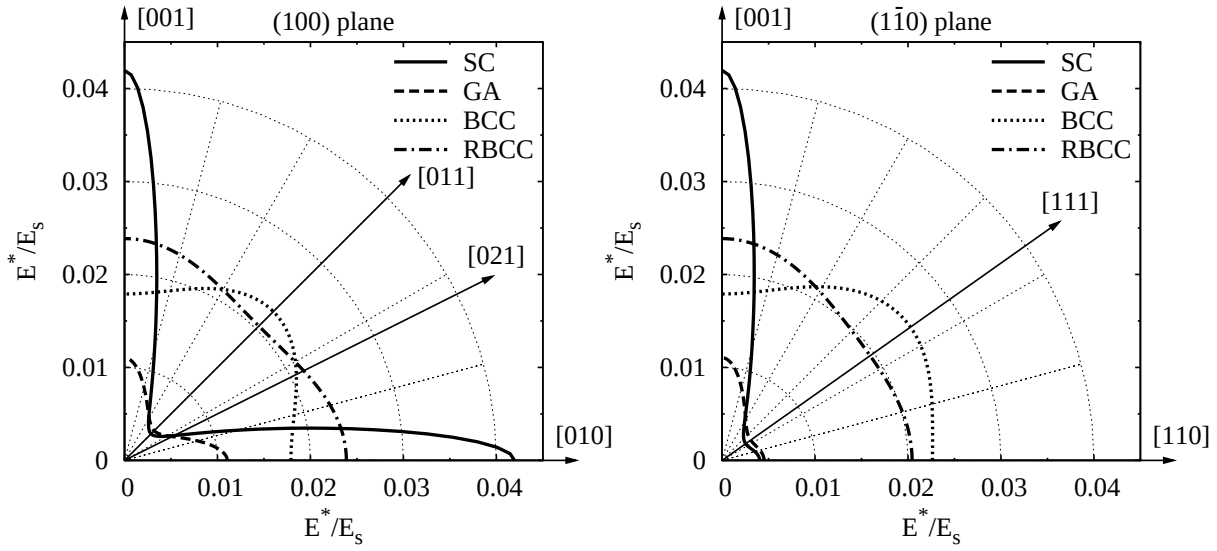

Figure 2.4 Comparison of the normalized Young's modulus in the (100) and (1$\bar{1}$0) planes for all structures with a relative density of 10%; results are obtained from the continuum element based unit cell models.

2.5.3 Comparison of FEM Modeling Techniques

The presented FEM modeling techniques are compared by means of the normalized Young's moduli for several directions of the investigated structures at 10% relative density. Figure 2.5 shows the normalized Young's moduli in the (100) plane predicted by the following approaches; continuum element based unit cell models (dashed bold lines), beam element based unit cell models with (solid bold lines) and without (solid thin lines) stiffness adaptation, as well as beam element based finite structure models with (open symbols) and without (filled symbols) stiffness adaptation in the vicinity of the vertices. The approximation of the density is done for all beam element based models.

The modeling of the density and the adaptation of the vertex stiffness are of approximative character. A unique treatment has been chosen for evaluating this approach and to learn about its effect on various structural architectures. Two effects on the elastic behavior are involved, being more or less pronounced at different situations. First, the density approximation yields some gaps and/or overlaps, and, consequently, a few percent error for the strut diameter at fixed density. Second, the stiffness of the vertex tends to be overes-

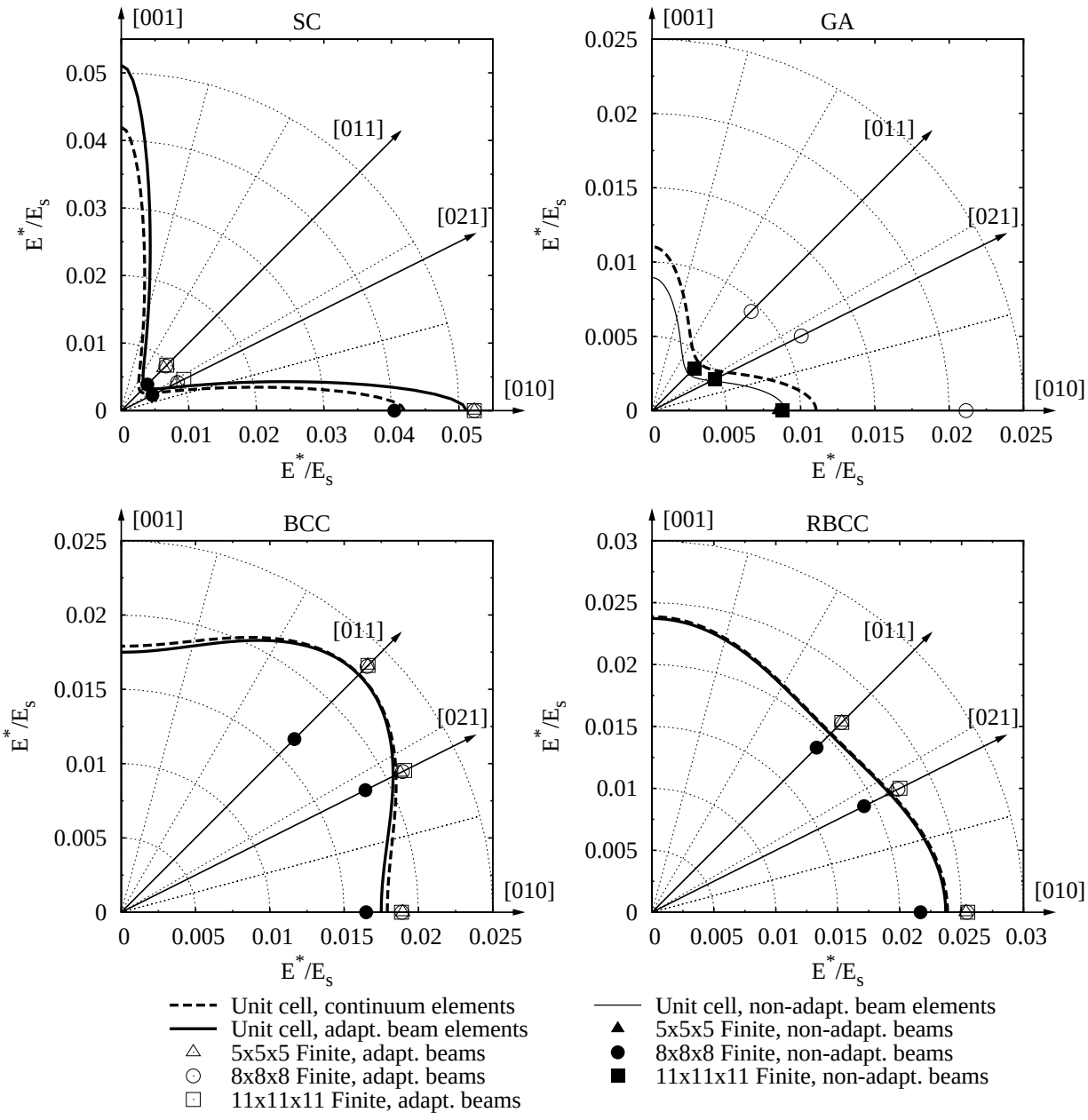

Figure 2.5 Comparison of modeling approaches in terms of the normalized Young's modulus in the (100) plane for structures with a relative density of 10%.

timated for some local loading scenarios, like stretching in direction of the strut axis. It was not attempted to find a best fit for each individual structure (and maybe each loading direction and density), but rather to gain general knowledge from such an approach.

Considering both unit cell models for SC (Figure 2.5, top left) it can be seen that the stiffness in the principal directions is overpredicted by the beam element model. This is caused by the rigid domains of the straight through struts in these directions. Deviating from the principal directions, the differences of the stiffness predictions decrease. For BCC and RBCC (Figure 2.5, bottom) the stiffness predictions by the unit cell models coincide.

In contrast to the structures discussed before, beam element based unit cells without an adaptation of stiffness are compared to the continuum unit cells for GA, since this structure exhibits only vertices connecting three struts. Due to the high number of vertices in this structure a minor stiffening effect due to material aggregation in the vertices is neglected. On the other hand, stiffness adaptation leads to a pronounced overstiffened behavior of the beam element based unit cell. This fact is shown in Figure 2.5 (top right, open symbols) in terms of the finite samples with applied stiffness adaptation. It can be seen that the beam element unit cell reacts in a more compliant way than the continuum element based unit cell model, indicating that the stiffness of the vertices is underestimated. The high number of vertices and short struts lead to less accuracy of the density approximation, too. The estimated strut radius is too large, increasing the stiffness of the structure and compensating partly for the omitted stiffness adaptation of the vertices.

The beam element models with and without adaptation of the stiffness at the vertices are also compared in terms of the 8×8×8 finite structure models. In Figure 2.5 (open and filled circles) the values of the normalized Young's moduli for three different directions are shown. It can be seen that the finite structure models without rigid domains respond less stiffly. The deviation between the two beam element based models depends strongly on the topology of the structure and the governing deformation mechanism, respectively. For directions in which bending is the governing mechanism, like [011] of SC, [011] of BCC, and all directions of GA the deviation is higher than for stretching dominated directions.

2.5.4 Influence of the Specimen Size

Finite samples consisting of different numbers of base cells are modeled by beam elements with adaptation of stiffness. The results are compared to the continuum unit cell models in order to assess the required specimen size for testing, i.e. the effect of the free faces as well as the effect of the top and bottom plates. The latter introduce additional constraints giving rise to higher stiffness, whereas the former result in a decrease of the stiffness.

Evaluation is done for three directions in terms of the normalized Young's modulus. Finite samples consisting of 5×5×5, 8×8×8, and 11×11×11 base cells are analyzed. Figure 2.5 shows a comparison of the simulation results of the various finite sample sizes for the different structures.

It can be seen that the results of the various samples sizes correspond well for all structures. General rules, however, regarding the size of testing specimens and for extrapolation to properties of infinite structures cannot be derived from these investigations, since the surface effects strongly depend on the structure's architecture and on the governing deformation mechanisms in the considered direction.

It is noted, that the inclined direction is chosen as [021] leaving sample surfaces with a minimum amount of dissected base cells. Arbitrary inclinations are expected to give rise to a more pronounced influence of the surfaces.

2.5.5 Comparison to Experimental Results

Figure 2.6 shows the results of the continuum element based unit cells and the 8×8×8 finite structural models with stiffness adaptation in comparison to experimental results [Stampfl et al., 2004; Woesz et al., 2004] in one of the principal directions.

For structures with directionally less sensitive behavior such as BCC, RBCC, and GA the results correspond very well, whereas for structures with high directional sensitivity such as SC deviation of the simulation results is noticeable. For SC the geometric imperfections that occur during the fabrication process may play a significant role, as do experimental

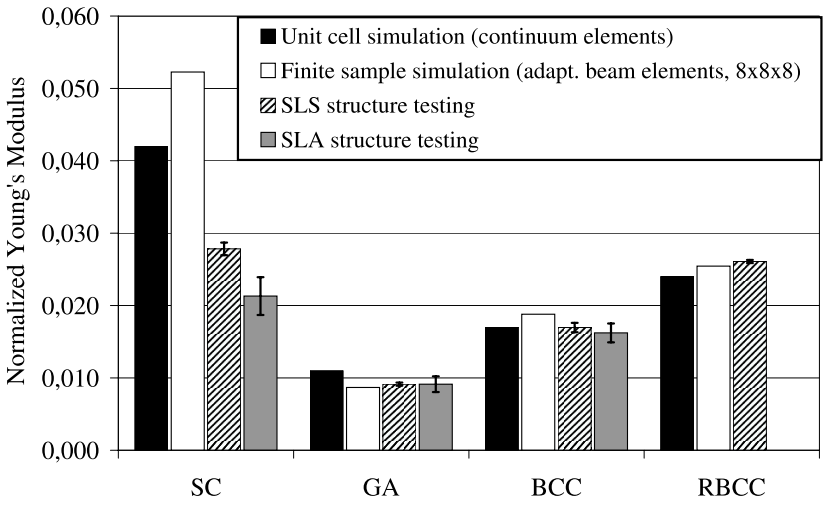

Figure 2.6 Comparison of experimental and simulation results regarding uniaxial compression in one of the principal directions, relative density of the structures is 10%.

conditions. As can be seen in Figure 2.4 small changes in loading direction lead to a pronounced decrease of the normalized Young's modulus. In addition, structural disorder is also expected to reduce the stiffness in the principal directions.

2.6 Conclusions

Various Finite Element modeling concepts and linear analyses of regular open cell structures are presented in this chapter.

Continuum element based unit cell models are utilized as reference models to discuss the applicability of beam element based models with and without an adaptation of stiffness in the vicinity of the vertices. The accuracy of the beam element models' results is found to be dependent on the structures' geometries and on the governing deformation mechanisms, respectively. The mechanical behavior of all structures is represented very well by the beam models, which are shown to be suitable for modeling of such structures.

Unit cell models are employed for a constitutive characterization of four different structures in terms of density and directional dependence of their normalized Young's moduli. The governing deformation mechanisms are identified. Both the mechanical properties and the deformation behavior are found to be strongly dependent on the structure's architecture, as well as on the loading scenario.

Finite samples consisting of different numbers of base cells are simulated to investigate the influence of free surfaces and load introduction. Both influences strongly depend on the structures' architecture and on the sample orientation, so that no general rule regarding the specimen size can be derived from these results.

The results of the simulations are compared to experimental results by means of uniaxial compression tests. It is shown that for structures with rather high directional sensitivity imperfections play a significant role and the results deviate. For all other structures the simulation results agree very well with the experimental results.

Chapter 3

Nonlinear Behavior of Regular and Disordered Cellular Structures

Based on the beam element models presented in Chapter 2, within the current chapter the models are extended to elastic-plastic bulk material behavior, large strain theory, and deformation localization. Inspired by nature (e.g. cancellous bone), the influence of structural disorder on the linear and nonlinear mechanical behavior of cellular structures is investigated by the Finite Element Method (FEM).

3.1 Introduction

In the production of man-made cellular materials, e.g. by foaming of plastics and metals, it is quite difficult to control the internal structure, i.e. the microstructure is disordered. Even when using rapid prototyping techniques, where predetermined geometries at high spatial resolution can be fabricated [Stampfl et al., 2004; Woesz et al., 2004], some disorder due to the inaccuracy of the fabrication process remains. Therefore, a sound understanding of the relations between the microstructural disorder and the overall mechanical behavior of cellular structures is important. In particular, knowledge on the governing mechanisms is desired.

The influence of different kinds of structural imperfections on the effective mechanical properties of two- and three–dimensional cellular solids has been widely investigated. Silva and Gibson [1997a] investigate the effects of non-periodic microstructure and missing cell walls on elastic moduli, plastic collapse strength, and localization of deformation of two–dimensional cellular solids by means of the FEM. Guo and Gibson [1999] employ the FEM to study the localization behavior of two–dimensional honeycombs with and without defects. Regular and disordered, low-density two–dimensional open-cell foam models subjected to large deformations are investigated numerically by Shulmeister et al. [1998]. Li et al. [2005] utilize the Voronoi tessellation technique and the FEM to analyze the effect of disorder in cell shapes and non-uniform cell wall thickness on the elastic properties of two–dimensional honeycombs. In the case of three–dimensional structures mostly Voronoi foams are utilized. Roberts and Garboczi [2002] investigate the elastic behavior of three–dimensional random foams using the FEM. The effect of cell disorder on the elastic properties of three–dimensional, low-density, open-cell Voronoi foam models is analyzed by Zhu et al. [2000]. Zhu and Windle [2002] model the high strain compression of low-density three–dimensional open-cell polymer FEM foam models. The mechanical behavior of linear elastic open cell foams is investigated by Gan et al. [2005] using three–dimensional FEM Voronoi models.

Within this chapter the effect of structural disorder on the linear and nonlinear mechanical behavior is evaluated under consideration of elastic-plastic bulk material properties, large strain theory, and deformation localization.
First, the linear elastic properties are investigated by a periodic microfield approach. Based on three–dimensional periodic unit cell models the entire elastic tensors are predicted for six different generic structures with regular geometries. The anisotropic stiffness and the directional sensitivities are presented. Out of these six structures the two with the highest and the lowest degree of anisotropy are selected for further studies. On large periodic unit cells geometrical disorder of varying level is introduced to the structures and their effect on the linear elastic behavior is studied.

Second, the nonlinear mechanical behavior is investigated in detail for the two selected structures. Since this, in general, cannot be accomplished by means of periodic unit cell

models, large finite samples are employed which are loaded by uniaxial compression. Different orientations of the structural lattice with respect to the loading direction are realized. As for the linear cases, regular structures are considered first and then a systematic study on the influences of structural disorder is performed. On the one hand, the focus is set to the overall nonlinear response, in particular the peak load and the overall stress-strain behavior in regimes moderately beyond the load maximum. On the other hand, the influence of structural disorder on the spatial deformation distribution is studied, i.e. whether or not deformation localization occurs and to which degree.

3.2 Methods

The modeling of porous structures comprises several tasks. First, the generation of particular geometries of the structures; second, the setup of appropriate representations within the framework of a computational method (here, the Finite Element Method); and third, the assessment of the simulation results. In the following the investigated structures, the computational modeling techniques, and the interpretations of the data are explained in detail.

3.2.1 Bulk Material

The bulk material of the structures is a crosslinked photopolymer for which isotropic, elastic-plastic, strain rate independent material behavior is assumed. The Young's modulus of the bulk material, E_s, is 1700 MPa, the Poisson's ratio is 0.3, and the yield stress is 18 MPa. In Figure 3.1 the uniaxial stress–strain curve of the bulk material is shown. J_2 plasticity and isotropic hardening are assumed.

3.2.2 Structural Models

Six generic three–dimensional structures are selected in an effort to choose topologies with a variety of mechanisms governing their behavior. At first, all of them show regular geome-

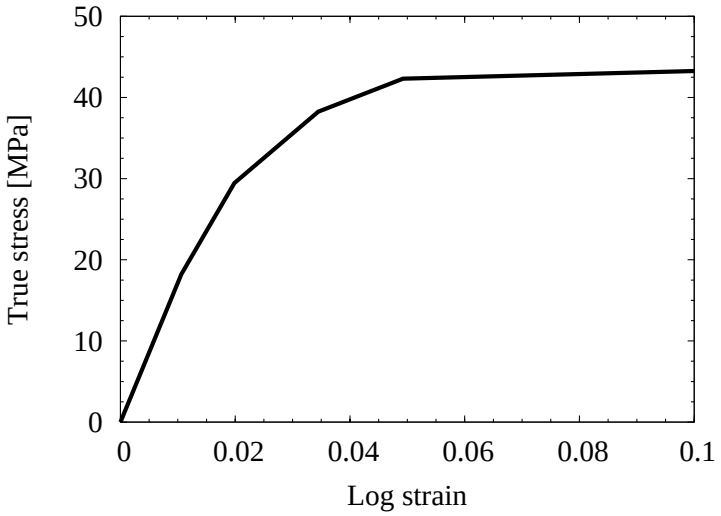

Figure 3.1 Uniaxial stress-strain curve of the bulk material (crosslinked photopolymer). For strains larger than 0.1 linear extrapolation is used.

tries which are repeated periodically in all principal directions. The six different base cells to be investigated are shown in Figure 3.2 at the top of each row. They comprise Simple Cubic (SC), Gibson Ashby (GA), Reinforced Body Centered Cubic (RBCC), and Body Centered Cubic (BCC), as already introduced in Chapter 2, as well as Kelvin (KV) and Weaire Phelan (WP) structures. Each structure exhibits a relative density of 12.5% and consists of struts with circular cross sections of constant diameter. The dimensions of all base cells are 4 mm $\times$ 4 mm $\times$ 4 mm. All base cells possess cubic material symmetry. Note that only struts belonging to a single base cell are shown. The cells may appear incomplete at first sight, in periodic repetition, however, their space-filling structural geometries become obvious.

For periodic structures the consideration of a base cell is sufficient in most cases. However, when introducing structural disorder larger models are required. Disordered structures are generated for SC and KV topologies by disturbing arrangements of 8×8×8 base cells. The vertices of the regular geometries are shifted to random positions by a fixed distance, δ. For the shifting direction a spatially random distribution [Marsagli, 1972] is adopted. The shifting distance, δ, is expressed in fractions of the strut length l of a regular reference structure. Note that all struts of regular SC and KV structures exhibit equal length.

Displacement magnitudes $\delta/l = 1/16, 1/8, 1/4$, and $3/8$ are realized, see Figures 3.3 and 3.4, upper rows. Such disorder in the structures, however, increases the strut lengths and, consequently, affects the density. Thus, for representing the desired density the strut diameter is adapted accordingly.
Note that within this thesis the notion disorder is used in terms of randomly shifted vertex positions, and that in terms of the topology the structures are still ordered.

Depending on the behavior to be predicted an appropriate modeling approach has to be selected. Accordingly, two different approaches for representing the structures as infinite and finite media, respectively, are employed. The first approach is the periodic unit cell (periodic microfield) method, e.g. [Pettermann and Suresh, 2000; Böhm, 2004; Pahr, 2003; Anthoine, 1995], by which several aspects of the mechanical behavior of an infinite periodic structure can be described in terms of an equivalent homogeneous medium, see Section 2.3.1.

In this study the unit cell approach is used for the linear elastic investigations. Models consisting of a single base cell are employed for the determination of the elasticity tensor of a regular infinite structure. Unit cell models consisting of 8×8×8 base cells with structural disorder are used for the investigation of the influence of disorder on the elastic behavior.

The periodic unit cell approach shows severe shortcomings with respect to its ability of representing deformation localization. Due to the strictly enforced periodicity, deformations cannot localize in arbitrary planes within the unit cell. Essentially, periodicity acts as a filter and the richness of responses predicted for a given type of structure grows with the size and the orientation of the selected periodic cell. To overcome the limits of the unit cell models, i.e. to investigate aspects of the behavior of finite sized cellular solids, finite structures corresponding to test specimens, see Section 2.4, are modeled in the second approach. Finite sample models are used for nonlinear investigations in which deformation localization can become an issue.
The uniaxial compressive response of cuboidal samples showing lattice orientations of [001], [021], [011], and [111] is investigated. The number of base cells is chosen to achieve sample dimensions of approximately 32 mm × 32 mm × 32 mm. The top boundary conditions are assumed to represent a rigid plate, which remains parallel to the (001) plane, but can

move freely otherwise and rotate around the [001] axis. This is achieved by an appropriate kinematic coupling of the displacements of the top face nodes. Furthermore, all degrees of freedom of the bottom face nodes are locked representing a rigid plate which is fixed, see Section 2.4. The finite sample analyses account for large deformations.

3.2.3 Finite Element Modeling

All numerical investigations are carried out by means of the Finite Element package ABAQUS/Standard (*Version 6.5.3, ABAQUS Inc., Providence, RI*). Beam element based models with a relative density of 12.5% as described in Section 2.2.1 are utilized throughout this section. At least four elements are used for the discretization of the compliant part of a single strut. For the beam cross sections the number of Gauss points is chosen to be 24 (eight in circumferential direction times three in radial direction). No contact or self contact is considered.

When bifurcation buckling can become an issue, care has to be taken not to proceed along the trivial equilibrium path. For the regular SC structure loaded in the principal direction a small transverse force is applied to induce buckling affine deformations. For all other cases belonging to the SC set, localization (if existing) starts from the boundary of the sample or is triggered by the structural disorder. For the KV structures the Gauss point patterns in various beam elements are aligned differently which is sufficient to act as (numerical) imperfections. General instability problems of the present kind involving elastic-plastic materials are highly complex and not within the scope of the present work.

3.2.4 Localization of Deformation

In the context of this work localization of deformation is defined by the existence of a collapsed region which spans a wide area in a structure in two dimensions, and has a rather limited extension in the third direction.

The evaluation of localization from deformation plots is rather intuitive. For pronounced localization the effect is quite obvious. For the cases of increasing disorder, however, assessment of the deformed structures becomes more difficult. For this reason two methodologies for estimating the degree of deformation localization within a cellular structure are introduced.

Mesoscopic Strain Rates

It is assumed that localization within a cellular structure is caused by the collapse of cells. Cell deformation can be described by the strains between opposing boundary vertices of the cells, in the following denoted as mesoscopic strains. Then, at least one strain component, measured in the global coordinate system, of a collapsing cell shows a severe change during global (macroscopic) deformation. If a simultaneous increase in one mesoscopic strain component of a considerable number of cells is accompanied by a decrease of the same component in some other regions of the structure, i.e. when both collapse and unloading of some cells appear, localization is assumed to take place.

For the evaluation of the mesoscopic strains, within each cell pairs of adjacent vertices are selected – for each considered vertex its connected neighbor with the largest distance in load direction is taken, i.e. the members of a vertex pair belong to opposite boundary faces of a cell. To avoid bogus effects caused by free and constrained boundary vertices, only vertices with full connectivity, i.e. six for a SC structure, are considered.
The mesoscopic compressive strain component in load direction, ε_{33}, between the members of the vertex pairs during uniaxial compression of the sample is observed. The change of the observed mesoscopic compressive strain component, $\Delta\varepsilon_{33}$, is normalized by the change of the corresponding global (macroscopic) compressive strain component, $\Delta\Gamma_{33}$, to achieve the mesoscopic strain rate,

$$\bar{\varepsilon}_{33} = \frac{\Delta\varepsilon_{33}}{\Delta\Gamma_{33}}. \tag{3.1}$$

The development of $\bar{\varepsilon}_{33}$ of each vertex pair is plotted versus the corresponding macroscopic compressive strain component, Γ_{33}, for each time increment of the FEM analysis.

Histograms showing the distribution of $\bar{\varepsilon}_{33}$ within the structure are presented for selected macroscopic strains.

Total Energy Distribution

Considerations of the spatial distribution of the mechanical total energy in the structures can also be helpful in evaluating the localization of deformation. The characteristics of this localization area is, that the major part of the (overall) deformation is concentrated in it and that the stresses with respect to the corresponding planes are (rather) continuous. This implies that the mechanical energy is predominantly concentrated in such regions.

This effect is visualized in terms of three–dimensional energy histograms. For that purpose the total mechanical energy in each beam element normalized by the overall total mechanical energy is plotted versus the relative frequency. The latter is the number of elements sharing energy values within the same interval divided by the total number of elements. As a third axis the overall displacement is used. This way excessive energy consumption of a certain fraction of beam elements, i.e. localization, can be detected.

3.2.5 Overall Energy Considerations

In addition to the energy considerations at the Finite Element level, see Section 3.2.4, the elastic strain energy and the plastic dissipation energy of the whole samples are predicted. The energy values are normalized by the volume of the bounding box of the undeformed sample to achieve the homogenized elastic strain energy density, u_{el}, the plastic dissipation energy density, u_{pl}, and the total energy density, u_{tot}. The energy densities are plotted over the macroscopic strain of the samples, Γ_{33}, to assess the evolution until the macroscopic peak stress is reached.

The energy densities of regular and disordered structures for different lattice orientations are compared for the maximum macroscopic stress, $\Sigma_{33,\max}$. This is done under the assumption that exceeding $\Sigma_{33,\max}$ results in catastrophic failure of the structure and is not

relevant for the applications treated within this work. In the case of the disordered structures the average over five randomly disordered structures is used for the consideration.

3.3 Results and Discussion

3.3.1 Elastic Anisotropy

First, the anisotropy of the linear elastic stiffness of the regular structures is investigated for all six cases. Periodic unit cell models of single base cells are employed and the required number of independent load cases is solved for each structure. From these responses the entire elastic tensors are assembled. The Young's moduli in all spatial directions are extracted by rotational transformations of the tensors. In Section 2.5.2 the Young's moduli, E^*, (normalized by the Young's modulus of the bulk material, E_s) of SC, GA, RBCC, and BCC for directions within the (100) and $(1\bar{1}0)$ planes are presented in polar plots. Here, three–dimensional visualizations of the normalized Young's moduli of these structures are given in Figure 3.2. Additionally, the normalized Young's moduli of the KV and the WP structures with the same relative densities are shown. Note that for better visualization the scale of the normalized Young's moduli's contours is different for different structures. The normalized Young's moduli for the orientations [001], [021], [011], and [111] are listed in Table 3.1. Since all structures show cubic material symmetry, the extremal stiffness values appear in the [001] and the [111] direction [Nye, 1985].

The SC structure shows the most pronounced anisotropy and directional sensitivity with respect to the Young's modulus. It exhibits very stiff behavior in the principal directions and a strong decrease of the stiffness apart the principal directions. In contrast, the KV structure is the most isotropic one and exhibits nearly equal values for the normalized Young's modulus in all directions. The maximum occurs for the [111] direction. Because of the significant difference in their anisotropy the SC structure and the KV structure are chosen for subsequent investigations.

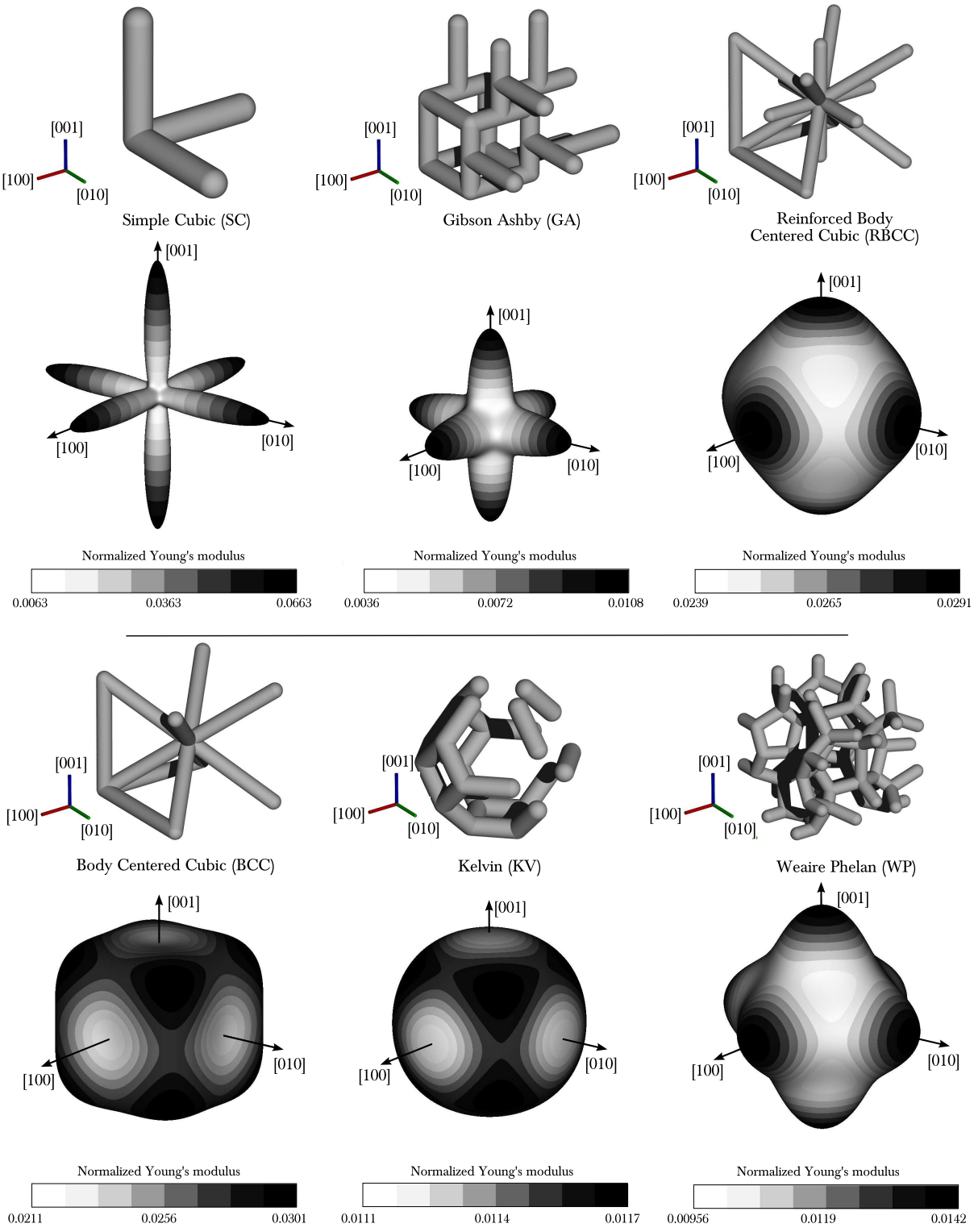

Figure 3.2 Base cells of the investigated structures with a relative density of 12.5% (in the upper of each row) and their individually scaled normalized Young's moduli in all spatial directions (below). Note the different scalings of the representations of the normalized Young's moduli.

Next, the influence of structural disorder on the elastic behavior of the SC and the KV structures is investigated. Because of the random character of the structural disorder, single base cells are no longer sufficient. Still, unit cell models are employed but consist now of some 8×8×8 base cells. For easier application of periodic boundary conditions the vertices located at the unit cell boundaries remain unchanged. Inside the cells structural disorder is introduced as described in Section 3.2.2. Four different degrees of disorder are analyzed. For each of them five different models (having the same statistical descriptors but different discrete realizations) are generated and the elastic tensors are predicted.

Figures 3.3 and 3.4 show details from the disordered structures (top) and the normalized Young's moduli for all directions (bottom). The latter shows one out of the five corresponding models for each level of disorder. The contour scaling is individual for each plot but the length scaling is the same for all plots in a figure. More details on the statistical variation of these results are given in Table 3.2, which lists the average, minimum, and maximum values of the normalized Young's moduli evaluated from the corresponding five models. The directions referred to always pertain to the regular structures from which the disordered geometries are derived.

In the case of the SC structure it can be seen that with increasing disorder the normalized Young's moduli in the principal directions decrease, whereas for the other directions the normalized Young's moduli increase. A pronounced anisotropy remains even for the most disordered case. The directions of the extremal values are unchanged compared to the regular structure.

The KV structure shows a decrease of the normalized Young's moduli for all directions. Note that for the most disordered case the Young's moduli are nearly uniform with respect to the direction, i.e. isotropy is approached closely, and that the extremal values are no longer aligned with the principal directions of the regular structure.

3.3.2 Nonlinear Behavior – Deformation Localization

So far the linear elastic behavior was considered for which periodic unit cells (of different sizes) are appropriate tools. They can also handle nonlinear deformations to a certain

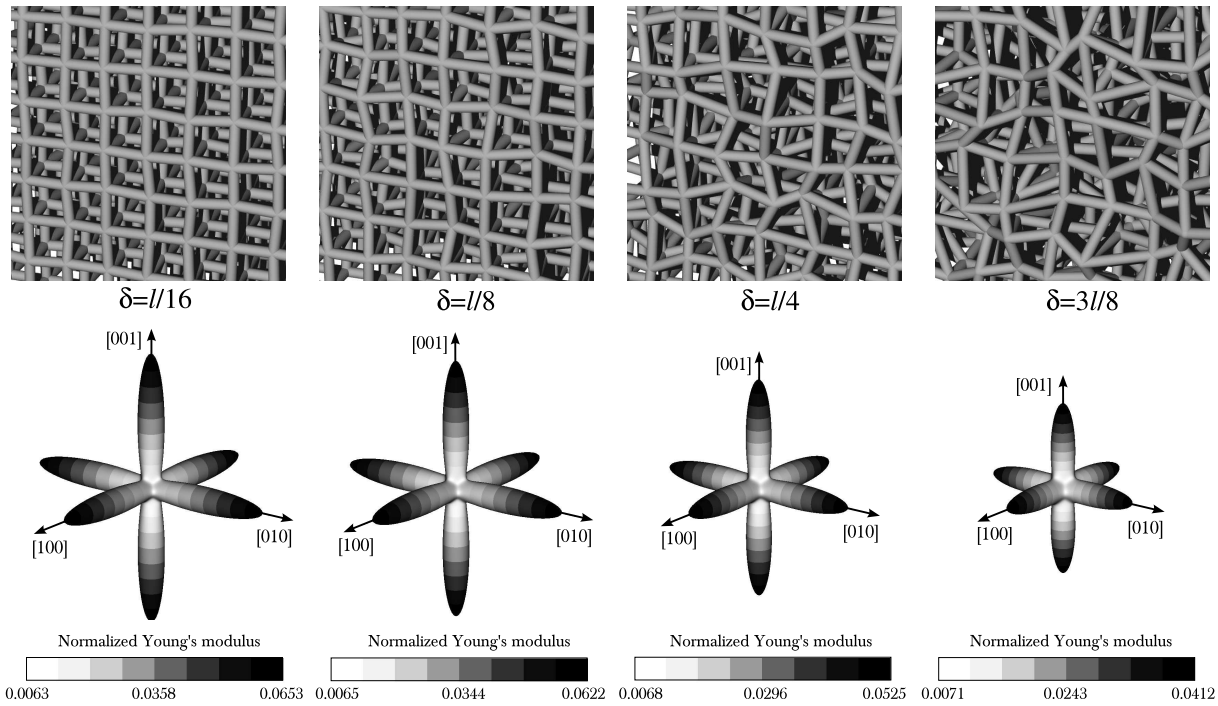

Figure 3.3 Influence of structural disorder, δ, on the elastic behavior of the Simple Cubic structure with a relative density of 12.5%; details of the disordered structures (top) and the predicted, equally scaled, normalized Young's moduli in all directions (bottom).

extent, however, other approaches have to be adopted for modeling deformation localization. The following investigations are based on finite samples which are loaded by uniaxial compression. The loading directions are given with respect to the lattice orientations and for disordered cases with respect to the lattice of the regular parent structures from which they are derived.

Again, the SC and the KV structures are studied. The results are given in terms of selected plots of deformed structures, overall stress–strain curves, diagrams showing the distribution and evolution of the mesoscopic strain rates and energy densities, and histograms showing the total energy distribution in the models. The presented results are restricted to the deformation regime before the onset of contact between struts.

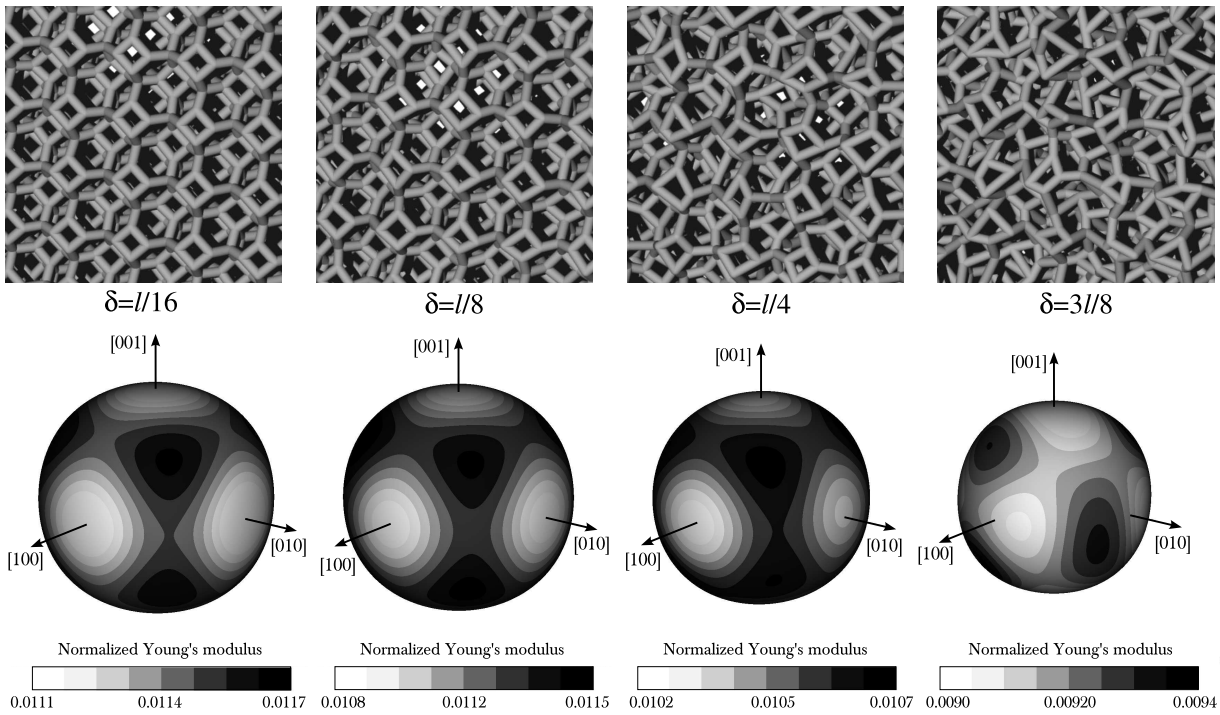

Figure 3.4 Influence of structural disorder, δ, on the elastic behavior of the Kelvin structure with a relative density of 12.5%; details from the disordered structures (top) and the predicted, equally scaled, normalized Young's moduli for all directions (bottom).

Regular Geometries

In this section the nonlinear deformation behavior under uniaxial compression of structurally perfect geometries is investigated using finite sample models.

In Figure 3.5 (first column) the deformation patterns of the regular SC structures at four different lattice orientations are shown without scaling the deformations. Pronounced localization of deformation can be seen. For the load cases [001] and [021] the localization takes place in a principal structure plane extending over one and two layers, respectively. These deformation patterns, however, are only one feature of the localization. The second parameter field required for fully describing the localization are the components of displacements within that plane, i.e. the direction into which the struts tilt. This will be called the localization displacement in the following. For the load cases [001] and [021] the localization displacements occur along a principal structure direction. In the [011] orientation the localization takes place in two perpendicular planes forming an "X", also showing

Table 3.1 Predicted normalized Young's moduli, E^*/E_s, of the regular Simple Cubic (SC), Gibson Ashby (GA), Reinforced Body Centered Cubic (RBCC), Body Centered Cubic (BCC), Kelvin (KV), and Weaire Phelan (WP) structures for a relative density of 12.5% at selected directions.

	$E^*/E_s \times 10^{-2}$			
	[001]	[021]	[011]	[111]
SC	6.630	1.193	0.816	0.631
GA	1.080	0.551	0.432	0.360
RBCC	2.906	2.632	2.499	2.389
BCC	2.106	2.460	2.716	3.007
KV	1.109	1.140	1.158	1.174
WP	1.421	1.152	1.041	0.956

localization displacements in principal directions. Note that, here, localization is triggered at the edge where the free and the fixed faces meet, so that other sample sizes may give rise to different deformation patterns. For the regular [111] case no distinct localization can be seen. The deformation concentrates in (011) planes but extends over the entire region which is not affected by the top and bottom constraints (representing rigid plates).
The overall stress–strain curves corresponding to the above scenarios are shown in Figure 3.6 by solid lines. In all cases plastic yielding starts well before deformation localization sets in. For [001] compression the highest peak load is reached at the smallest overall strain followed by a sharp drop upon localization. In [021] and [011] loading the behavior is similar, but with markedly reduced peak values at higher overall strains and only a moderate load reduction upon localization. Finally, the [111] case shows the lowest peak load and almost no subsequent decrease at high overall strains.

The behavior of the regular KV structures for the selected orientations is given in Figure 3.7 by the solid lines. All predictions are very similar both with respect to the peak loads and the corresponding overall strains as well as with respect to the rather smooth shapes of the curves. Similar to the elastic behavior, the directional dependence of strength is rather insignificant for the KV structures. The minimum peak value is predicted for the [111] orientation, the maximum for the [011] orientation. Note that this is in contrast to the

Table 3.2 Minimum, maximum, and average values of the predicted normalized Young's moduli, E^*/E_s, of Simple Cubic and Kelvin structures with various levels of disorder, δ, for a relative density of 12.5% at selected directions; for each level of disorder five models are analyzed.

		$E^*/E_s \times 10^{-2}$					
		Simple Cubic			Kelvin		
		min.	max.	avg.	min.	max.	avg.
[001]	$\delta = 0$ (regular)	-	-	6.630	-	-	1.109
	$\delta = l/16$	6.516	6.528	6.524	1.100	1.104	1.103
	$\delta = l/8$	6.192	6.242	6.219	1.081	1.085	1.083
	$\delta = l/4$	5.178	5.260	5.211	1.011	1.035	1.024
	$\delta = 3l/8$	4.072	4.151	4.103	0.894	0.912	0.905
[021]	$\delta = 0$ (regular)	-	-	1.193	-	-	1.140
	$\delta = l/16$	1.197	1.199	1.198	1.132	1.135	1.134
	$\delta = l/8$	1.207	1.213	1.210	1.111	1.115	1.113
	$\delta = l/4$	1.242	1.268	1.249	1.038	1.046	1.044
	$\delta = 3l/8$	1.174	1.304	1.238	0.911	0.929	0.918
[011]	$\delta = 0$ (regular)	-	-	0.816	-	-	1.158
	$\delta = l/16$	0.820	0.821	0.820	1.149	1.152	1.150
	$\delta = l/8$	0.831	0.834	0.833	1.125	1.131	1.128
	$\delta = l/4$	0.867	0.889	0.875	1.053	1.059	1.056
	$\delta = 3l/8$	0.843	0.940	0.891	0.914	0.932	0.923
[111]	$\delta = 0$ (regular)	-	-	0.631	-	-	1.174
	$\delta = l/16$	0.634	0.636	0.635	1.165	1.169	1.167
	$\delta = l/8$	0.644	0.647	0.645	1.138	1.145	1.142
	$\delta = l/4$	0.671	0.681	0.680	1.056	1.068	1.065
	$\delta = 3l/8$	0.700	0.715	0.708	0.913	0.950	0.928

present elastic predictions, where [111] yields the highest Young's modulus and [011] has an intermediate value.
From the deformed KV structures (not shown) no localization is obvious. For all cases the distributions of the deformations are rather homogeneous over the height of the samples.

Influence of Structural Disorder

Now, the influence of structural disorder on the global stress–strain behavior and on the deformation localization is investigated. Again, five models for each level of disorder are generated and analyzed. Analyses are performed for lattice orientations [001], [021], [011], and [111].

Figure 3.5 shows the predicted deformations of the SC models with structural disorder of different degree (together with the regular structures) under uniaxial compression for the selected lattice orientations. For small levels of disorder the behavior is similar to the regular structures and the deformation localizations occur in the same manner. With increasing disorder the localizations are less obvious and at pronounced disorder no localization can be seen in the deformed structures of all orientations.

Figure 3.6 shows the corresponding stress-strain curves for these cases. The predictions for all five realizations of each single case are shown. Inspection of the [001] orientation reveals, at first, the previous result that for increasing disorder the stiffness of the structures decreases. With increasing deviation of the vertices from their location in the regular structure the governing deformation mechanism changes from pure axial compression in the struts to a mixed mode with increasing bending contribution. As for the stiffness, the peak load is reduced and shifted to higher strains for increased disorder. Also the load drop following the maximum load is less pronounced, resulting in a higher load carrying capacity at greater displacements. For the [021], [011], and [111] orientations the same trends can be seen, but in a much less pronounced way. The structures tend to exhibit more compliant behavior and lower strength with increasing disorder, and the load drop after the peak is less pronounced. Note that the linear elastic behavior as discussed earlier, here, is superimposed by nonlinear effects.

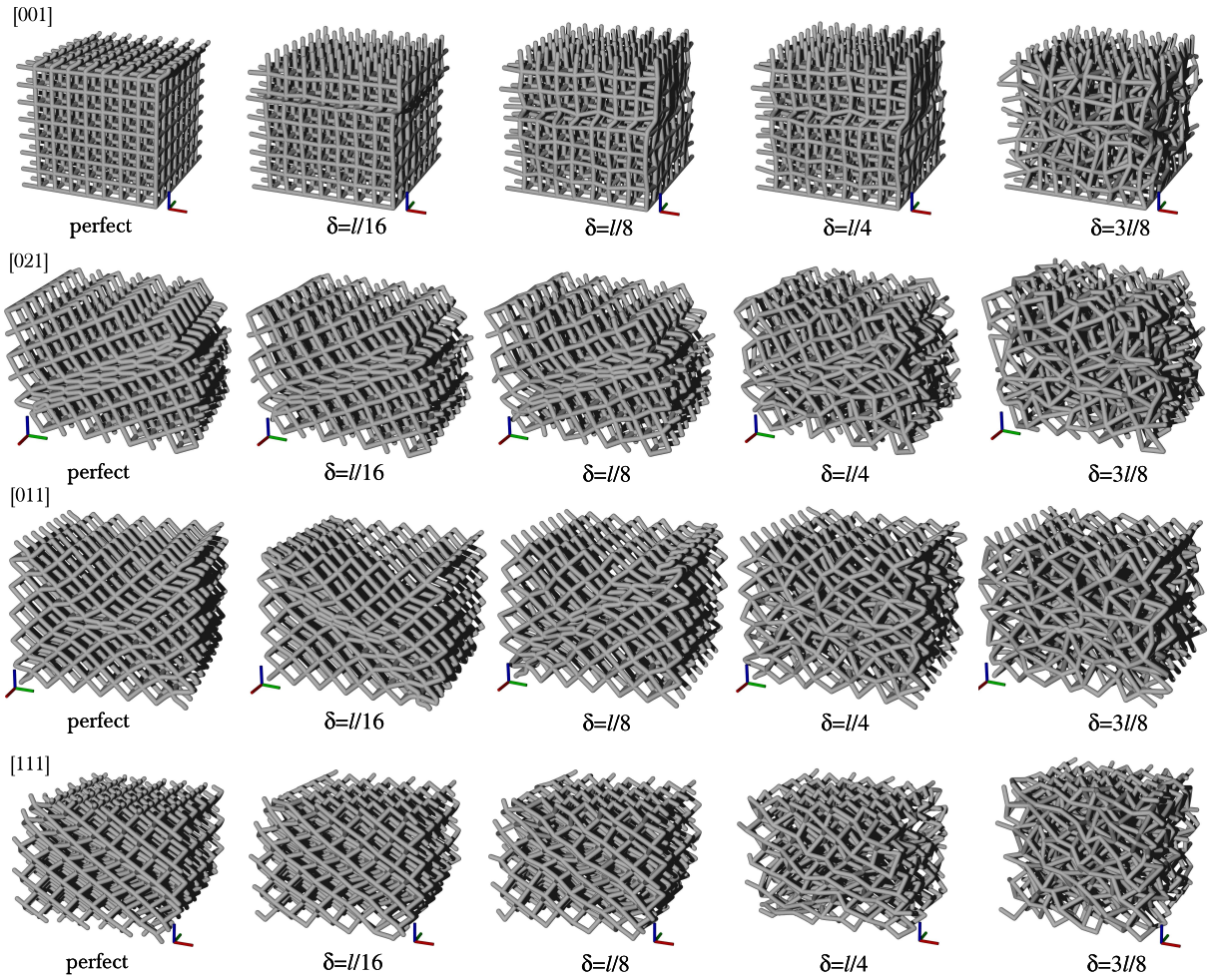

Figure 3.5 Predicted deformation patterns (without deformation scaling) of Simple Cubic finite structures under uniaxial vertical compression for increasing disorder, δ, (from left to right) and for lattice orientations [001], [021], [011], and [111] (from top to bottom).

For the KV structures the predicted overall stress–strain diagrams for various levels of disorder are given in Figure 3.7. For all orientations the introduced disorder leads to a moderate decrease of the peak loads. The qualitative behavior is not affected by the disorder. These results support the previous finding that KV structures, in general, are not susceptible to deformation localization.

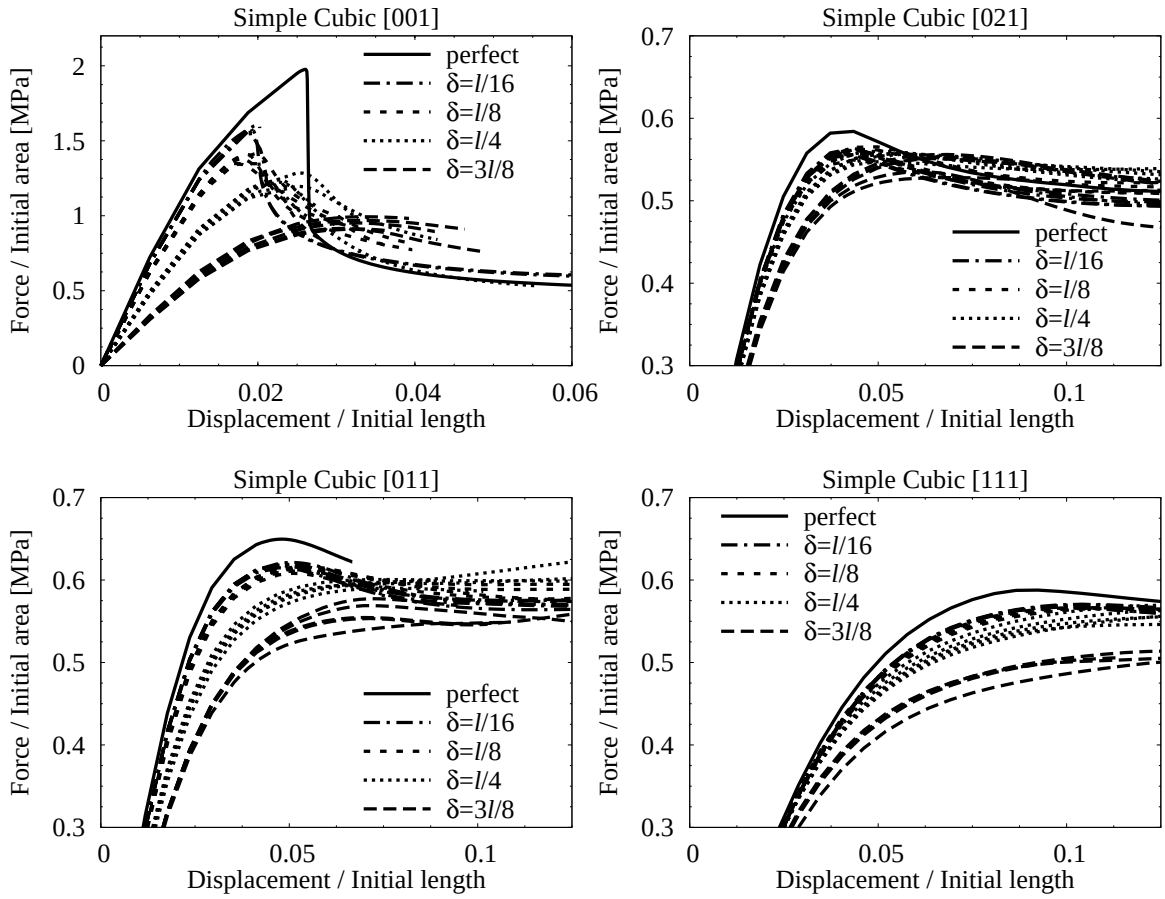

Figure 3.6 Predicted overall stress–strain curves of Simple Cubic finite structures with different levels of disorder, δ, for lattice orientations [001], [021], [011], and [111] with respect to uniaxial compression.

Mesoscopic Strain Rates

The evaluation of the mesoscopic compressive strain rates in load direction, $\bar{\varepsilon}_{33}$, over the macroscopic compressive strain in load direction, Γ_{33}, for regular and disordered structures and different lattice orientations are shown in the left columns of Figures 3.8 to 3.11. In addition, the elastic strain energy density, u_{el}, the plastic dissipation energy density, u_{pl}, and the total mechanical energy density, u_{tot}, are shown in the figures (for a discussion of the energy evolution see Section 3.3.3). The corresponding distributions of the mesoscopic strain rates within the structures at selected macroscopic strains are shown aside. For

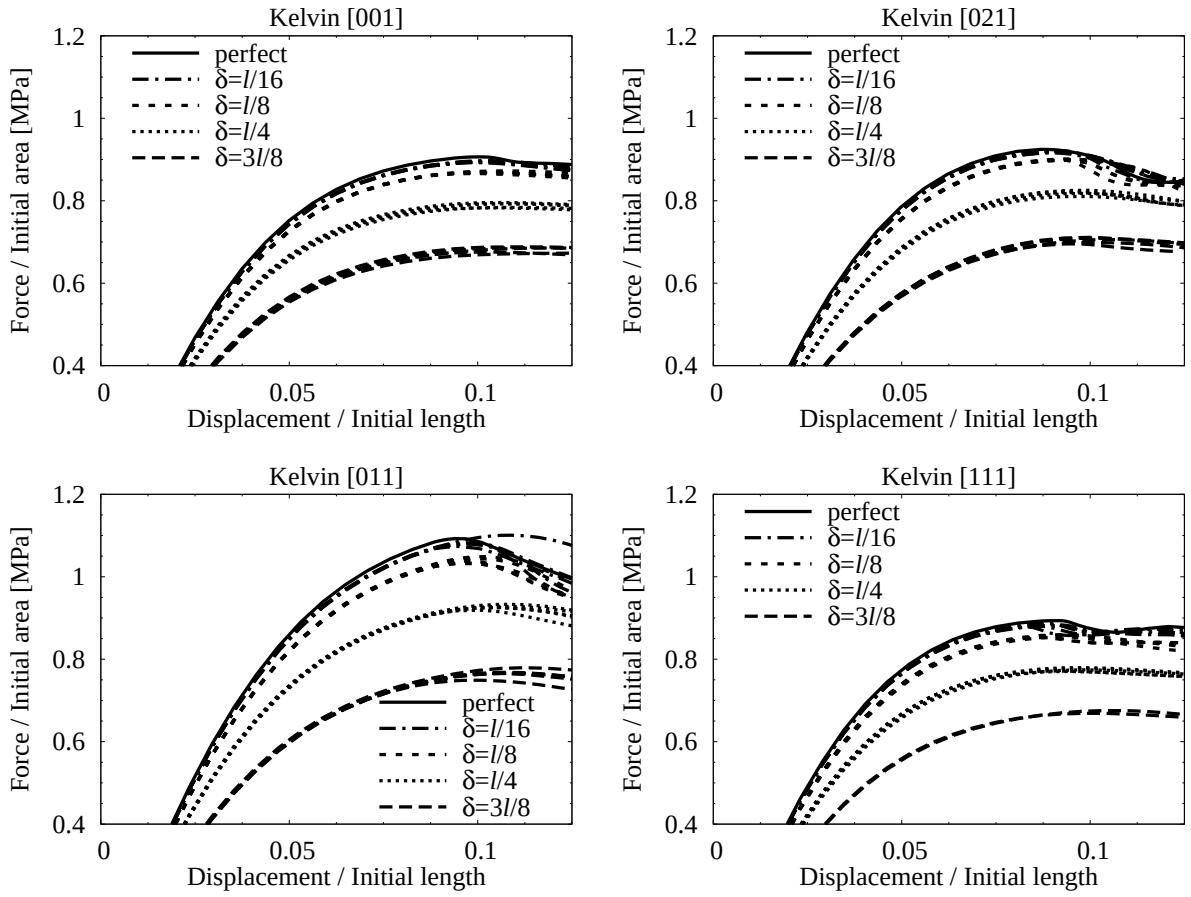

Figure 3.7 Predicted overall stress–strain curves of Kelvin finite structures with different levels of disorder, δ, for lattice orientations [001], [021], [011], and [111] with respect to uniaxial compression.

each level of disorder the results of one representative sample out of the five simulated disordered structures is discussed.

In Figure 3.8 the evaluation of the mesoscopic strain rate $\bar{\varepsilon}_{33}$ for structures with lattice orientation [001] is shown. For the regular structure (top row) at a macroscopic strain of $\Gamma_{33} \approx 0.026$ the values of $\bar{\varepsilon}_{33}$ for a small fraction of vertex pairs rapidly increase ($\bar{\varepsilon}_{33} > 20$, not shown in the histogram) whereas the values of $\bar{\varepsilon}_{33}$ of the larger part of the vertex pairs decrease (thin lined curve in the histogram). This behavior accompanies the beginning of localization. After the collapse of cells has started, two branches with different mesoscopic strain rates in load direction are observed. The upper branch corresponds to the vertex pairs within the localization zone. The lower branch corresponds to the remaining observed

vertex pairs.

In the case of a disorder of level $\delta = l/8$ (Figure 3.8, middle row) localization starts at $\Gamma_{33} \approx 0.0175$. An increase of $\bar{\varepsilon}_{33}$ in a small fraction of vertex pairs can be observed while the larger fraction shows a decrease of $\bar{\varepsilon}_{33}$. As in the regular case, two branches can be observed, but the disorder results in smaller mesoscopic strain rates and a much wider scatter of $\bar{\varepsilon}_{33}$.

No distinct increase or decrease of the mesoscopic strain rates is found for a disorder of level $\delta = 3l/8$ (Figure 3.8, bottom row). The values of $\bar{\varepsilon}_{33}$ increase continuously for a fraction of vertex pairs, but they do not establish a contiguous domain. No sudden change of a notable fraction of pairs is observed, i.e. in this case the structural disorder prevents localization of deformation.

Figure 3.9 shows the evaluation of $\bar{\varepsilon}_{33}$ for the structures with lattice orientation [021]. For the regular case (top row) two branches with different mesoscopic strain rates in load direction are observed during the first phase of the deformation. The lower branch corresponds to the domains in which the strut deformation is constrained by the rigid top and bottom plates. The upper branch corresponds to the vertex pairs in between the regions influenced by the plates. At $\Gamma_{33} \approx 0.025$ the mesoscopic strain rate distribution splits into three branches and localization of a contiguous domain starts. The upper branch corresponds to the collapsing cells within the localization domain, i.e. two layers of cells [Luxner et al., 2006a]. The middle branch accords with the vertex pairs between the localization domain and the region influenced by the top and bottom plates. The cells in these domains show a decrease of $\bar{\varepsilon}_{33}$, i.e. unloading at the mesoscopic level. The lower branch corresponds to all other vertex pairs, which are slightly affected by the global deformation or deform at a constant rate, respectively. After unloading in some domains has finished the middle branch merges with the lower branch and the corresponding cells deform at a constant rate close to zero.

In the case of $\delta = l/8$ (Figure 3.9, middle row) a similar behavior can be seen, but localization starts at $\Gamma_{33} \approx 0.045$, which is higher than in the regular case. Again, three branches, but with a wider scatter of $\bar{\varepsilon}_{33}$, are present during localization.

The structures with $\delta = 3l/8$ (Figure 3.9, bottom row) do not show localization. A wide

scatter of $\bar{\varepsilon}_{33}$ can be seen and only single struts collapse which do not form a contiguous region.

The results of structures with lattice orientation [011] are shown in Figure 3.10. In the regular case (top row) regions with increasing and decreasing mesoscopic strain rates can be identified at a macroscopic strain of approximately 0.045, suggesting localization and unloading in some regions, respectively. The unloading in some regions is more pronounced than the localization.
For the [011] structures with a disorder of level $\delta = l/8$ (Figure 3.10, middle row) still regions with increasing and decreasing mesoscopic strain rates are observed, i.e. localization and unloading at a macroscopic strain of about 0.050 is suggested, however, with a wider scatter of $\bar{\varepsilon}_{33}$ compared to the corresponding regular structure.
No localization is observed for the highly disordered structures with lattice orientation [011] (Figure 3.10, bottom row). Only single struts in non-connected regions localize, which can be seen from the increase of $\bar{\varepsilon}_{33}$ for some struts in Figure 3.10, bottom row.

Structures with lattice orientation [111] are evaluated in Figure 3.11. The histogram for the regular structures (top row) shows two peaks at a macroscopic strain of approximately 10% (thick lined curve). This indicates two regions with different values of $\bar{\varepsilon}_{33}$. Together with the observed splitting of $\bar{\varepsilon}_{33}$ at $\Gamma_{33} \approx 0.088$ localization is suggested. No regions with increasing and decreasing mesoscopic strain rates can be identified for the structures with perturbation levels $\delta = l/8$ and $\delta = 3l/8$ (Figure 3.11, middle and bottom row). The structural disorder prevents the initiation of deformation localization.

Total Energy Distribution

In the following the spatial energy distribution at the level of individual Finite Elements within regular and disordered SC structures is discussed by means of energy histograms.

For the case of a regular SC structure oriented in [001] and following the trivial path (no localization), the histogram would exhibit a bi-modal distribution (not shown). Two thirds of the elements are oriented perpendicularly to the loading direction and contain nearly zero energy. The remaining 1/3 of the elements are aligned with the load. They share the

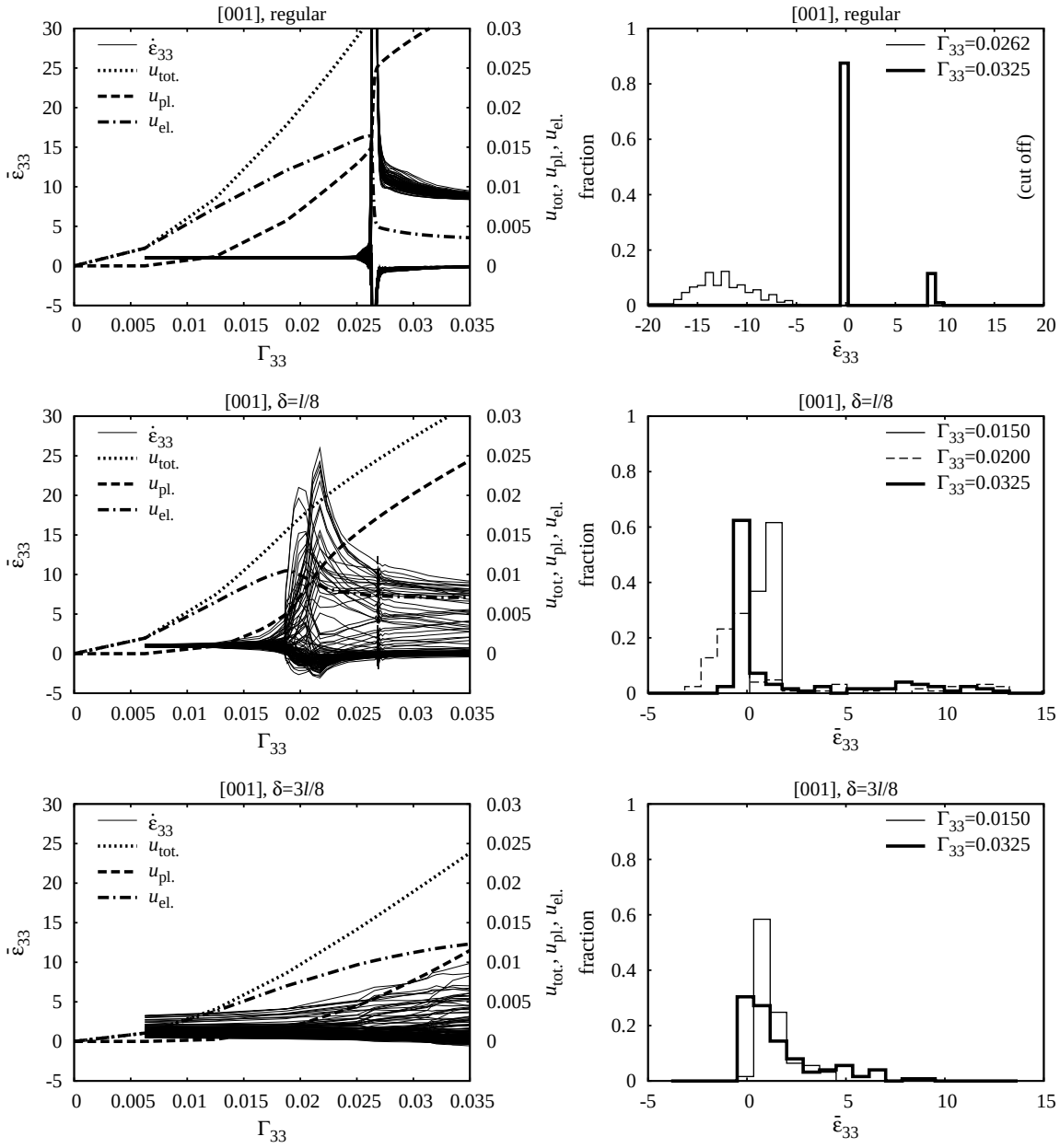

Figure 3.8 Evolution of the mesoscopic strain rate, $\bar{\varepsilon}_{33}$, elastic strain energy density, u_{el}, plastic dissipation energy density, u_{pl}, and total energy density, u_{tot}, over the macroscopic sample strain, Γ_{33}, for regular and disordered Simple Cubic structures with lattice orientation [001] (left column); corresponding distributions of the mesoscopic strain rates within the structure at selected macroscopic strains (right column).

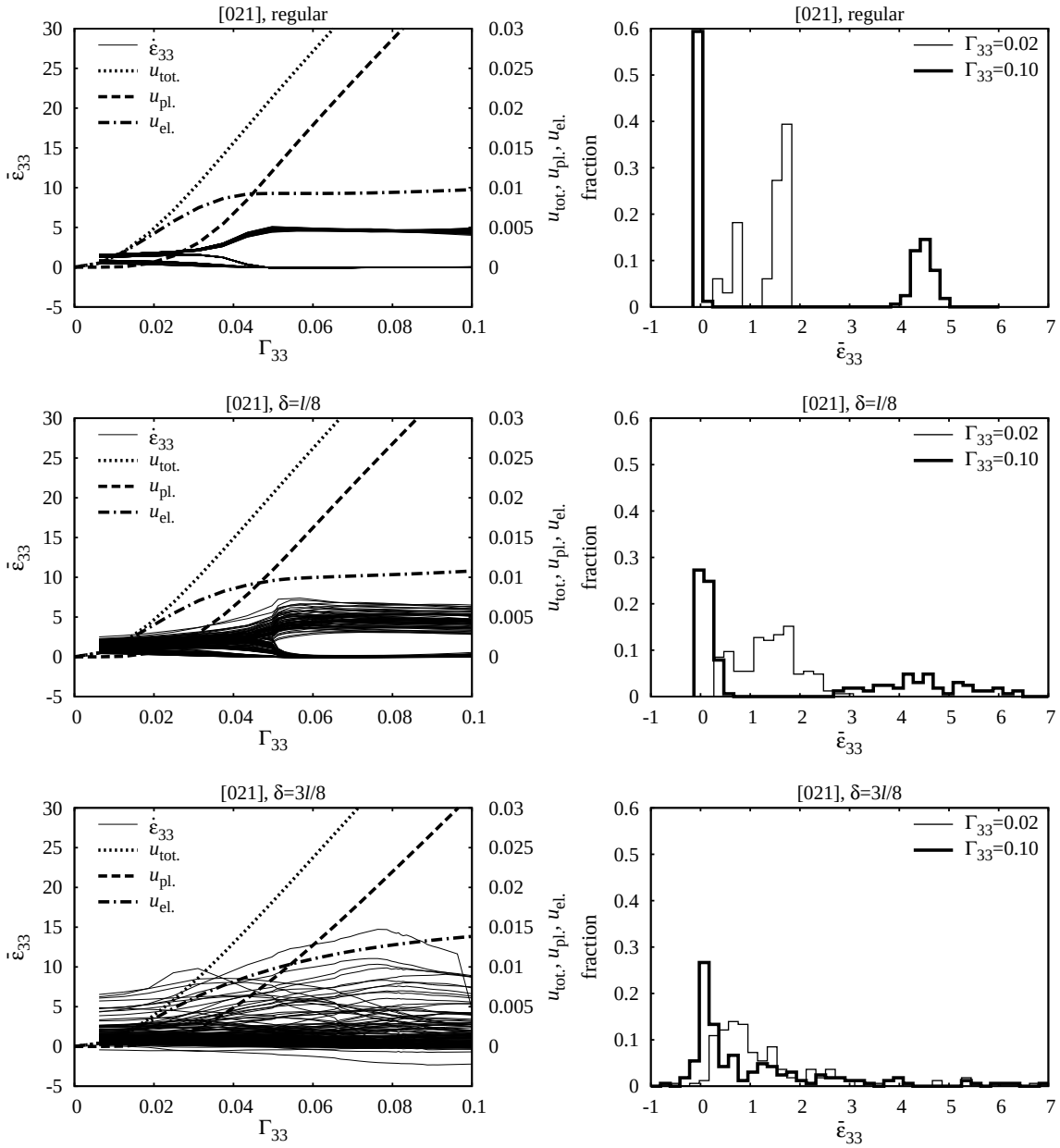

Figure 3.9 Evolution of the mesoscopic strain rate, $\bar{\varepsilon}_{33}$, elastic strain energy density, u_{el}, plastic dissipation energy density, u_{pl}, and total energy density, u_{tot}, over the macroscopic sample strain, Γ_{33}, for regular and disordered Simple Cubic structures with lattice orientation [021] (left column); corresponding distributions of the mesoscopic strain rates within the structure at selected macroscopic strains (right column).

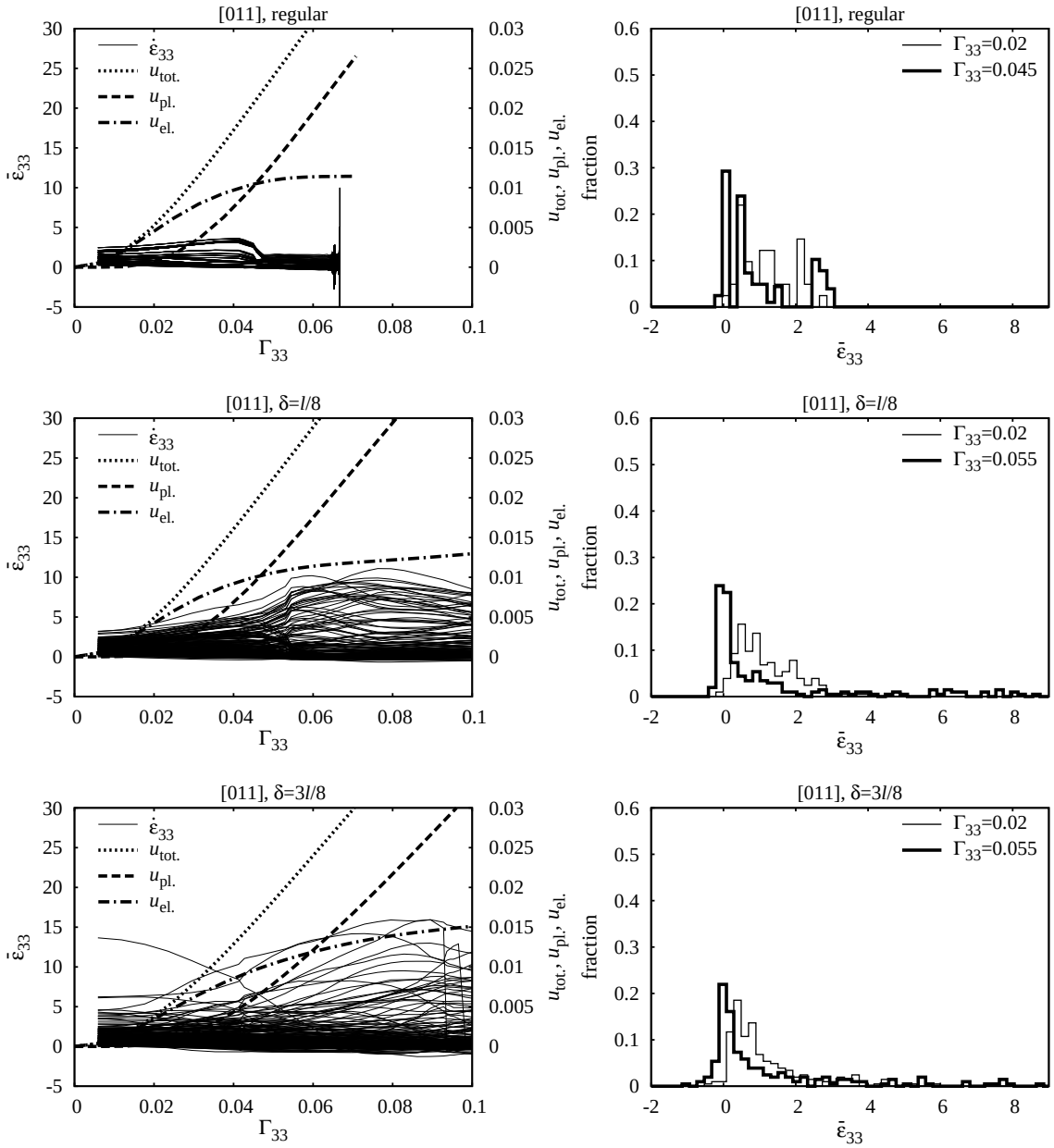

Figure 3.10 Evolution of the mesoscopic strain rate, $\bar{\varepsilon}_{33}$, elastic strain energy density, u_{el}, plastic dissipation energy density, u_{pl}, and total energy density, u_{tot}, over the macroscopic sample strain, Γ_{33}, for regular and disordered Simple Cubic structures with lattice orientation [011] (left column); corresponding distributions of the mesoscopic strain rates within the structure at selected macroscopic strains (right column).

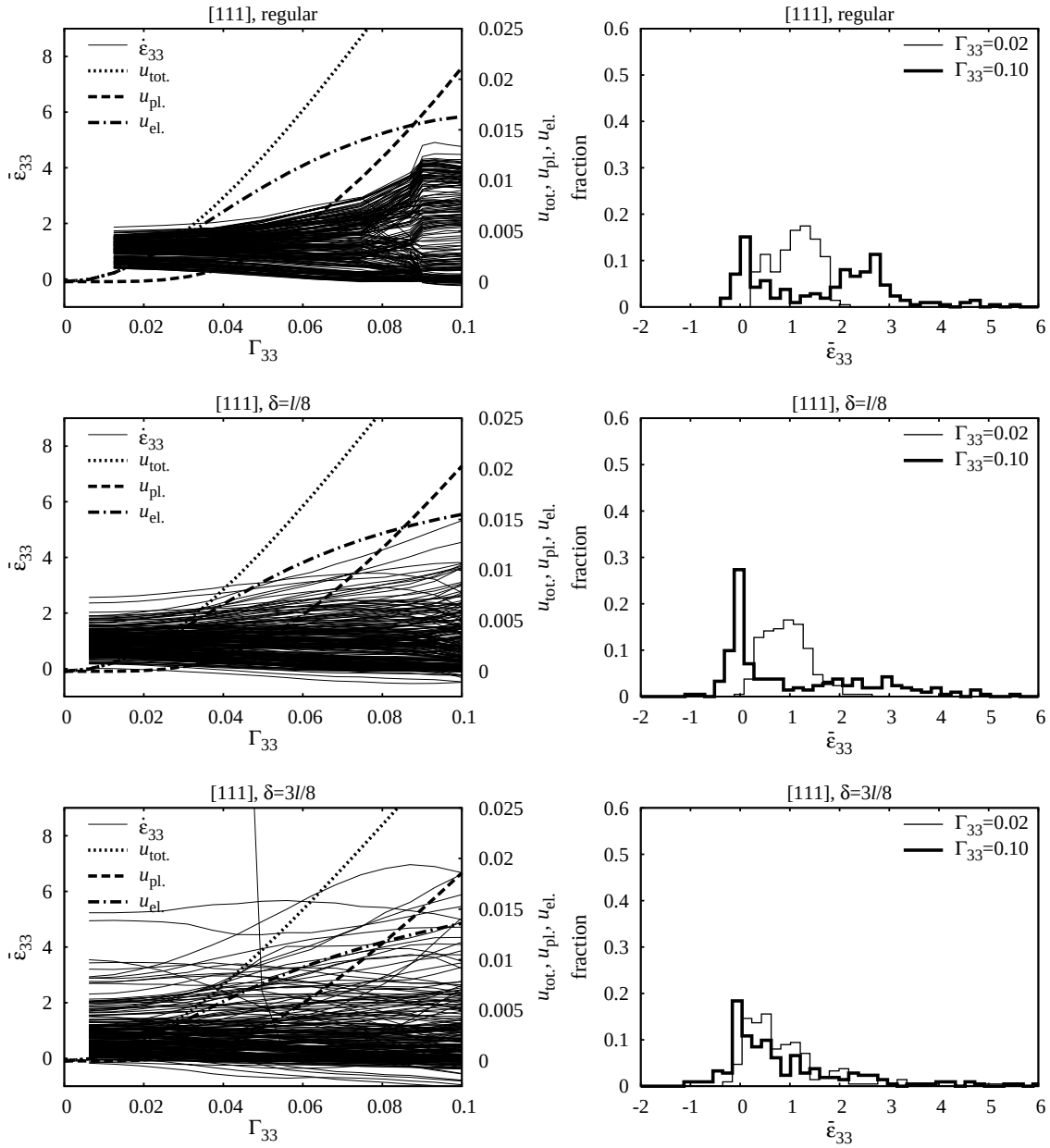

Figure 3.11 Evolution of the mesoscopic strain rate, $\bar{\varepsilon}_{33}$, elastic strain energy density, u_{el}, plastic dissipation energy density, u_{pl}, and total energy density, u_{tot}, over the macroscopic sample strain, Γ_{33}, for regular and disordered Simple Cubic structures with lattice orientation [111] (left column); corresponding distributions of the mesoscopic strain rates within the structure at selected macroscopic strains (right column).

energy evenly, resulting in a second peak in the histograms. Note that for this case the normalized energy is not changing with increasing overall deformation.

In contrast to the trivial solution, the consideration of the post-buckling path of the regular structure gives rise to a different energy histogram. After bifurcation a fraction of the elements experiences considerably higher energies. These values are isolated from the rest, show no scatter, and are rising with increasing overall deformation. In the present example this effect concerns about 1/8 of the load aligned elements. The energy distribution of the other elements is mostly unchanged.

Introduction of a small structural disorder ($\delta = l/16$) yields a similar appearance of the histogram, with less pronounced peaks, see Figure 3.12. Increasing the structural disorder results in a wider region of localization and being less pronounced. Consequently, the high energy peaks in the histograms move to lower values, become wider, and concern more elements. When the structural disorder is large enough so that localization does not occur at all, the high energy peaks disappear completely. Their energy level is reduced until they are "absorbed" into the low energy peaks, eventually. The latter, simultaneously, become more spread out as the disorder increases. The resulting histogram is shown in Figure 3.13 for the $\delta = 3l/8$ case.

Here, only the SC structure loaded in principal directions is discussed with respect to the effects of structural disorder. These examples are considered as extreme cases showing all particular features, to which, to a certain extent, all other cases resemble.

3.3.3 Overall Energy Considerations

The development of the elastic strain energy density, u_{el}, plastic dissipation energy density, u_{pl}, and total energy density, u_{tot}, of structures with different lattice orientations and different levels of disorder is plotted in the left columns of Figures 3.8 to 3.11. In addition the corresponding values at maximum stress $\Sigma_{33,\mathrm{max}}$ are documented in Figure 3.14 and Table 3.3.

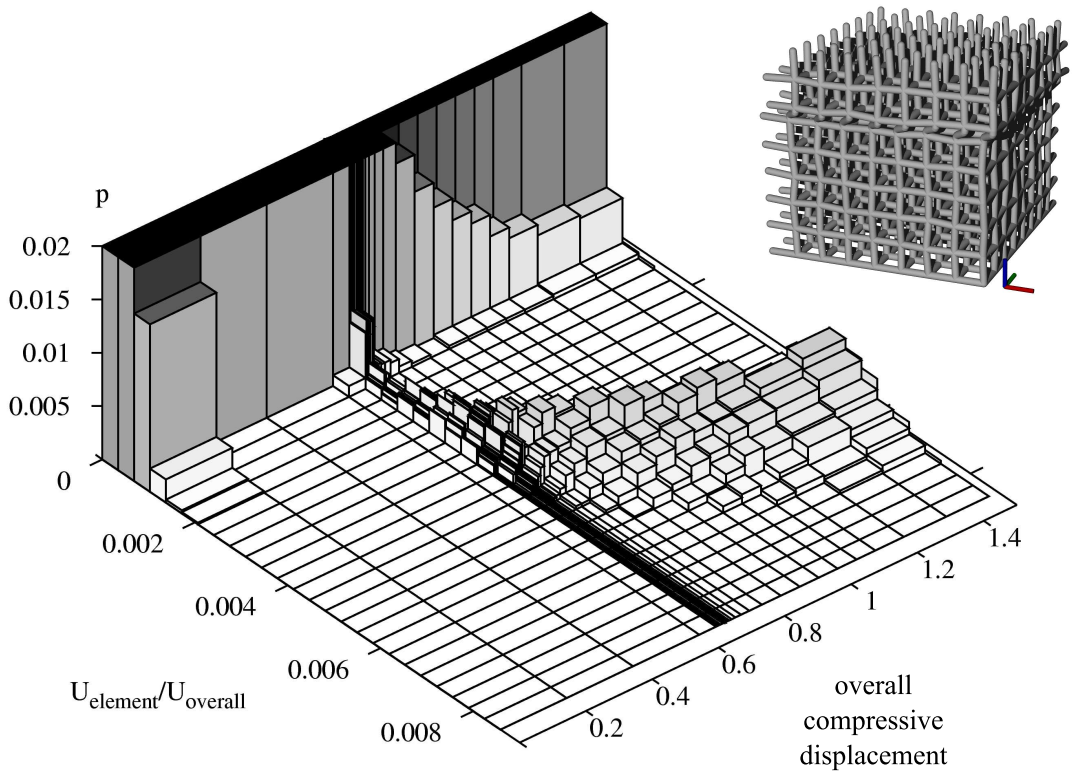

Figure 3.12 Predicted energy distribution in the course of uniaxial compression of a disordered ($\delta = l/16$) Simple Cubic finite structure with lattice orientation [001]; total energy within each Finite Element normalized by the overall work, $U_{\text{element}}/U_{\text{overall}}$, vs. fraction of elements, p, (cut off at $p = 0.02$).

In the case of structures with lattice orientation [001] both, regular structures and structures with a disorder of level $\delta = l/8$ show a drop of elastic strain energy density after localization has started (Figure 3.8, top and middle row). This indicates that part of the elastic strain energy is dissipated plastically. The elastic strain energy is released in the non-localizing regions, i.e. during unloading. This phenomenon is very pronounced for the regular case. Here, the main part of the elastic strain energy is converted suddenly to plastic dissipation energy.

For $\delta = 3l/8$ (Figure 3.8, bottom row), however, the elastic strain energy constantly increases. This is further evidence that for the structures with lattice orientation [001] and disorder $\delta = 3l/8$ localization is not an issue.

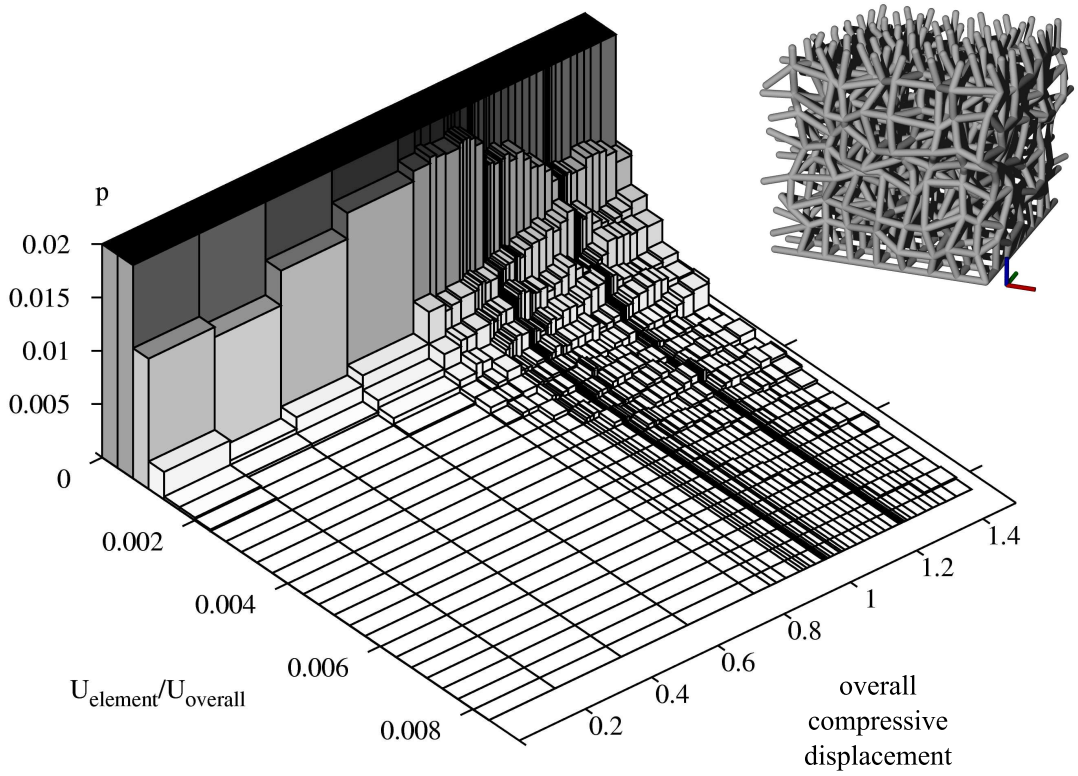

Figure 3.13 Predicted energy distribution in the course of uniaxial compression of a disordered ($\delta = 3l/8$) Simple Cubic finite structure with lattice orientation [001]; total energy within each Finite Element normalized by the overall work, $U_{\text{element}}/U_{\text{overall}}$, vs. fraction of elements, p, (cut off at $p = 0.02$).

From Table 3.3 and Figure 3.14 it can be seen that, compared to the regular case, disorder of level $\delta = l/8$ results in a decrease of the total energy until the maximum stress $\Sigma_{33,\max}$ is reached. On the other hand the amount of absorbable energy increases with increasing levels of perturbation.

Compared to the corresponding regular structure, the structures with lattice orientation [021] and perturbation level $\delta = l/8$ (Figure 3.9, middle row) do not show a significant change of u_{tot}, whereas the structures with $\delta = 3l/8$ (Figure 3.9, bottom row) show an average increase of u_{tot} by 50%, while $\Sigma_{33,\max}$ decreases by 6.7%, see Table 3.3. The increase of u_{tot} is due to a marked increase of Γ_{33} at $\Sigma_{33,\max}$. The plastic dissipation energy density, u_{pl}, increases by 78.5%.

Compared to the corresponding regular structure, no significant change of the energy densities is observed for the structures with lattice orientation [011] and $\delta = l/8$ (Figure 3.10, middle row). The structures with $\delta = 3l/8$ (Figure 3.10, bottom row) show an average increase of 51.4% for u_{tot} at a decrease of $\Sigma_{33,\mathrm{max}}$ of 13.7%; the increase of u_{tot} is due to a strong increase of $\Gamma_{33}(\Sigma_{33,\mathrm{max}})$, see Table 3.3. The plastic dissipation energy density increases by 70.8%.

A significant increase of the energy densities for all levels of disorder of structures with lattice orientation [111] can be seen. Structures with disorder $\delta = 3l/8$ (Figure 3.11, bottom row) show an increase of 34% for u_{tot} at a decrease of $\Sigma_{33,\mathrm{max}}$ of 14.2%; the plastic dissipation energy density u_{pl} increases by 70.8%, see Table 3.3. The amount of u_{el} decreases slightly. This is the only case for which an increase of u_{tot} is not associated with an increase of u_{el}.

3.3.4 Influence of the Relative Density

The studies within this chapter are carried out under the premise of a single relative density which is kept constant for all investigations. Since the introduction of structural disorder gives rise to longer struts in average, i.e. the relative density would increase, their diameters have to be adjusted accordingly to keep the relative density constant. The effect on the behavior when keeping the struts' diameter constant is discussed in the following example.

The SC structure with a disorder of level $\delta = 3l/8$ and no diameter correction increases its relative density from 12.5% to 13.8%. For the case of the [001] lattice orientation without a diameter correction the predicted peak load would suggest a maximum peak load that is 22% higher than for the structure with diameter correction.

3.4 Conclusions

In this chapter the mechanical properties of porous open cell structures made from elastic-plastic bulk material are investigated by Finite Element simulations. Six regular three–

Table 3.3 Comparison of elastic strain energy density, u_{el}, plastic dissipation energy density, u_{pl}, and total energy density, u_{tot}, at maximum stress, $\Sigma_{33,\max}$, for different lattice orientations and different levels of disorder of a Simple Cubic structure. For the disordered cases the values of $\Sigma_{33,\max}$, $\Gamma_{33}(\Sigma_{33,\max})$, u_{el}, u_{pl}, and u_{tot} are the averaged values of five different randomizations. The values in the brackets are the standard deviations. The percentages refer to the regular case.

				energy densities at $\Sigma_{33,\max}$		
		$\Sigma_{33,\max}$ [MPa]	$\Gamma_{33}(\Sigma_{33,\max})$	u_{el} [MJ/m^3]	u_{pl} [MJ/m^3]	u_{tot} [MJ/m^3]
[001]	regular	1.976E+00	2.601E-02	1.641E-02	1.441E-02	3.082E-02
	$\delta = l/8$	1.382E+00	1.803E-02	1.007E-02	4.419E-03	1.449E-02
				(±6.15E-04)	(±1.24E-03)	(±1.84E-03)
		-30.06%	-30.66%	-38.63%	-69.33%	-52.98%
	$\delta = 3l/8$	9.484E-01	3.240E-02	1.142E-02	8.968E-03	2.039E-02
				(±5.43E-04)	(±1.22E-03)	(±1.74E-03)
		-52.01%	+24.58%	-30.42%	-37.75%	-33.84%
[021]	regular	5.841E-01	4.348E-02	9.103E-03	8.510E-03	1.761E-02
	$\delta = l/8$	5.585E-01	4.472E-02	8.905E-03	8.471E-03	1.738E-02
				(±3.50E-04)	(±1.32E-03)	(±1.64E-03)
		-4.39%	+2.86%	-2.17%	-0.45%	-1.34%
	$\delta = 3l/8$	5.447E-01	6.610E-02	1.126E-02	1.519E-02	2.645E-02
				(±5.38E-04)	(±1.10E-03)	(±1.61E-03)
		-6.76%	+52.03%	+23.74%	+78.45%	+50.17%
[011]	regular	6.847E-01	5.085E-02	9.805E-03	1.225E-02	2.206E-02
	$\delta = l/8$	6.463E-01	5.544E-02	9.942E-03	1.323E-02	2.317E-02
				(±1.48E-04)	(±5.76E-04)	(±7.00E-04)
		-5.62%	+9.01%	+1.39%	+7.93%	+5.02%
	$\delta = 3l/8$	5.909E-01	8.298E-02	1.248E-02	2.092E-02	3.341E-02
				(±7.17E-04)	(±7.77E-03)	(±8.45E-03)
		-13.70%	+63.17%	+27.31%	+70.75%	+51.44%
[111]	regular	5.270E-01	9.938E-02	2.045E-02	2.653E-02	4.698E-02
	$\delta = l/8$	5.074E-01	1.143E-01	2.051E-02	3.404E-02	5.455E-02
				(±2.41E-04)	(±1.79E-03)	(±2.01E-03)
		-3.72%	+15.00%	+0.30%	+28.33%	+16.13%
	$\delta = 3l/8$	4.524E-01	1.404E-01	1.991E-02	4.302E-02	6.293E-02
				(±8.43E-04)	(±7.13E-03)	(±7.93E-03)
		-14.15%	+41.24%	-2.63%	+62.15%	+33.96%

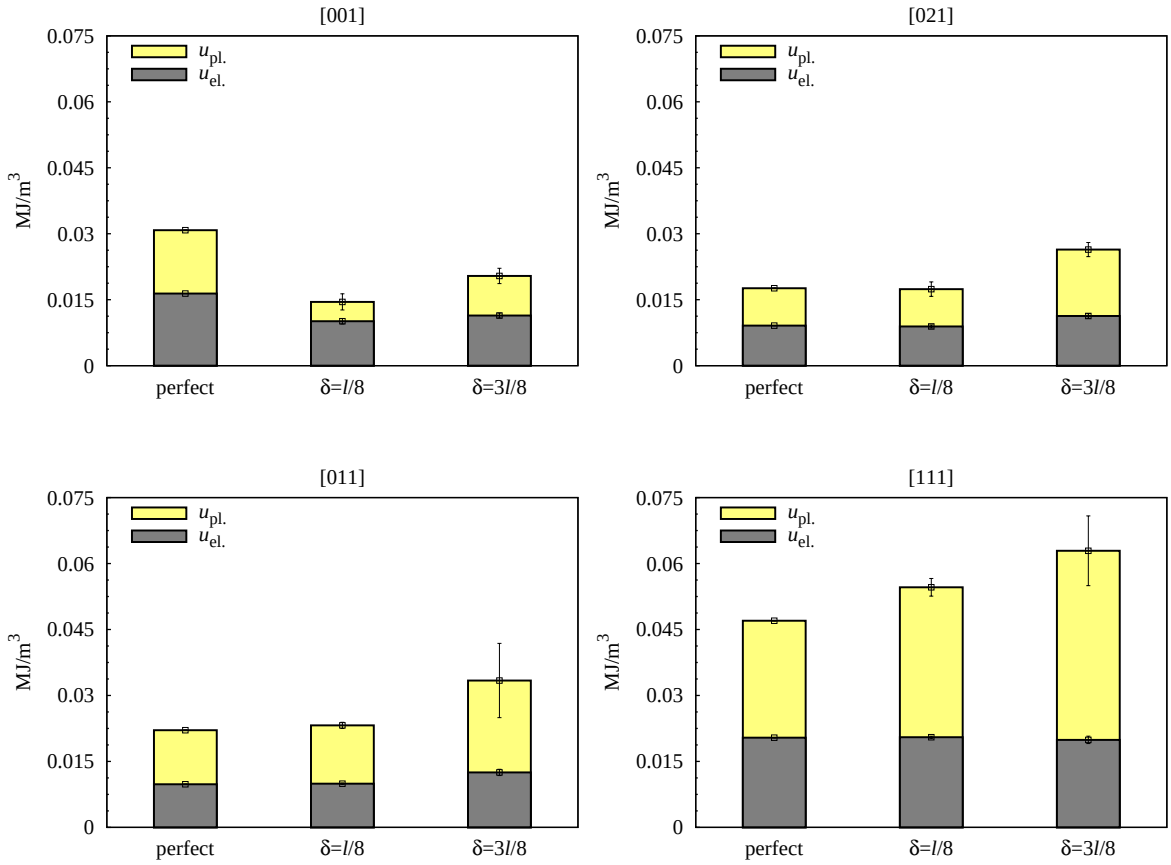

Figure 3.14 Comparison of elastic strain energy density, u_{el}, and plastic dissipation energy density, u_{pl}, at maximum stress, $\Sigma_{33,\max}$, for different lattice orientations and different perturbation levels, δ, of a Simple Cubic structure. For the disordered cases the values are the averages of five different randomizations, the error bars indicate the standard deviation.

dimensional generic structures are modeled by a unit cell approach and the entire elastic tensors are predicted. Out of these six, the Simple Cubic and the Kelvin type structures are studied further.

Various degrees of structural disorder are introduced while the density is kept constant and the effect on the elastic behavior is predicted. For the Simple Cubic structure disorder leads to a decrease of anisotropy. The Young's moduli in the principal structure directions are reduced, while in the other directions the stiffness increases. For the most disordered model investigated a remarkable degree of anisotropy is still left. The Kelvin type structure shows the lowest elastic anisotropy among the regular geometries studied. The disorder gives rise

to a moderate decrease of the Young's moduli in all directions. For the highest degree of disorder cubic material symmetry is no longer obvious from the plots of orientation dependent stiffnesses.

The nonlinear mechanical behavior of the Simple Cubic and the Kelvin structures is analyzed. The effect of the structural disorder on the localization of the deformation is studied under uniaxial compression. For large finite samples the overall stress–strain response is predicted for different lattice orientations. Histograms which show the statistical distribution of the total energy and the mesoscopic strain rates in the structures are used to assess the localization behavior.

For regular and slightly disordered Simple Cubic type geometries a distinct localization is observed. The localization patterns are characteristic for the lattice inclination with respect to the loading direction. With increasing levels of disorder the localization regions become less "sharp". At the highest level of disorder investigated localization no longer occurs in Simple Cubic structures. For the selected lattice orientations an increase of disorder decreases the peak loads and gives rise to a smoother overall stress–strain behavior. This is most pronounced for loading parallel to the principal lattice orientation of the Simple Cubic structure.

The Kelvin structure does not exhibit a marked direction dependence of the mechanical properties in the nonlinear regime. Structural disorder decreases the overall stress–strain response for all selected orientations. Localization is not found for the Kelvin type models. Introduction of structural disorder drives the Kelvin structures towards isotropic behavior with respect to elasticity and strength.

Structural disorder has a marked effect on the Simple Cubic structures. The orientation dependence is decreased as well as the tendency to develop deformation localization. This is beneficial for energy absorption applications or when pronounced anisotropy and localization are considered detrimental. Kelvin structures in general are found to be close to isotropic. Disorder does not change the behavior since the regular Kelvin structure already exhibits a quite complex geometry.

If the service load is known to be uniaxial compression of a determined direction Simple Cubic structures with disorder may be advantageous. However, if a predominant loading direction is not known, Kelvin structures appear to be preferable. The peak load level in the weakest direction for Simple Cubic is lower than for Kelvin.

Note that these conclusions are based on uniaxial compressive load cases. For multiaxial loading scenarios additional simulations are likely to be required.

Furthermore, it is noted that the shape and the size of the simulated finite structure models have an effect on the results. Larger samples and samples with different shapes may result in differing localization patterns, and variations on the overall responses.

Chapter 4

Influence of Sample Size and Shape

The investigations in Chapters 2 and 3 give rise to the question of how strongly the results are influenced by the geometry and the size of the simulation models. On account of this a new sample geometry is introduced in the current chapter and a comparison to the old sample geometry is presented.

4.1 Introduction

So far, within this work cuboidal structures consisting of 8×8×8 (=512) base cells have been used for the determination of the nonlinear behavior of cellular structures under uniaxial compression.

In the following the investigations are extended to cylindrical structures consisting of about 2650 base cells, see Figure 4.1. The goal is to determine the influence of the size and the shape of samples subjected to uniaxial compression on their mechanical response. This becomes crucial for assessing the results obtained by uniaxial compression tests of samples with limited size, e.g. owing to the fabrication process.

Out of the six generic cellular structures presented in Chapters 2 and 3, the Simple Cubic (SC) structure is selected for further nonlinear studies on account of its distinct anisotropy and its various deformation modes for different lattice orientations. Cuboidal

and cylindrical samples are subjected to uniaxial compression and their nonlinear responses and deformation patterns are compared.

4.2 Methods

4.2.1 Numerical Models

Cylindrical and cuboidal SC structures with lattice orientations [001], [021], [011], and [111] are generated by arranging appropriately rotated base cells. The dimensions of the cuboidal samples are approximately 32 mm × 32 mm × 32 mm, see Section 3.2.2. The diameter of the cylindrical samples is chosen to be 13 base cells, i.e. 52 mm, their height is about 20 base cells, i.e. approximately 80 mm, see Figure 4.1.

Irregular modifications thereof are generated by shifting the vertices of the regular geometries to random positions by a fixed distance, δ, see Section 3.2.2. Irregularities of $\delta/l = 1/8$ and 3/8 are realized for both the cuboidal and the cylindrical samples. Figure 4.1 (middle and bottom row) shows the disordered structures by means of the cylindrical samples. For each value of δ five structures are generated and simulated. Such disorder in the structures, however, increases the strut lengths and, consequently, affects the density. Thus, for representing the desired density the strut diameters are adopted accordingly.

The beam element based modeling technique including adaption of the stiffness and the material distribution in the vicinity of the vertices is employed, see Section 2.2.1. The boundary conditions of the samples are chosen as described in Section 2.3.2.

4.3 Results and Discussion

4.3.1 Overall Stress–Strain Behavior

The overall stress–strain behavior of cuboidal and cylindrical samples is compared to evaluate the influences of free surfaces, load introduction, sample size, and sample shape.

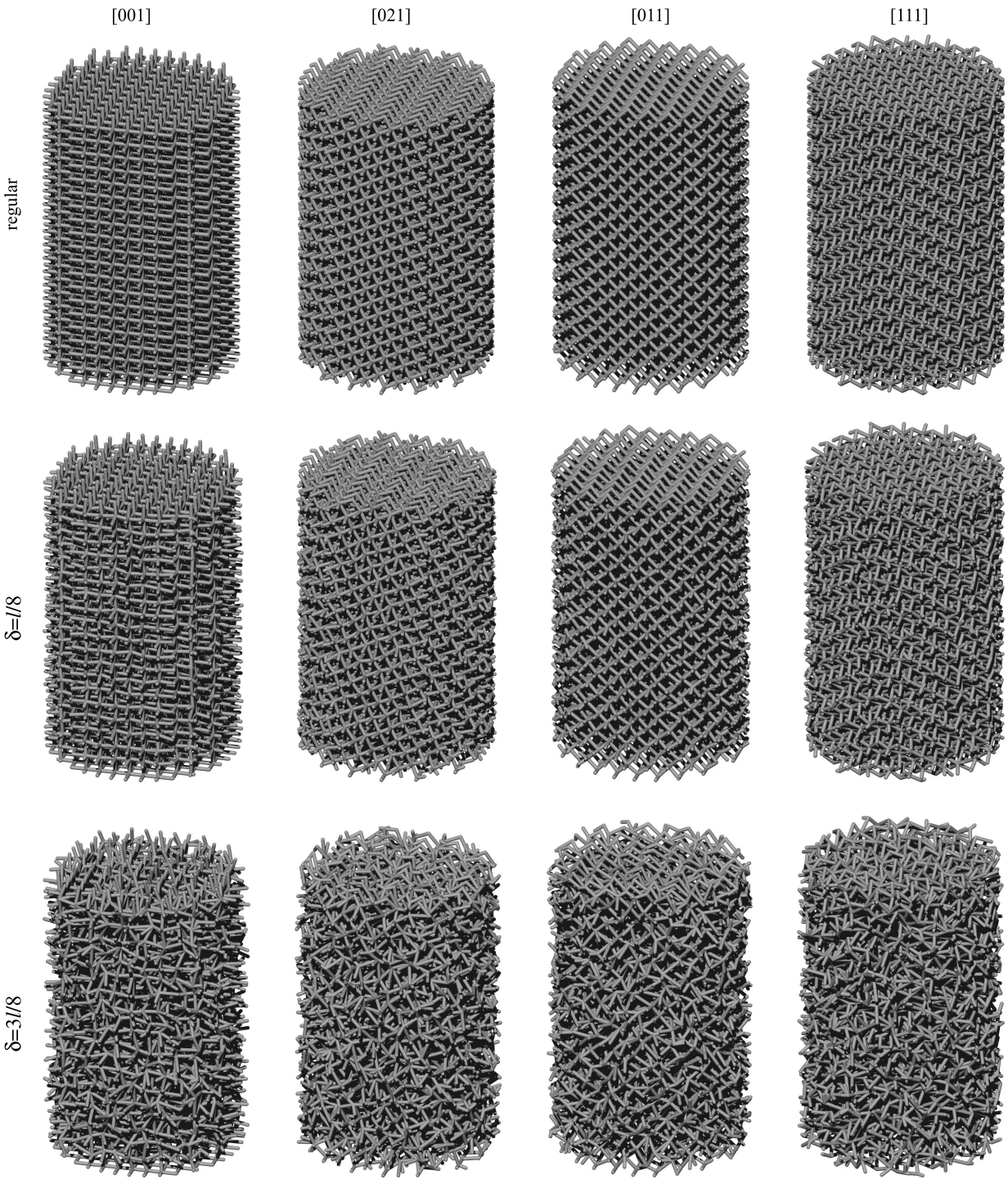

Figure 4.1 Regular and disordered (from top to bottom) Simple Cubic cylindrical samples with lattice orientations [001], [021], [011], and [111] (from left to right).

Figures 4.2 to 4.5 show the predicted overall stress–strain curves of the cylindrical and cuboidal samples with levels of disorder $\delta = l/8$ and $\delta = 3l/8$ for lattice orientations [001], [021], [011], and [111] with respect to uniaxial compression.

It can be seen that the cuboidal and cylindrical structures with lattice orientations [001] and [111] show a very similar overall behavior in terms of stiffness and maximum stress. The steeper drop in the stress–strain curves after the maximum stress for the cylindrical samples with lattice orientation [001] and $\delta = l/8$ is caused by the larger sample size. During localization a fraction of the strain energy stored in the structure is converted into plastic dissipation energy, i.e. unloading takes place in some regions. Due to the larger sample height more strain energy is stored in the cylindrical samples. Hence, more strain energy can be released from the unloading regions and dissipated in the localization plane, resulting in a steeper drop of the stress–strain curve after localization has started.

Variations of the overall stress–strain behavior are observed between cuboidal and cylindrical structures with lattice orientations [021] and [011], see Figures 4.3 and 4.4. Furthermore it can be seen that for lattice orientations [021] and [011] the differences between the samples for the different sample shapes decrease with increasing disorder in the structure. The deviations of the stress–strain curves of the [021] and [011] orientations can be explained by the influence of the rigid top and bottom plates. First, the bending deformations of struts which are connected to the plates are limited due to their rigid connection, i.e. struts near the plates exhibit a stiffened behavior when they are subjected to bending. Because of the limited sample size this effect is more pronounced for the cuboidal samples than for the cylindrical samples. Second, the overall Poisson effect between strut–endings which are clamped in the plates is constrained by the rigid behavior of the plates, also resulting in a pronounced stiffened overall behavior of the cuboidal samples. The large deviations of the stiffnesses of the cuboidal and cylindrical samples with lattice orientation [011] may be explained by the large zone of influence of the top and bottom plates for this lattice orientation. In the case of the [011] cuboidal samples the overall behavior seems to be dominated by the stiffer behavior of the zone of influence of the top and bottom plates.
Since the struts of structures with lattice orientation [001] are mainly subjected to axial

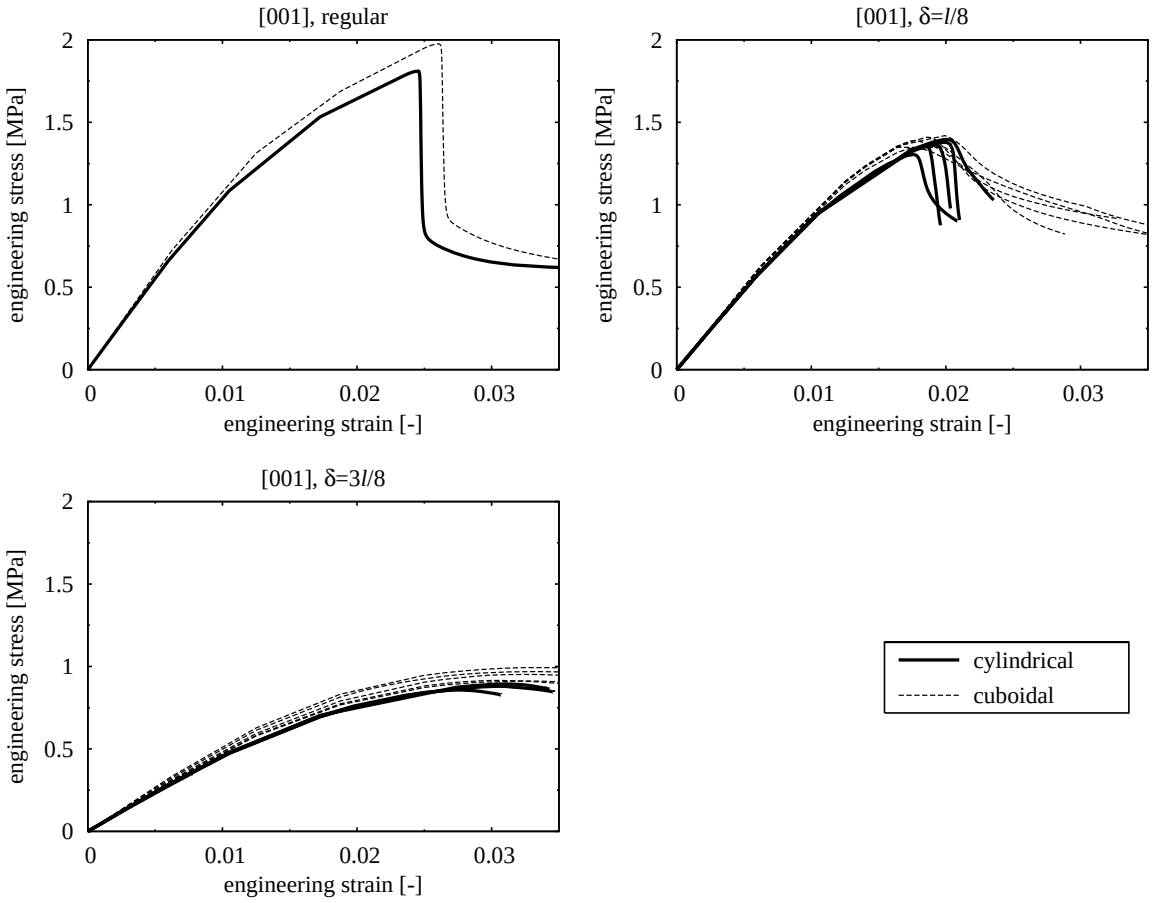

Figure 4.2 Predicted overall stress–strain curves of cylindrical and cuboidal samples with different levels of disorder, δ, for lattice orientation [001] with respect to uniaxial compression.

loading, the influence of the constrained deformation of struts which are connected to the top or bottom plate is insignificant, and the overall behavior of the sample is less affected.

4.3.2 Localization of Deformation

In Section 3.3.2 the localization patterns of cuboidal samples under uniaxial compression are presented. Here, the localization patterns of cylindrical samples with disorder $\delta = l/8$ under uniaxial compression are presented and compared to the corresponding cuboidal samples. Selected localization patterns of the investigated cylindrical structures with disorder $\delta = l/8$ and lattice orientations [001], [021], [011] and [111] are shown in Figure 4.6.

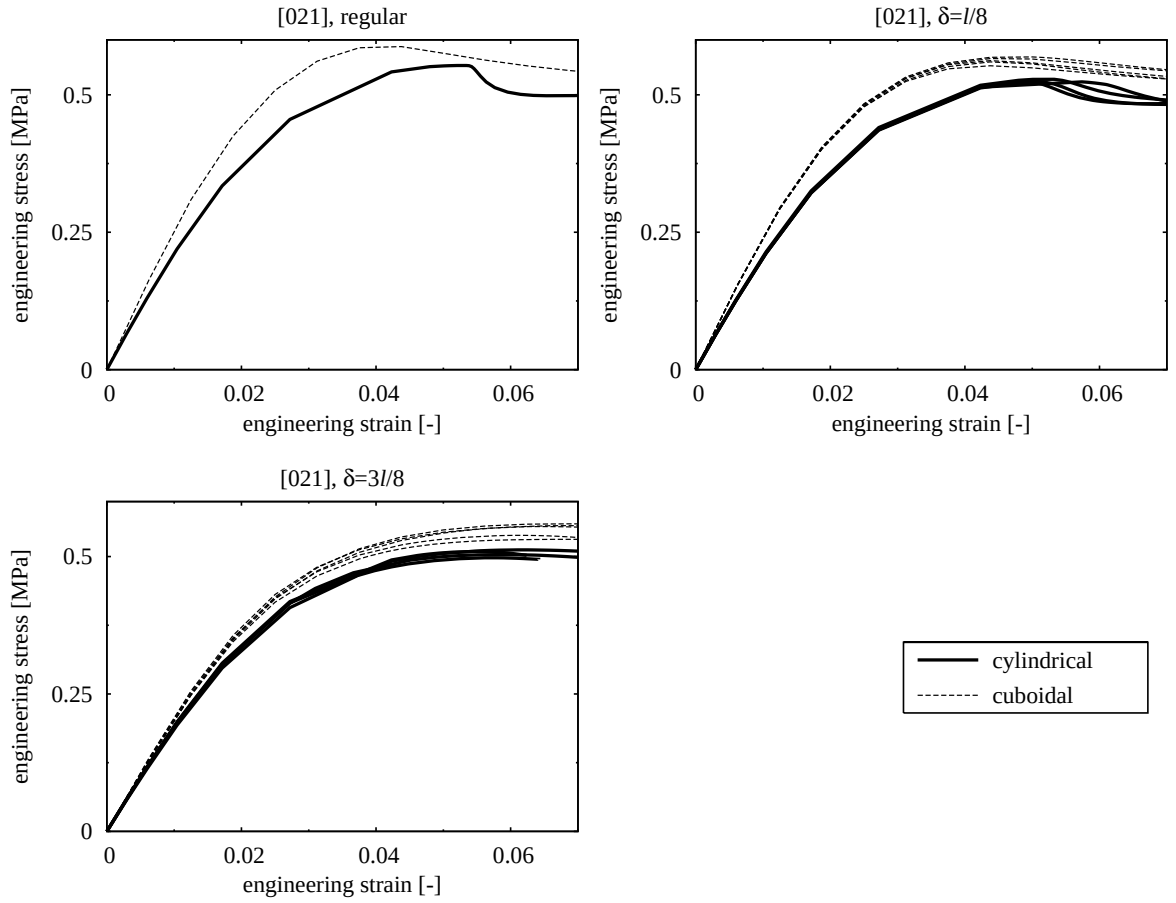

Figure 4.3 Predicted overall stress–strain curves of cylindrical and cuboidal samples with different levels of disorder, δ, for lattice orientation [021] with respect to uniaxial compression.

For the samples with lattice orientations [001] and [021] the shape of the localization patterns of the cylindrical samples coincide with the patterns of the cuboidal samples shown in Section 3.3.2 (Figure 3.5). For both the [001] and the [021] orientations localization takes place in principal structural planes extending one and two layers, respectively. Within the cuboidal samples with lattice orientation [021] localization always starts at the common edge between the plates and the free surfaces. For cylindrical samples with the same lattice orientation localization starts at different positions, but the localization pattern is always the same. Although the cuboidal samples with lattice orientation [021] are able to reproduce the shape of the localization pattern of the cylindrical samples, the position of the localization plane is predetermined due to the small sample size.

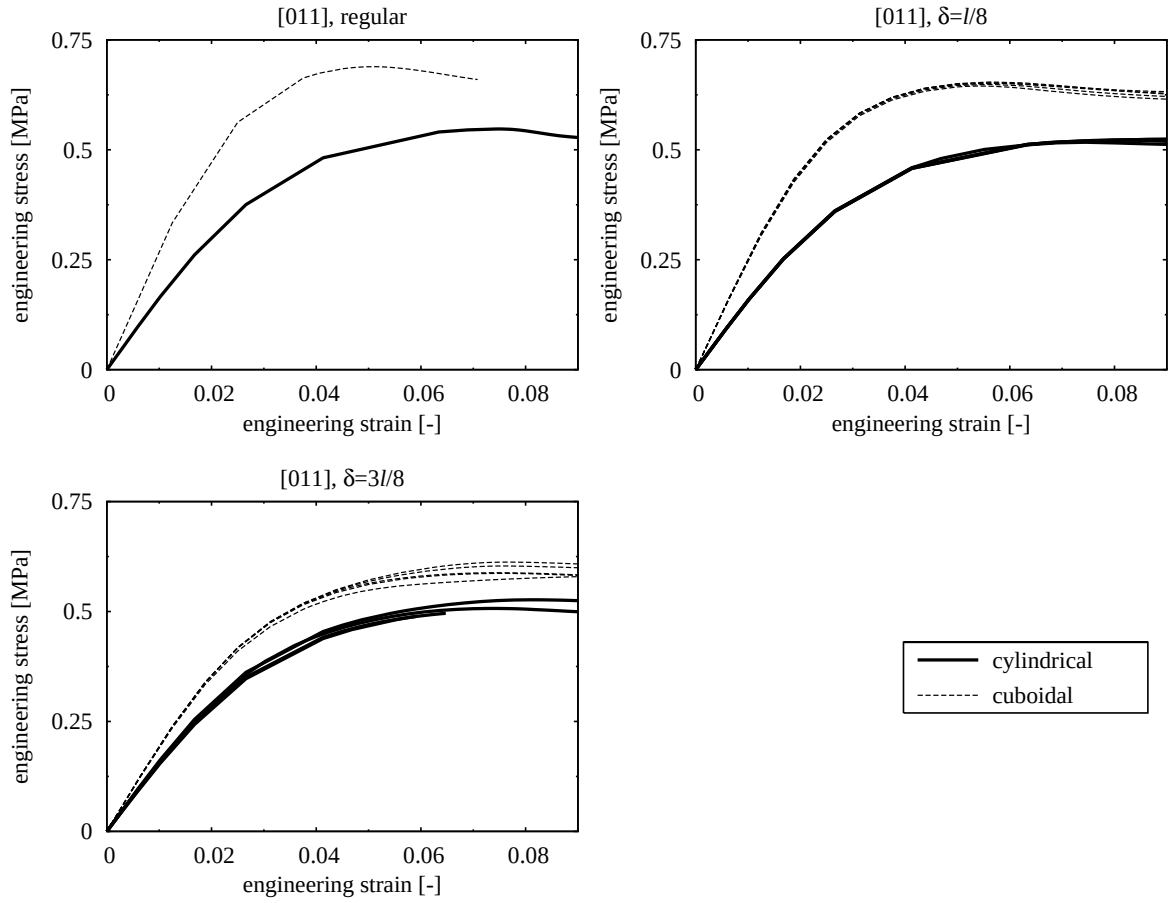

Figure 4.4 Predicted overall stress–strain curves of cylindrical and cuboidal samples with different levels of disorder, δ, for lattice orientation [011] with respect to uniaxial compression.

Similarly, localization of cuboidal samples with lattice orientation [011] always starts at the common edge between the plates and the free surfaces in terms of one collapsing layer of cells, see Section 3.3.2. A slightly different localization behavior is observed for the corresponding cylindrical samples. Two different localization patterns can be seen in Figure 4.6. The first one can be described as a band of three to four adjacent layers of collapsing cells leaving two non-localizing domains. The second observed localization pattern shows a concentration of deformation in the center of the sample surrounded by collapsing cells in the shape of an "X". This shows that the pertinent localization pattern within the cuboidal samples with lattice orientation [011] cannot fully evolve due to the

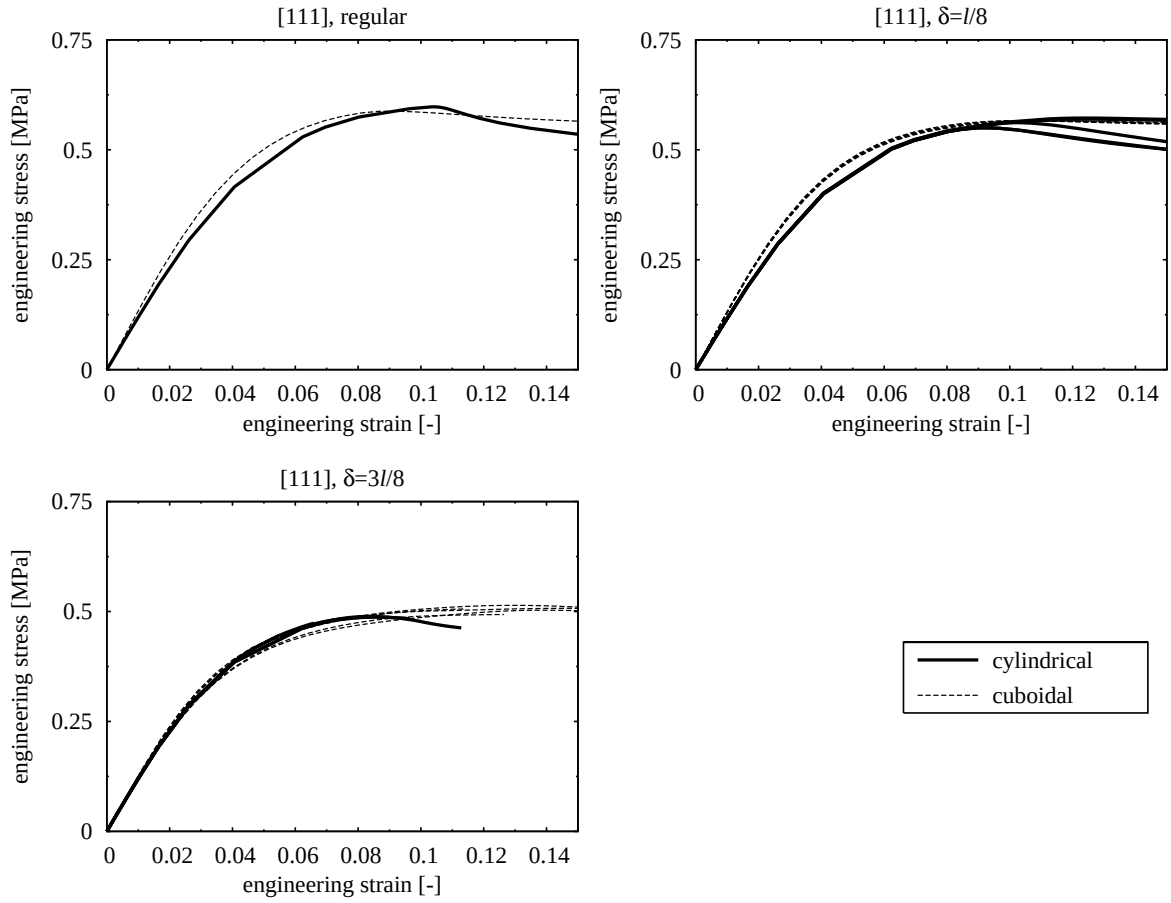

Figure 4.5 Predicted overall stress–strain curves of cylindrical and cuboidal samples with different levels of disorder, δ, for lattice orientation [111] with respect to uniaxial compression.

limited sample size, resulting in a stiffer overall behavior than the cylindrical samples, see also Section 4.3.1.

For some of the simulated cylindrical structures with lattice orientation [111] localization of deformation is observed, see Figure 4.6, whereas no distinct localization of deformation is observed for the cuboidal structures. A development of localization patterns shown by the cylindrical samples within the cuboidal structures is prevented by the limited sample size of the cuboidal samples.

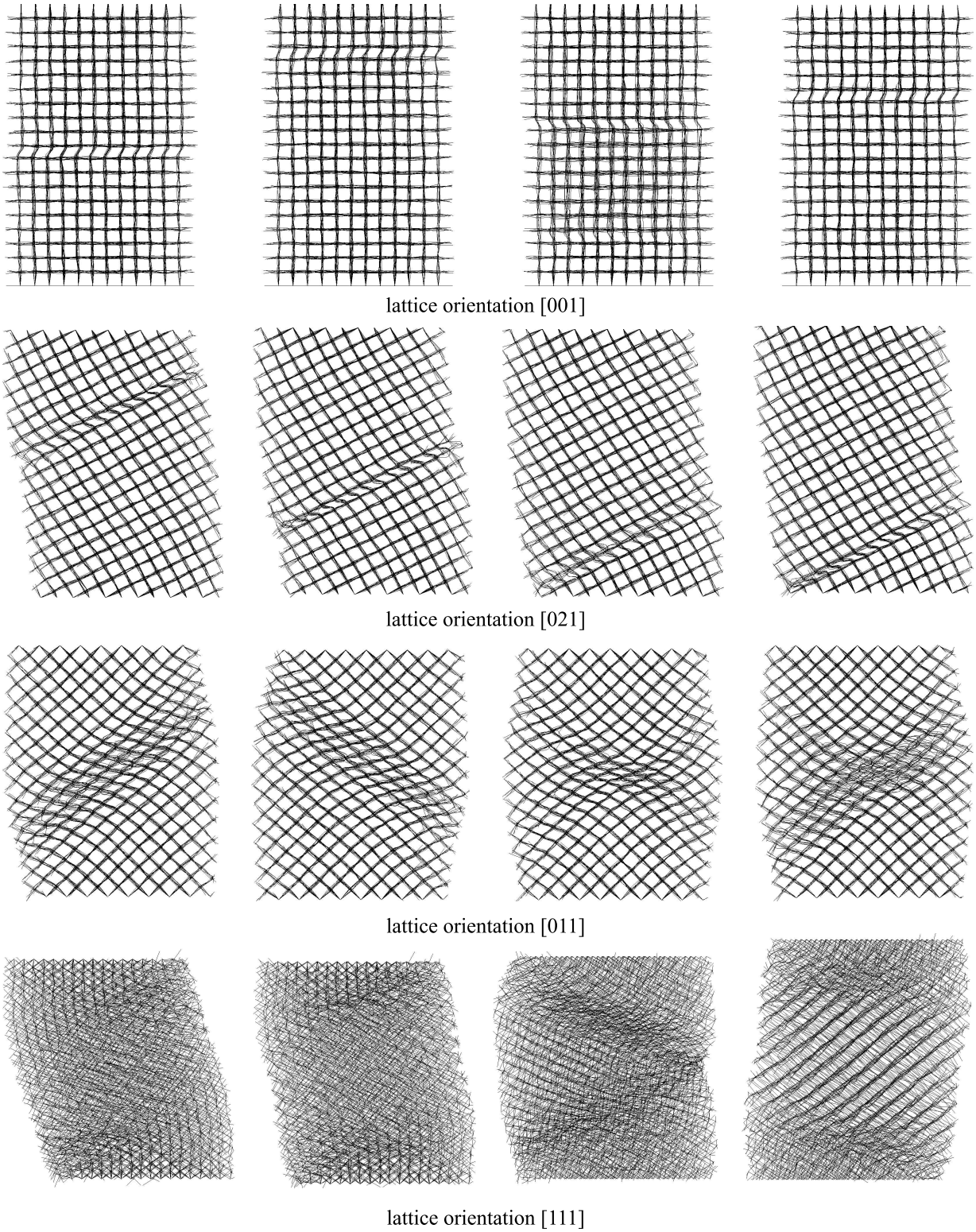

Figure 4.6 Predicted deformation patterns of cylindrical samples with disorder $\delta = l/8$ and lattice orientations [001], [021], [011], and [111].

4.4 Conclusions

The nonlinear mechanical behavior of Simple Cubic structures under uniaxial compression is predicted in terms of overall stress–strain curves and localization patterns of cuboidal and cylindrical samples with different lattice orientations. The stress–strain curves of the cuboidal and cylindrical samples are compared and found to be deviating for the [021] and [011] directions. For these orientations the cuboidal samples are strongly influenced by the rigid top and bottom plates, resulting in a stiffer overall behavior than the cylindrical samples. The stress–strain curves for the [001] and [111] directions are found to be in good agreement.

Similar trends are found regarding the localization of deformation. The localization patterns within cuboidal structures with lattice orientation [011] cannot fully evolve due to the limited sample size. Equivalent localization patterns are found for the structures with [001] and [021] lattice orientations. No unique localization pattern is found for structures with lattice orientation [111].

The results show that adequate care has to be taken regarding the sample shape and size when the nonlinear mechanical behavior of cellular structures is to be determined. For some lattice orientations small samples can predict an overall behavior which rather reflects the sample properties than the properties of the cellular architecture. This can be caused by the dominant influence of the chosen boundary conditions or by a localization pattern which cannot fully evolve.

Chapter 5

Reinforced Simple Cubic Structures

In the previous chapters the elastic anisotropy of several cellular structures with different architectures was analyzed. Based on these findings new cellular architectures with tailored properties are introduced in this chapter.

5.1 Introduction

Several cellular structures with different architectures have been discussed so far within this thesis, see Chapters 2 and 3. The Simple Cubic (SC) and the Kelvin (KV) structures turned out to be the ones with the highest and the lowest anisotropy, respectively, see Section 3.3.1.

The SC structure exhibits high stiffness in the principal directions, but even for small deviations from these directions the structure shows a much more compliant behavior. That means, when loaded in one of the principal directions, SC structures are very sensitive in terms of small changes in load direction and geometric inaccuracy, e.g. caused by the fabrication process, see Section 2.5.5. These facts make them suboptimal for applications in which high stiffness and a certain robustness against varying load directions and structural inaccuracy are required.
By contrast the KV structure exhibits nearly equal, but comparatively low values for the

normalized Young's moduli in all directions. The almost isotropic behavior of the KV structure makes it insensitive to changes in load direction and to structural inaccuracy, see Section 3.3.1, but at a nearly constant overall compliance in all directions which is about six times higher than for a SC structure in the principal directions.

An "optimal" structure in terms of high and constant stiffness at varying load directions and in the presence of structural inaccuracy would be a structure with the high stiffness of a SC structure in the principal directions and the low anisotropy of a KV structure. In this chapter possible cellular architectures are presented to push the mechanical behavior towards high stiffness and low anisotropy at a constant relative density. Based on a SC structure the distribution of the solid phase is changed by shifting bulk material to additional struts. For the introduced structures the elastic anisotropy, the nonlinear behavior under uniaxial compression, and a comparison to experimental results is presented.

5.2 Methods

5.2.1 Structures

As already mentioned, the pronounced anisotropy limits the range of applications of SC structures. A straightforward improvement of their overall behavior is shifting material to additional spatial and face bracings.

In the following, six possible modifications of a SC structure at a constant relative density of 12.5% are introduced in terms of additional spatial and face diagonal struts. The same methodology as introduced in Section 2.2.1 is used to determine the volume of the bulk material. Table 5.1 shows the resulting strut radii.

Body Centered Cubic (BCC) and Face Centered Cubic (FCC)

One possible improvement to reduce the anisotropy of a SC structure has already been shown by introducing the Body Centered Cubic (BCC) structure, see Chapters 2 and 3. Additional struts have been added in the spatial diagonal directions, see Figure 5.1. An-

other straightforward approach would be the adding of diagonal struts in the side faces of a SC structure, resulting in a Face Centered Cubic (FCC) structure, see Figure 5.1.

Reinforced Simple Cubic Structures

Due to the rearrangement of bulk material from the struts in principal directions to the additional struts at a constant relative density all struts become thinner, e.g. for the BCC and FCC structures the strut radii are only about half the size as for the SC structure, see Table 5.1. On account of this a class of structures is introduced subsequently for which the decrease of the strut radii due to the shifting of bulk material is less pronounced.

An alternative modification with fewer additional –and thus thicker– struts, which will be referred to as Reinforced Simple Cubic 1 (RSC1) in the following, consists of a SC structure in which in every second principal plane face diagonals in every second side face in the appropriate principal directions are added, see Figure 5.1. This results in a checkerboard pattern in every second principal plane.

This modification is inspired by the design of the skeleton of the deep-sea sponge *Euplectella* sp. [Aizenberg et al., 2005], which fulfills the necessary connectivity in each vertex to achieve shear stability for a two–dimensional grid without overconstraining [Deshpande et al., 2001].

Following the design of the RSC1 structure, the Reinforced Simple Cubic 2 (RSC2) structure is generated by adding face diagonals in every second side face in the appropriate principal directions, but in every principal plane, see Figure 5.1. The additional struts result in smaller strut radii than for the RSC1 structure, see Table 5.1.

The next modification, which will be referred to as Reinforced Simple Cubic 3 (RSC3) in the following, is described as a SC structure superimposed by a BCC structure where the sidelength of the BCC base cell is twice the sidelength of the SC base cell, see Figure 5.1, i.e. spatial diagonals are added in every second cube in principal directions.

Table 5.1 Strut radii of the investigated structures with a relative density of 12.5% determined by the volume approximation described in Section 2.2.1.

Structure	Strutradius
SC	0.515
FCC	0.250
BCC	0.261
RSC1	0.414
RSC2	0.336
RSC3	0.420
RSC4	0.343

As the last modification presented within this study the Reinforced Simple Cubic 4 (RSC4) structure is introduced. It is created by superimposing a RSC1 structure with a RSC3 structure, see Figure 5.1.

5.2.2 Numerical Models

For all numerical investigations the beam element modeling technique including adaption of the stiffness and the material distribution in the vicinity of the vertices is employed, see Section 2.2.1.

For the evaluation of the elastic anisotropy periodic unit cell models of single base cells, see Figure 5.1, are employed and the required number of independent load cases is solved for each structure, see Section 2.3.1. From these responses the entire elastic tensors are assembled and the Young's moduli in all spatial directions are extracted by rotational transformations of the tensors. Note that due to the modifications the side lengths of the periodic part of the RSC structures become two times larger than the size of the periodic part of the SC, FCC, and BCC structures. Consequently, larger unit cell models must be used, see Figure 5.1.

Finite sample models, see Section 2.3.2, are used to predict the nonlinear stress–strain curves of the RSC structures with different lattice orientations with respect to uniaxial

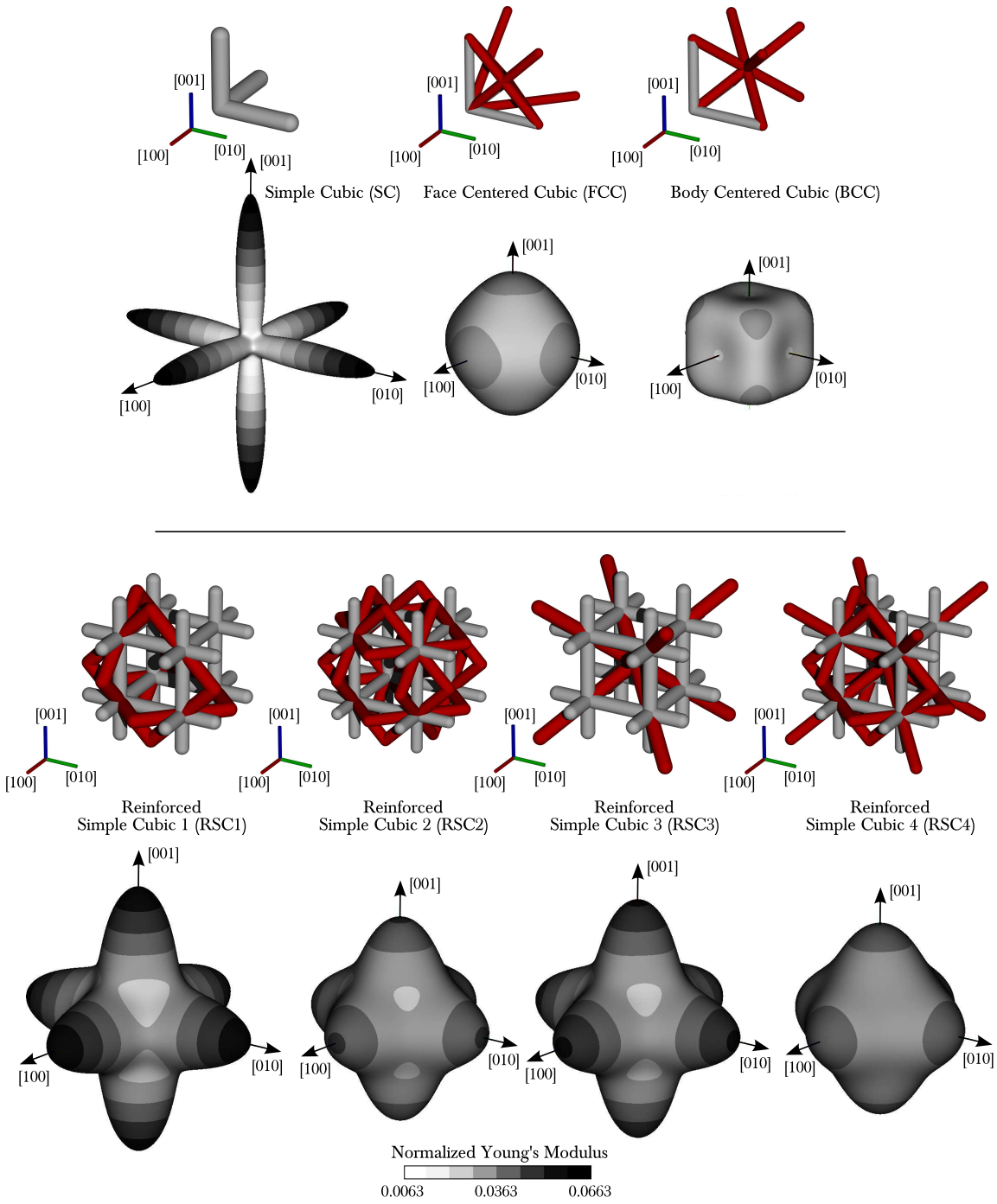

Figure 5.1 Base cells of SC, FCC, BCC, RSC1, RSC2, RSC3, and RSC4 structures with a relative density of 12.5% (upper rows) and their predicted normalized Young's moduli in all spatial directions (below). Note that the dimensions of the RSC basecells are twice the dimensions of the SC, FCC, and BCC basecells.

compression. Note that the SC samples and the RSC samples have equal overall dimensions, but the periodic cell of the RSC structures is larger and therefore the RSC samples consist of only 4×4×4 periodic base cells.

5.2.3 Rapid Prototyping and Experiments

RSC1 structures with lattice orientations [001], [021], [011], and [111] are fabricated by Digital Light Processing, see Section 2.4 and Figure 5.2, and tested by uniaxial compression[1]. The same experimental setup as described in Section 2.4 is used. For each lattice orientation five samples are built and tested. The behavior of the bulk material corresponds to Figure 3.1.

5.3 Results and Discussion

Below, the anisotropy of the linear elastic stiffness for the structures introduced above is evaluated and discussed. Furthermore, the nonlinear stress–strain curves for RSC1, RSC2, RSC3, and RSC4 are predicted and compared to the SC structure. Experimental results of a RSC1 structure obtained from uniaxial compression tests of samples fabricated by Rapid Protoyping are compared to the simulation results.

5.3.1 Elastic Anisotropy

The elastic anisotropy of the introduced modified SC structures is discussed in the following. In Figure 5.1 the Young's moduli, E^*, (normalized by the Young's modulus of the bulk material, E_s) for the SC, FCC, BCC, RSC1, RSC2, RSC3, and RSC4 structures are shown for each direction. Note that the scalings of the three–dimensional representations of the Young's moduli are equal. In addition, Figure 5.3 shows the normalized Young's moduli of the introduced structures and the KV structure for directions within the (100)

[1]Fabrication and testing were performed in cooperation with Alexander Woesz during the author's stay at the Max Planck Institute of Colloids and Interfaces, Potsdam, Germany.

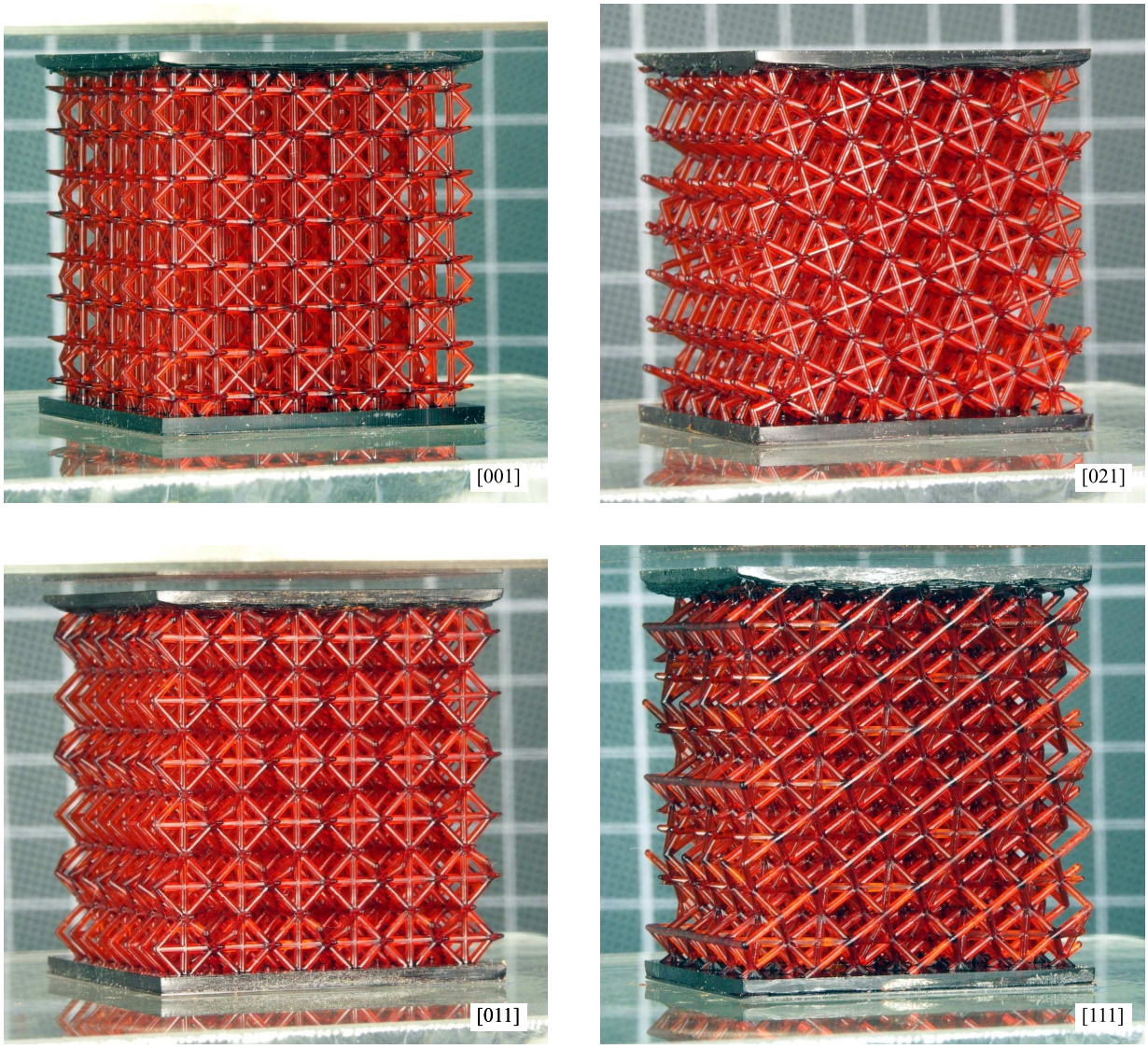

Figure 5.2 RSC1 test samples with a relative density of 12.5% and lattice orientations [001], [021], [011], and [111] fabricated by Digital Light Processing. Base cell length is 4 mm.

and $(1\bar{1}0)$ planes by means of polar plots. A comparison of the normalized Young's moduli in selected directions by means of absolute values and percentages is shown in Table 5.2. Since all structures show cubic material symmetry, the extremal stiffness values appear in the [001] and the [111] directions [Nye, 1985]. On account of this the ratio of the maximum Young's modulus and the minimum Youngs's modulus, $E^*_{\max}/E^*_{\min}$, is introduced as a simple measure for anisotropy, see Table 5.2.

Out of the modified SC structures the FCC structure shows the lowest anisotropy. The ratio $E^*_{\max}/E^*_{\min}$ is close to that of the KV structure, but, the FCC structure shows an about 53% more compliant overall behavior in principal directions than the SC structure. The additional face diagonals result in a less pronounced anisotropy which is paid for by a large decrease of the overall stiffness in the principal directions.
The BCC structure is the stiffest structure in the [111] direction, which is the consequence of the thru struts in this direction. For most directions except the [111] direction the BCC structure shows the most compliant overall behavior. Neither the FCC nor the BCC structure shows a satisfactory overall behavior concerning the desired high stiffness at low elastic anisotropy.

The RSC1 structure shows the lowest degradation of stiffness in the principal directions caused by the redistribution of the bulk material. It is only 12% more compliant in [001] direction than the SC structure and exhibits its minimal stiffness in [111] direction, resulting in $E^*_{\max}/E^*_{\min} = 2.29$, which is about five times less than for the SC structure.

The additional struts of the RSC2 structure increase the stiffness around the [111] and [011] directions slightly, but compared to the RSC1 structure the stiffness in principal directions is decreased markedly, which results in $E^*_{\max}/E^*_{\min} = 1.59$. This makes the RSC2 structure a rather inefficient structure in terms of material distribution, maximum stiffness, and elastic anisotropy.

The RSC3 structure exhibits about the same stiffness in the [021], [011] and [111] directions as the RSC2 structure, but it is about 17% stiffer in the principal directions than the RSC2 structure. Hence, in terms of the desired improvements the RSC3 structure would be a better choice than the RSC2 structure.

The RSC4 structure has about the same stiffness in [111] direction as the BCC structure. Among the RSC structures the RSC4 structure is the one with the highest Young's modulus in the [111] direction and exhibits the lowest Young's modulus in the principal directions, resulting in $E^*_{\max}/E^*_{\min} = 1.40$.

Concerning robustness against varying load directions around the principal directions and structural inaccuracy the RSC1 structure proves to be a robust replacement for a SC

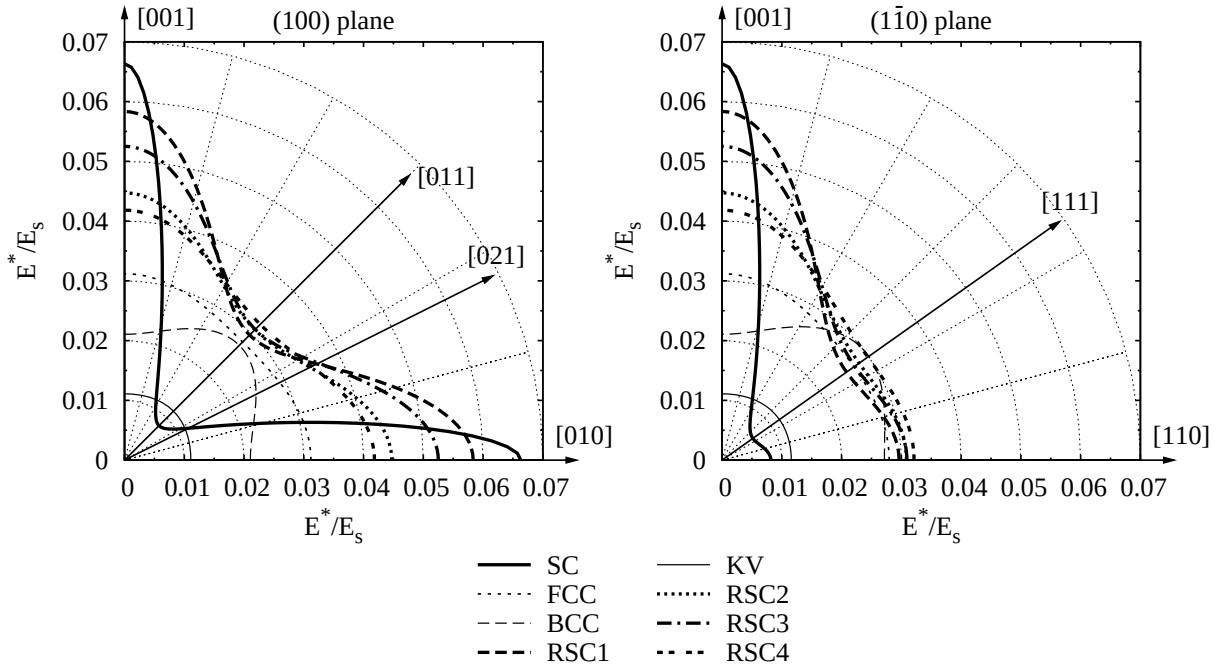

Figure 5.3 Comparison of the normalized Young's moduli in the (100) and $(1\bar{1}0)$ planes for SC, KV, FCC, BCC, RSC1, RSC2, RSC3, and RSC4 structures with a relative density of 12.5%.

structure, since the stiffness in principal directions is only 12% smaller than for the SC structure and the elastic anisotropy is decreased by a factor of about five. For deviations not exceeding 25° from the principal directions the RSC1 structure turns out to be the best choice in terms of high elastic stiffness.

5.3.2 Nonlinear Behavior

In Figure 5.4 the predicted overall stress–strain curves of regular SC, RSC1, RSC2, RSC3 and RSC4 finite structures for lattice orientations [001], [021], [011], and [111] with respect to uniaxial compression are shown.

In the case of the investigated structures with lattice orientation [001], see Figure 5.4 (top left), the load is mainly carried by the continuous struts in load direction. On this account the overall mechanical behavior in this direction is dominated by these struts and the SC structure exhibits the highest peak stress because of its large strut radius. Since the strut

Table 5.2 Comparison of the normalized Young's moduli of the investigated structures for selected directions. Percentages refer to the Simple Cubic structure.

	$E^*/E_\mathrm{s} \times 10^{-2}$				$E^*_\mathrm{max}/E^*_\mathrm{min}$
	[001]	[021]	[011]	[111]	
SC	6.6320	1.1921	0.8157	0.6310	10.51
KV	1.1090	1.1400	1.1580	1.1740	1.06
	-83.28%	-4.37%	+41.96%	+86.06%	
FCC	3.1194	2.9043	2.7958	2.7024	1.15
	-52.97%	+143.63%	+242.74%	+328.29%	
BCC	2.1062	2.4599	2.7164	3.0067	1.43
	-68.24%	+106.35%	+233.00%	+376.52%	
RSC1	5.8341	3.5981	2.9609	2.5503	2.29
	-12.03%	+201.83%	+262.97%	+304.19%	
RSC2	4.4730	3.4718	3.0857	2.8086	1.59
	-32.55%	+191.24%	+278.28%	+345.12%	
RSC3	5.2509	3.6301	3.0931	2.7205	1.93
	-20.83%	+204.52%	+279.18%	+331.15%	
RSC4	4.1826	3.5043	3.2123	2.9864	1.40
	-36.93%	+193.97%	+293.79%	+373.31%	

radii of the modified structures are decreased by the reallocation of the bulk material, the peak stresses of all RSC structures are lower than for the SC structure.
The RSC1 and RSC3 structures exhibit roughly the same strut radii and show higher peak stresses than the RSC2 and RSC4 structures, which also exhibit about the same strut radii. Nevertheless, the overall behavior is not only governed by the thru struts. The orientations of the additional diagonals also have some effect, since the RSC3 structure has a slightly larger strut radius than the RSC1 structure, but is less stiff. The same correlation is observed for the RSC2 and RSC4 structures. Exceeding the peak stress of a SC structure results in a sudden drop in the stress–strain curve, i.e. in a catastrophic failure of the structure. For all RSC structures the maximum stress occurs at higher overall strains and the drop of the stress–strain curves after the maximum stress has been reached is far less steep than for the SC structure, i.e. the RSC structures show an improved behavior after the maximum stress has been reached.

Out of the modified structures with lattice orientation [021] the ones with additional diagonal struts, namely the RSC3 and RSC4 structures, show the highest peak stresses, see Figure 5.4 (top right). The RSC1 and RSC2 structures show a very similar overall mechanical behavior for the [021] lattice orientation. All RSC structures with lattice orientation [021] show a markedly improved overall behavior in terms of the maximum peak stress compared to the SC structure.

Similarly to the [021] lattice orientation, out of the structures with lattice orientation [011] the RSC3 and RSC4 structures exhibit the highest peak stresses, see Figure 5.4 (bottom left). The predicted curves for RSC1 and RSC2 are nearly equal. Again, compared to the SC structure, all RSC structures show a markedly improved overall behavior in terms of the maximum peak stress.

The RSC2 structures exhibits the highest peak stress out of the RSC structures with lattice orientation [111], see Figure 5.4 (bottom right). Interestingly, the RSC3 structure, which has struts oriented in the [111] direction, shows a smaller peak stress than all other structures. The RSC1 and RSC3 structures show a similar behavior.

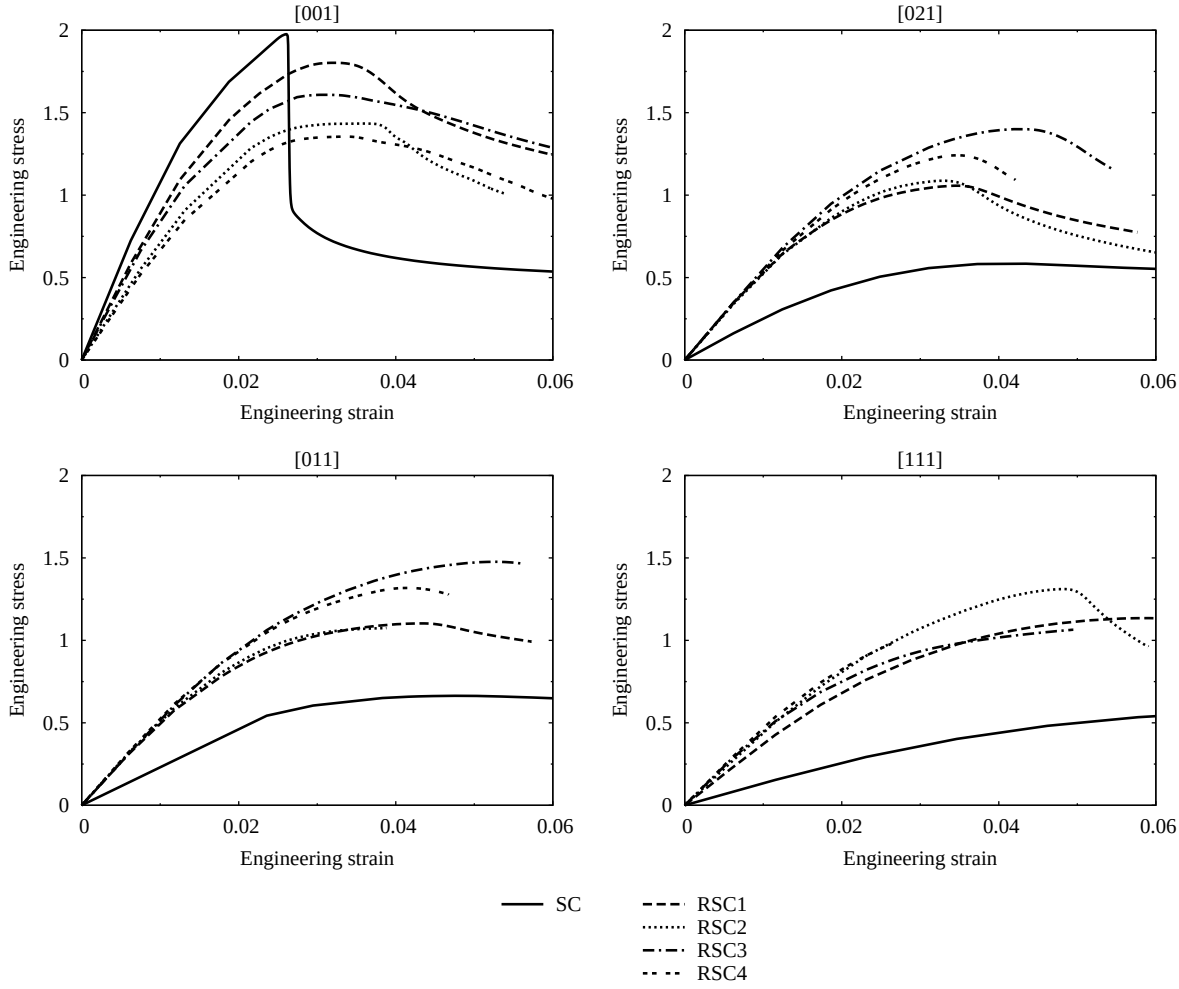

Figure 5.4 Predicted overall stress–strain curves of regular SC, RSC1, RSC2, RSC3 and RSC4 finite structures for lattice orientations [001], [021], [011], and [111] with respect to uniaxial compression.

5.3.3 Experimental Results

In Figure 5.5 the numerically predicted and experimentally obtained overall stress–strain curves of RSC1 structures with lattice orientations [001], [021], [011], and [111] are shown. For each lattice orientation the results of five tested samples are presented.

For lattice orientations [001], [021], and [011] some scatter in the experimental results is observed, whereas the curves for the [111] lattice orientation exhibit smaller deviations. This can be explained by the different stiffness gradients at the investigated directions.

From Figure 5.3 it can be seen that for the directions [001], [021], and [011] the gradient of the Young's modulus is higher than for the [111] direction. The latter case makes the structure less sensitive to changes in load direction and structural inaccuracy under uniaxial compression in the [111] direction. Both deviations from the theoretical load direction and structural inaccuracy cannot be avoided during experiments.

In all cases the simulations predict a stiffer overall behavior than shown by the tested samples. This may be due to the beam modeling approach, which tends to overestimate the overall stiffness of the structures, see Section 2.5.3, and by assuming a rigid behavior of the top and bottom plates. The large deviation in the [111] case cannot be fully explained, it is assumed that for this strongly bending dominated direction the chosen beam element approach predicts a too stiff overall behavior. Except for the [001] direction the peak stress predicted by the simulations is lower than predicted by the experiments.

5.4 Conclusions

In this chapter several modifications of a Simple Cubic (SC) structure are presented. The goal is to achieve an improved overall mechanical behavior in terms of robustness against varying load directions and structural inaccuracy at a constant relative density and high stiffness. The elastic anisotropy and the nonlinear behavior under uniaxial compression is predicted by Finite Element simulations. The predicted nonlinear behavior is compared to results obtained from uniaxial compression tests of samples fabricated by Digital Light Processing.

The FCC and BCC structures with their face and spatial bracings, respectively, turned out to be modifications with a low anisotropy but a very compliant behavior. Hence, the desired behavior is not fully met by the FCC and BCC structures.

In terms of the desired robustness against varying load directions and structural inaccuracy at high overall stiffness in principal directions, out of the investigated structures the RSC1 structure turns out to be the best suitable modification. The elastic anisotropy has been

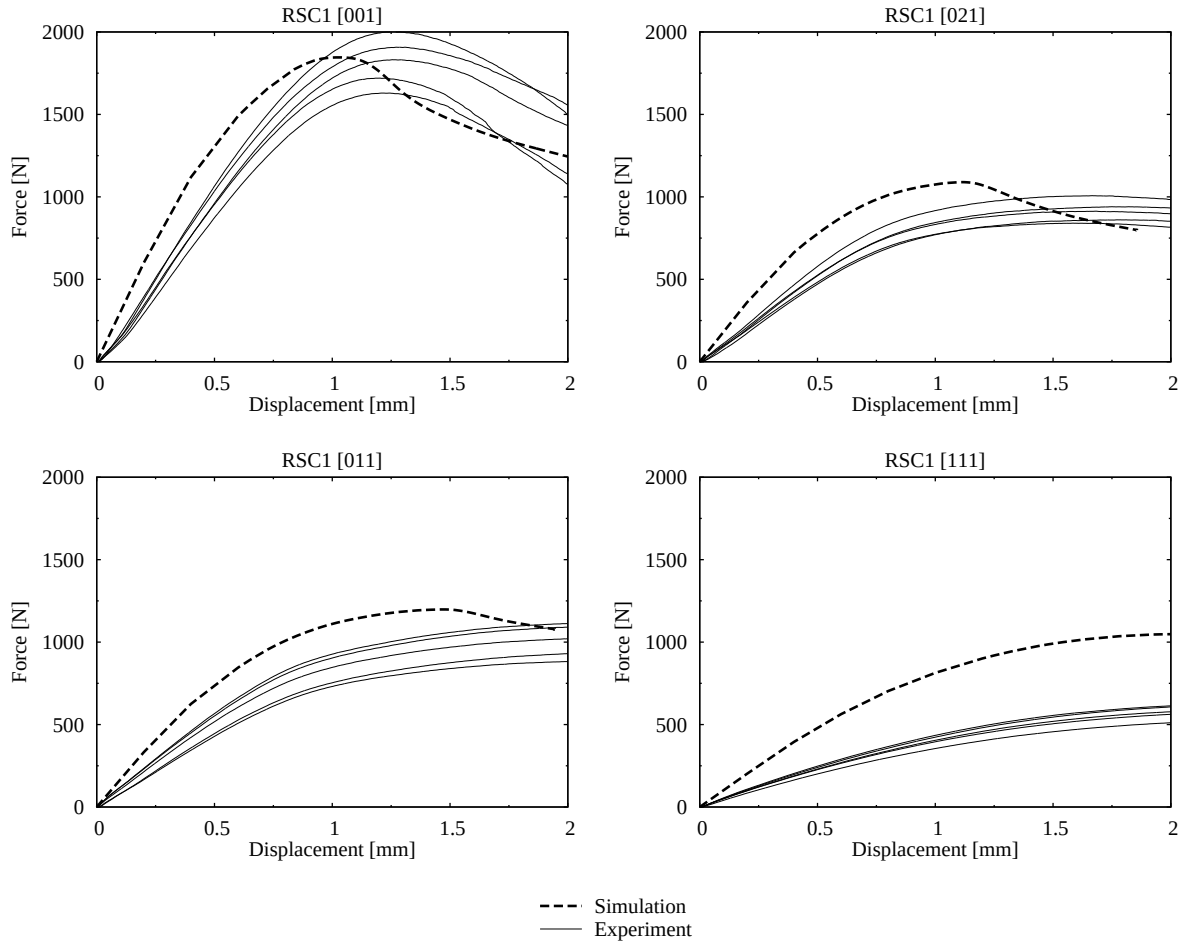

Figure 5.5 Predicted overall stress–strain curves of RSC1 structures with lattice orientations [001], [021], [011], and [111] in comparison with experimental results with respect to uniaxial compression.

reduced by a factor of about five and the Young's moduli in the principal directions are only 12% less than for the SC structure.

Regarding the nonlinear behavior under uniaxial compression all RSC structures exhibit a markedly increased peak stress for lattice orientations [021], [011], and [111] compared to the SC structure. For the [001] lattice orientation the peak stress of all RSC structures is lower than for the SC structure, but the drops after the peak stress of the stress–strain curves of the RSC structures are less steep, so that they can carry higher loads after exceeding the peak load. The directional dependence of the strength is markedly reduced by the RSC1 structure.

Experimental results obtained from RSC1 structures with several lattice orientations built by Digital Light Processing are compared to the results predicted by the Finite Element simulations. The simulations predict a stiffer overall behavior and, except for one direction, a higher peak load, but the the qualitative and quantitative behaviors agree very well.

Chapter 6

Influence of Defects

Within this chapter the regular and disordered cylindrical Simple Cubic structures from Chapter 4 are taken and a systematic computational study on the interaction of defects and structural disorder is performed.

6.1 Introduction

Regular structures have proven to be useful theoretical tools for understanding some of the key aspects of the mechanical behavior of cellular solids, see Chapters 2 to 5. In contrast to an idealized structure, most cellular materials in nature and engineering applications exhibit imperfections and inhomogeneities in their microstructure. The influence of several levels of structural disorder is already addressed in Chapters 3 and 4. Another source of inhomogeneities within an open cell material are defects which may occur during the fabrication process, while in service, and due to an age–related remodeling process, e.g. in bone [Mosekilde, 2000; Moore and Gibson, 2001, 2002; Currey, 2003]. The understanding of the effect of defects and their interaction with structural disorder becomes important for the design of new cellular materials which are less sensitive to defects and for an assessment of the implication of the age–related remodeling process in bone.

Several investigations regarding the influence of defects on the mechanical behavior of cellular solids have been reported. Silva et al. [1995]; Silva and Gibson [1997a] investigate the effects of non-periodic microstructure and defects on the compressive behavior of two–dimensional cellular solids by means of Finite Element models. Periodic, hexagonal honeycombs are compared to non-periodic Voronoi honeycombs. Defects are introduced by removing cell walls at random locations. The structures are compared in terms of elastic moduli, plastic collapse strength, and localization of deformation. In [Silva and Gibson, 1997b] they extend their numerical models to modeling of changes in the microstructure of vertebral trabecular bone. The stress-strain behavior, failure mode, and strain distribution are predicted for healthy bone and aged bone. Guo and Gibson [1999] employ Finite Element models to study the mechanical behavior of intact and damaged honeycombs. The effect of single, isolated defects of varying sizes and the effect of the distance between two defects on the elastic and plastic behavior are analyzed. The defect sensitivity of a three-dimensional truss-like structure is investigated by Wallach and Gibson [2001]. The influence of randomly removing struts on stiffness and compressive strength is calculated numerically. Andrews and Gibson [2001] perform Finite Element simulations of two–dimensional cellular structures with defects to study the influence of defect size and cell size on the tensile strength of cellular structures. The effects of holes and rigid inclusions on the elastic modulus and yield strength of regular honeycombs under biaxial loading by means of Finite Element studies are investigated by Chen et al. [2001]. In [Albuquerque et al., 1999] an experimental study of in-plane deformation in compression of honeycombs with missing cell walls is presented.

Within this chapter the influence of defects with varying characteristics on the linear elastic and nonlinear behavior of three–dimensional open cell structures is investigated. Simple Cubic structures with different lattice orientations are used to analyze the differences in the mechanical response of regular and disordered structures when parts of the structure are removed.

6.2 Methods

6.2.1 Investigated Structures

Cylindrical samples as introduced in Chapter 4 are used for the investigations presented in this chapter. Simple Cubic (SC) structures with lattice orientations [001], [021], [011], and [111] are generated by arranging appropriately rotated base cells. All investigations are based on structures with a relative density of 12.5%. The diameter of the cylindrical samples is chosen to be 13 base cells, i.e. 52 mm, their height is about 20 base cells, i.e. approximately 80 mm, see Figure 4.1.

Defects

Three different classes of defects are introduced by removing a constant number of struts from the structures, i.e. for all types of defects the same amount of bulk material is removed from the samples and, therefore, their relative density is decreased. The number of struts to be removed is chosen to be 108. This corresponds to 1.87% of the total number of struts within a structure, i.e. due to the defects the relative density of the structures changes to 12.25%.

For the first class of defects 108 single struts are randomly removed, see Figure 6.1 (left). As a second approach 18 vertices are removed from the structures, i.e. 18 vertices are randomly selected and the six struts connected to each of them are removed, see Figure 6.1 (middle). The third class of defects is generated by removing three clusters of struts consisting of 36 struts each. Each cluster is generated by removing the struts which are connected to the vertices of a randomly selected cube, see Figure 6.1 (right).

All defects are randomly chosen obeying the condition that neighboring defects cannot share a vertex, i.e. defects are forced to keep a certain distance to adjacent defects. To avoid pronounced interactions between the defects and the surfaces of the sample the defects are limited to a predetermined internal domain. This domain is defined by a concentric cylinder with radius 22 mm and height 56 mm, which prohibits defects close to

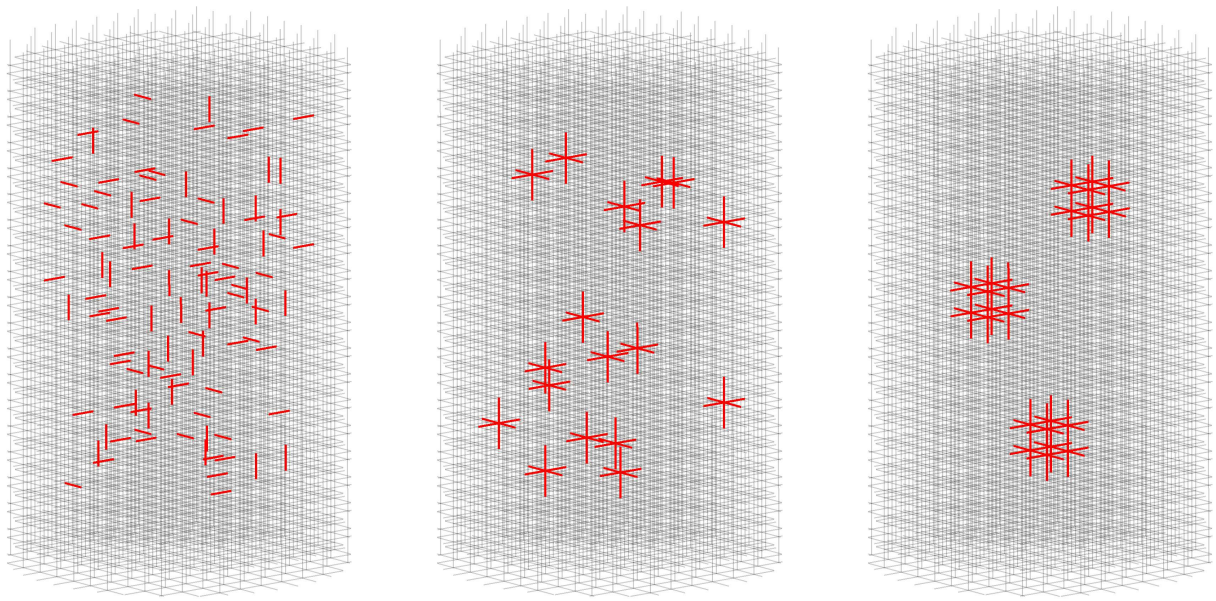

Figure 6.1 Three different classes of defects shown by means of a Simple Cubic structure with lattice orientation [001]; each class of defects consists of 108 removed struts. The struts to be removed are emphasized.

the top and bottom surface and within an outer "shell" with the thickness of the baselength of two base cells.

For each class of defects and each lattice orientation five sets of defects are generated. In the case of disordered structures without defects also five models are generated for each level of disorder.

Structural Disorder

Each class of defects is applied to regular and disordered structures. The same type of disorder as described in Section 3.2.2 is employed. For each lattice orientation and each type of defect the same particular five sets of defects are applied to the structures, i.e. the same struts are removed from the regular and the respective disordered structures. Disorder of levels $\delta = l/8$ and $\delta = 3l/8$ is investigated. In the case of the defects applied to the disordered structures, each structure exhibits a different structural disorder.

6.2.2 Finite Element Models

Beam element based models with adaptation of the stiffness and the material distribution in the vicinity of the vertices, see Section 2.2.1, are used for the subsequent investigations. The boundary conditions are chosen as described in Section 2.3.2. The bulk material behavior corresponds to the crosslinked photopolymer introduced in Section 3.2.2. Large deformations are considered within the nonlinear FEM analyses.

6.3 Results and Discussion

6.3.1 Overall Uniaxial Linear Stiffness

First, the overall linear stiffness of the various samples is discussed. For this purpose the Young's moduli in axial direction of the cylinders, $\bar{E}_{\mathrm{cyl}}$, are determined from the stress response of the structure to a small strain in loading direction. This small strain corresponds to the first increment in the nonlinear FEM analyses and amounts 0.003 for all samples.

Figure 6.2 shows a comparison of the average Young's moduli, $\bar{E}_{\mathrm{cyl}}$, of SC structures with lattice orientations [001], [021], [011], and [111] and different defects at various levels of disorder. In addition the corresponding values and a comparison per cent to the particular samples without defects is given in Table 6.1. In each case the average Young's modulus and its standard deviation, s, are determined from five simulated structures.

For all investigated cases the defects result in a decrease of the axial stiffness. Depending on the lattice orientation the level of the decrease varies. The most distinctive decrease of stiffness is observed for structures with lattice orientation [001] with missing single struts (regular and disordered) and for structures with lattice orientation [021] and [011], respectively, with missing single struts and a disorder of level $\delta = 3l/8$, see Table 6.1. It can be seen that a removal of 1.87% bulk material results in a reduction of stiffness of about 2–7%.

Irrespective of the level of disorder and the lattice orientation the missing single struts always result in the strongest decrease of the stiffness in axial direction. For all cases of structures with lattice orientation [011] the missing vertices result in the smallest decrease of stiffness, whereas for structures with lattice orientations [001], [021], and [111] no consistent trend regarding the class of defect and the stiffness is observed, see Figure 6.2 and Table 6.1.

Note that with the exception of structures with lattice orientation [111] structural disorder always yields a decrease of stiffness. For the lattice orientation [111] the structural disorder of level $\delta = 3l/8$ results in an increase of stiffness, which reflects the findings obtained from the unit cell models in Section 3.3.1, where for increasing disorder a decrease of stiffness in the [001], [021], and [011] directions is predicted, and in the [111] direction for $\delta = 3l/8$ an increase of stiffness is observed.

6.3.2 Nonlinear Overall Behavior

In Figures 6.3 to 6.6 the predicted overall stress–strain curves of SC cylindrical samples with lattice orientations [001], [021], [011], and [111] subjected to compression in axial direction are shown. Samples with three different classes of defects and varying levels of disorder (thin lines) are compared to disordered and regular samples without defects (bold lines). The results for the disordered structures without defects correspond to the results in Chapter 4, Figure 4.2 to 4.5. For the sake of clarity only the enveloping curves from Figures 4.2 to 4.5 are copied to Figures 6.3 to 6.6. Three to five structures are analyzed for each class of defects, lattice orientation, and level of structural disorder.

The differences in the nonlinear responses of the various structures are discussed in terms of the peak stresses and the strains at which they occur, in the following denoted as "peak strains". The average peak stresses, the corresponding average peak strains, and the standard deviations (indicated by the error bars) of respectively three to five structures are shown in Figures 6.7 to 6.10 and Tables 6.2 and 6.3.
Some simulations terminate due to numerical difficulties prior to reaching the peak load, i.e. a peak stress cannot be detected definitely. Proven by experience, such numerical

Table 6.1 Average Young's moduli in axial direction, $\bar{E}_{\mathrm{cyl}}$, of cylindrical SC structures with lattice orientations [001], [021], [011], and [111] and different defects at various levels of structural disorder, δ. In each case the average Young's modulus and its standard deviation, s, are determined from five simulated structures.

		regular		$\delta = l/8$		$\delta = 3l/8$	
		$\bar{E}_{\mathrm{cyl}}$ [MPa]	$s \times 10^{-1}$ [MPa]	$\bar{E}_{\mathrm{cyl}}$ [MPa]	$s \times 10^{-1}$ [MPa]	$\bar{E}_{\mathrm{cyl}}$ [MPa]	$s \times 10^{-1}$ [MPa]
[001]	no defects	11.117	-	9.697	1.846	4.787	5.319
	missing struts	10.319	4.958	9.034	7.531	4.494	3.825
		-7.18%		-6.83%		-6.11%	
	missing vertices	10.677	1.129	9.323	1.857	4.583	4.062
		-3.96%		-3.86%		-4.26%	
	missing clusters	10.609	11.837	9.298	3.705	4.625	6.389
		-4.57%		-4.11%		-3.37%	
[021]	no defects	2.219	-	2.145	1.085	1.971	2.647
	missing struts	2.133	1.180	2.053	1.034	1.848	3.526
		-3.86%		-4.27%		-6.22%	
	missing vertices	2.151	0.237	2.070	0.962	1.914	3.483
		-3.06%		-3.48%		-2.86%	
	missing clusters	2.148	0.171	2.075	0.678	1.912	3.278
		-3.18%		-3.24%		-2.98%	
[011]	no defects	1.598	-	1.554	1.726	1.550	3.359
	missing struts	1.537	0.204	1.485	0.385	1.442	2.200
		-3.83%		-4.44%		-6.99%	
	missing vertices	1.548	0.371	1.499	0.649	1.470	2.160
		-3.12%		-3.57%		-5.18%	
	missing clusters	1.542	0.126	1.492	0.631	1.465	1.973
		-3.47%		-3.99%		-5.48%	
[111]	no defects	1.142	-	1.116	0.301	1.168	1.403
	missing struts	1.101	0.074	1.071	0.329	1.121	0.528
		-3.59%		-4.02%		-3.98%	
	missing vertices	1.109	0.042	1.083	0.136	1.130	0.427
		-2.90%		-2.98%		-3.22%	
	missing clusters	1.109	0.178	1.081	0.328	1.140	2.795
		-2.87%		-3.17%		-2.36%	

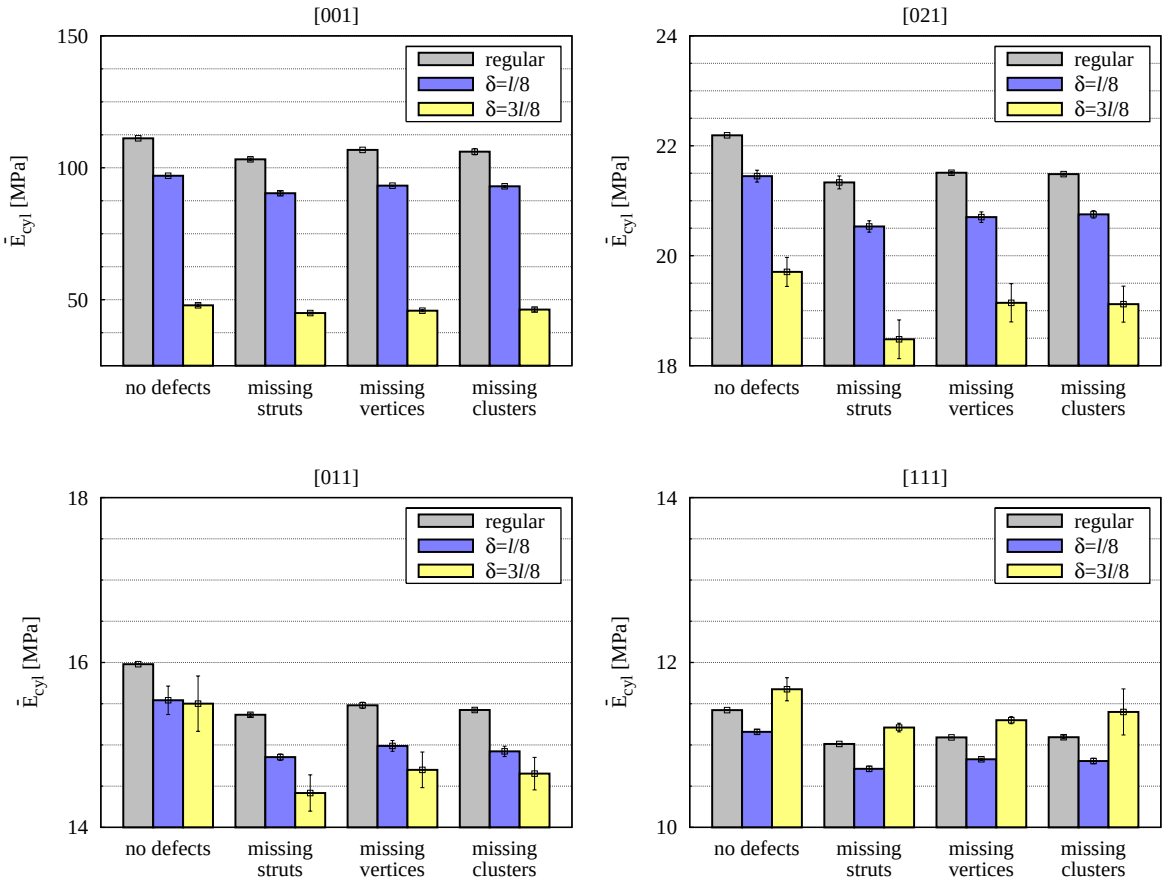

Figure 6.2 Comparison of the average Young's moduli in axial direction, $\bar{E}_{\mathrm{cyl}}$, of cylindrical SC structures with lattice orientations [001], [021], [011], and [111] as well as different defects at various levels of structural disorder, δ. The error bars indicate the standard deviation. In each case the average Young's modulus and the standard deviation are determined from five simulated structures, see Table 6.1.

difficulties occur close to or at the peak of the stress–strain curve, i.e. when parts of the structure become plastic and localization starts. Hence, in some cases (denoted by asterisks in Tables 6.2 and 6.3) the stress and strain at which the simulation stopped are regarded as the peak stress and the corresponding peak strain.

Lattice Orientation [001]

First, the structures with lattice orientation [001] are discussed, see Figure 6.7 and Table 6.2. Irrespective of the level of the structural disorder, the structures without defects sustain the highest stresses and strains, followed by structures with missing vertices, missing clusters, and missing single struts. This reflects the findings of the previous section, where it is shown that the missing single strut defects always result in the strongest decrease of stiffness, see Table 6.1.
Due to the defects the peak stresses of the regular structures are decreased by about 11-14%, whereas for the disordered structures a decrease of about 6-7% ($\delta = l/8$) and 6-8% ($\delta = 3l/8$) is observed, i.e. for disordered structures with lattice orientation [001] defects result in a smaller decrease of the peak stress than for a corresponding regular structure.

Lattice Orientation [021]

Figure 6.8 and Table 6.2 show the predicted responses for the structures with lattice orientation [021]. Similarly to the structures with lattice orientation [001], the structures without defects sustain the highest stresses and strains, followed by the structures with missing vertices. For the other defects no consistent trend regarding the order of the level of the peak stresses is observed. The missing clusters result in the lowest peak stresses for regular and slightly disordered ($\delta = l/8$) structures, whereas the missing single struts exhibit the lowest peak stresses for the highly disordered ($\delta = 3l/8$) structures. The variations of the peak stresses and strains tend to increase with increasing level of structural disorder. With exception of the structures with missing clusters and $\delta = l/8$ and structures with missing struts and $\delta = 3l/8$ the disordered structures show a slightly less pronounced reduction of the peak stresses due to the defects than the corresponding regular structures.

Lattice Orientation [011]

As in the previous cases among the structures with lattice orientation [011] the ones without defects still exhibit the highest peak stresses, see Figure 6.9 and Table 6.3, but a different behavior in terms of the peak strains is shown by the disordered structures. In the case of $\delta = l/8$ and missing vertices a larger average peak strain is predicted. Both structures with missing vertices and structures with missing clusters show a higher peak strain in the case of $\delta = 3l/8$ than the corresponding structures without defects.
No general trend regarding the reduction of the peak stresses due to the defects can be observed for the structures with lattice orientation [011]. With exception of the highly disordered ($\delta = 3l/8$) structures with missing struts and missing vertices, compared to the regular structures a slightly smaller decrease of the peak stresses is observed for the disordered structures.

Lattice Orientation [111]

Finally, the structures with lattice orientation [111] are discussed. Out of the structures with lattice orientation [111] the regular and slightly disordered ($\delta = l/8$) structures without defects exhibit the highest peak stresses and peak strains, see Figure 6.10 and Table 6.3. Out of the structures with disorder of level $\delta = 3l/8$ the structures without defects are still the ones with the highest peak stresses, but also the ones with the lowest peak strains.
With increasing levels of disorder a decreased reduction of the peak stresses caused by the defects is observed. This effect is slightly pronounced for disorder $\delta = l/8$, but very distinctive for the highly disordered structures ($\delta = 3l/8$). Due to the defects a decrease of the peak stresses of 7-11% is observed for the regular structures, whereas for the structures with disorder $\delta = 3l/8$ only a decrease of 2-3% is observed, i.e. highly disordered structures with lattice orientation [111] are more robust than the corresponding regular and slightly disordered structures.

As a general trend it is observed that for all investigated lattice orientations the peaks of the stress–strain curves of the defective structures with structural disorder of level $\delta = 3l/8$ move together. This shows that in terms of the peak stresses and its corresponding strains

the characteristic of a defect has less influence within a strongly disordered structure and that the amount of the removed material becomes the governing aspect.

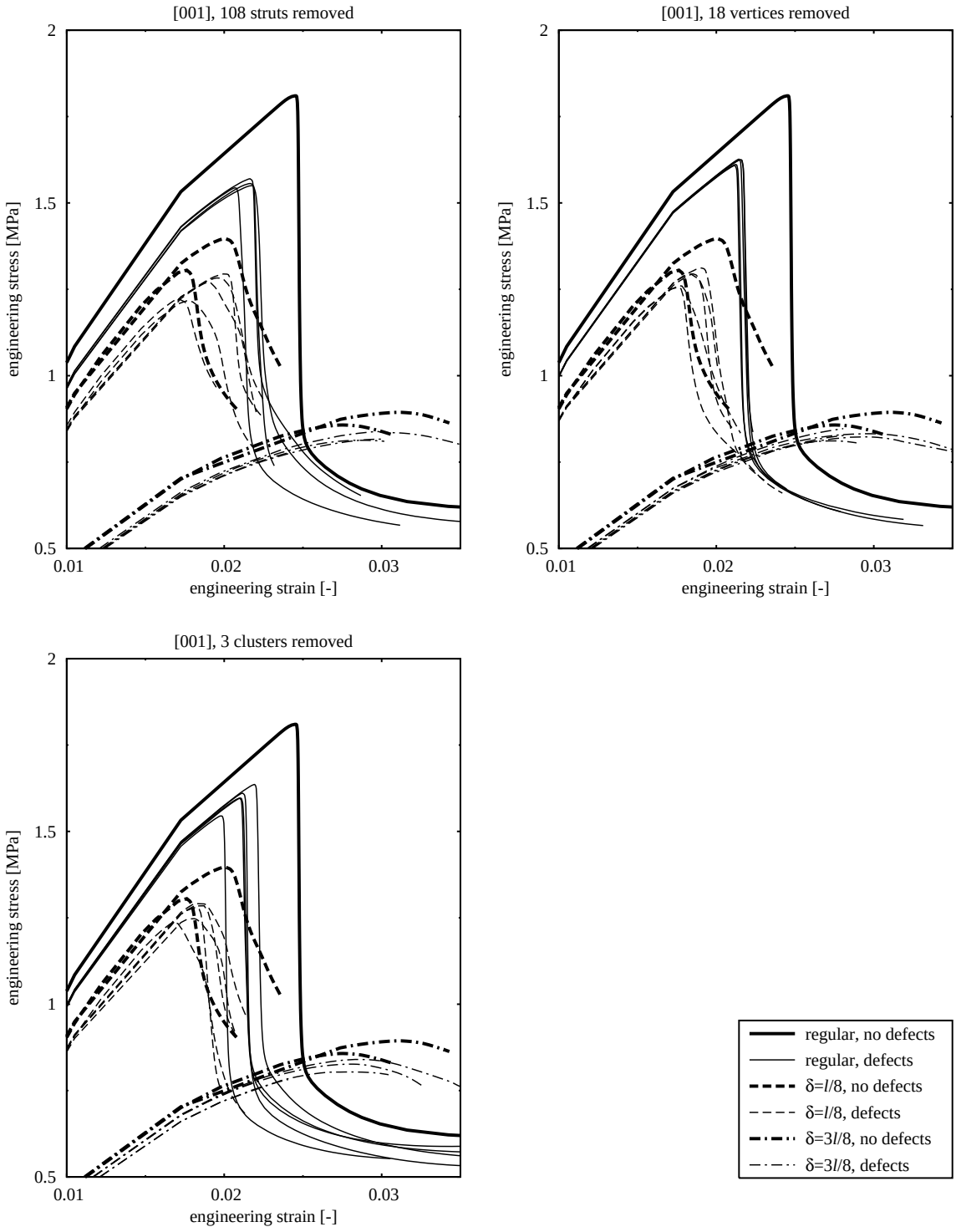

Figure 6.3 Predicted overall stress–strain curves of regular and disordered cylindrical Simple Cubic structures with and without defects and lattice orientation [001].

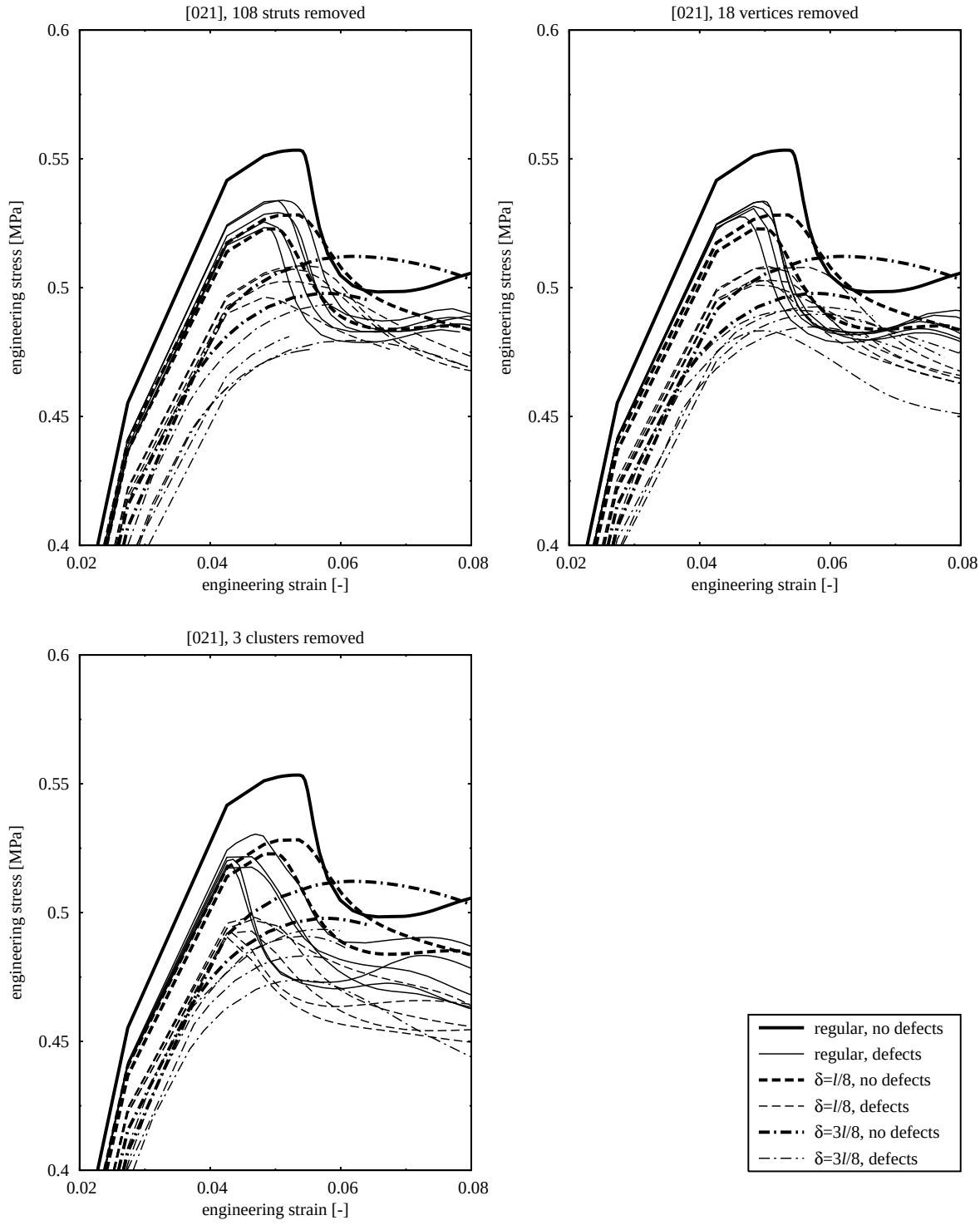

Figure 6.4 Predicted overall stress–strain curves of regular and disordered cylindrical Simple Cubic structures with and without defects and lattice orientation [021].

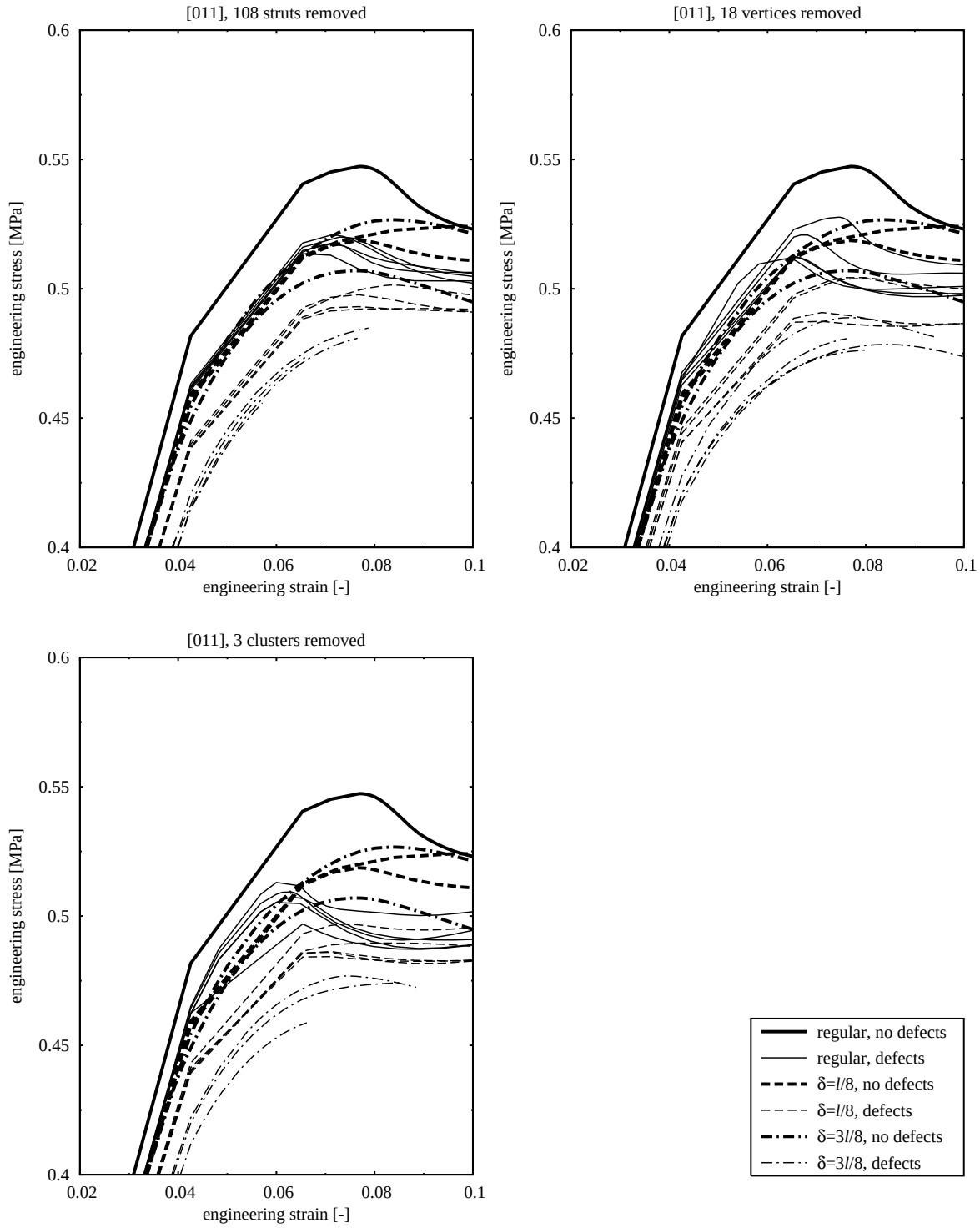

Figure 6.5 Predicted overall stress–strain curves of regular and disordered cylindrical Simple Cubic structures with and without defects and lattice orientation [011].

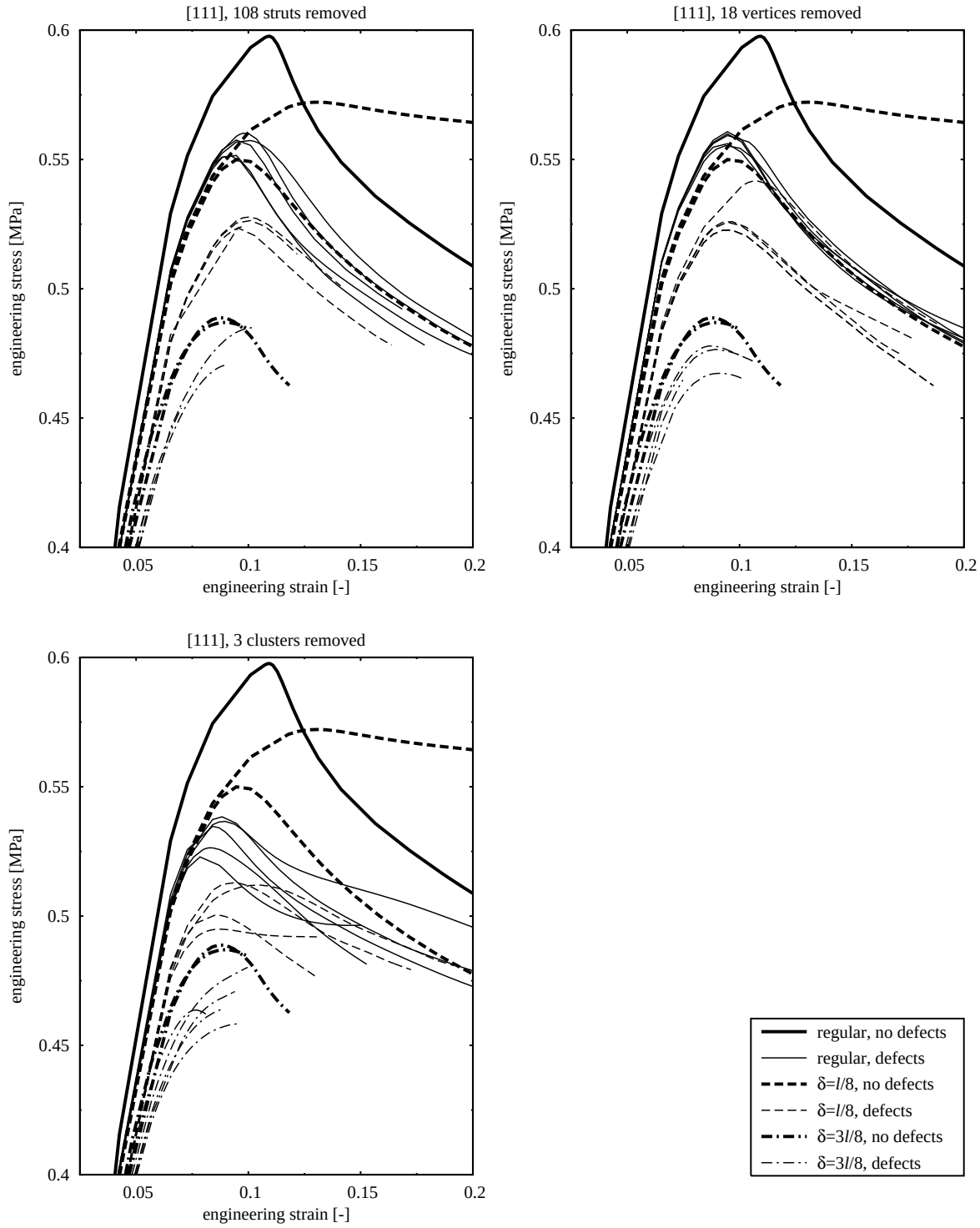

Figure 6.6 Predicted overall stress–strain curves of regular and disordered cylindrical Simple Cubic structures with and without defects and lattice orientation [111].

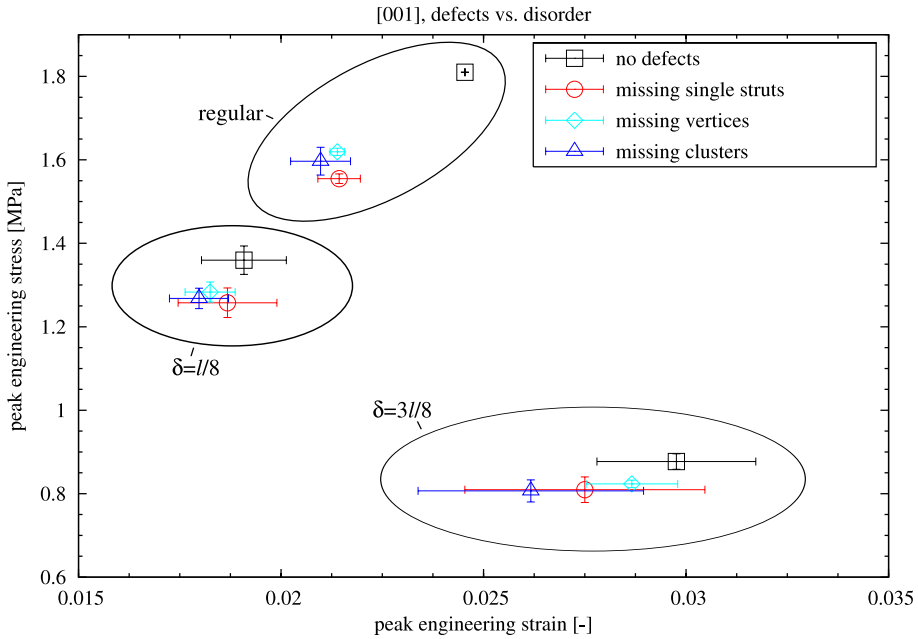

Figure 6.7 Averages of the peak stresses and the peak strains of regular and disordered cylindrical Simple Cubic structures with and without defects and lattice orientation [001]. The error bars indicate the standard deviations.

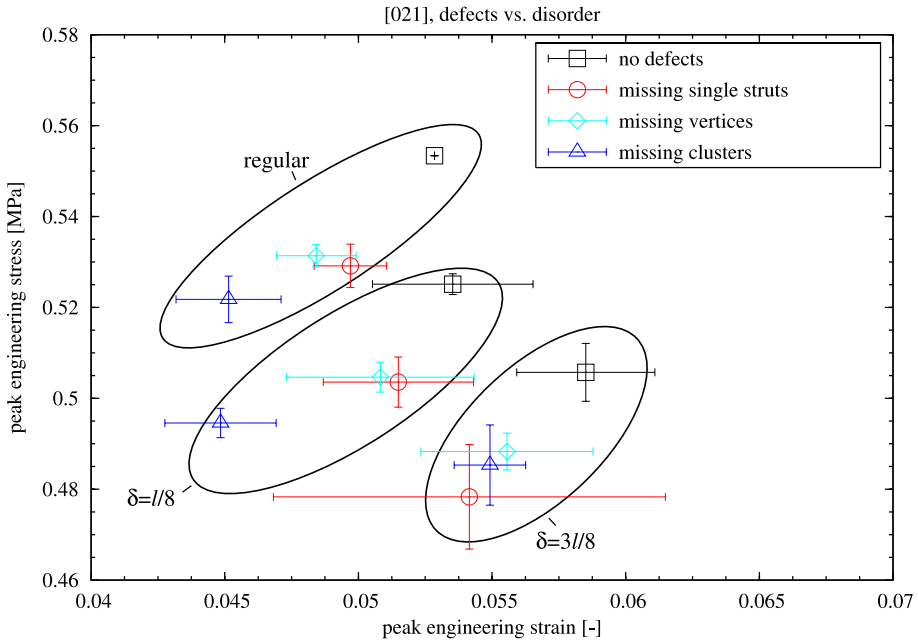

Figure 6.8 Averages of the peak stresses and the peak strains of regular and disordered cylindrical Simple Cubic structures with and without defects and lattice orientation [021]. The error bars indicate the standard deviations.

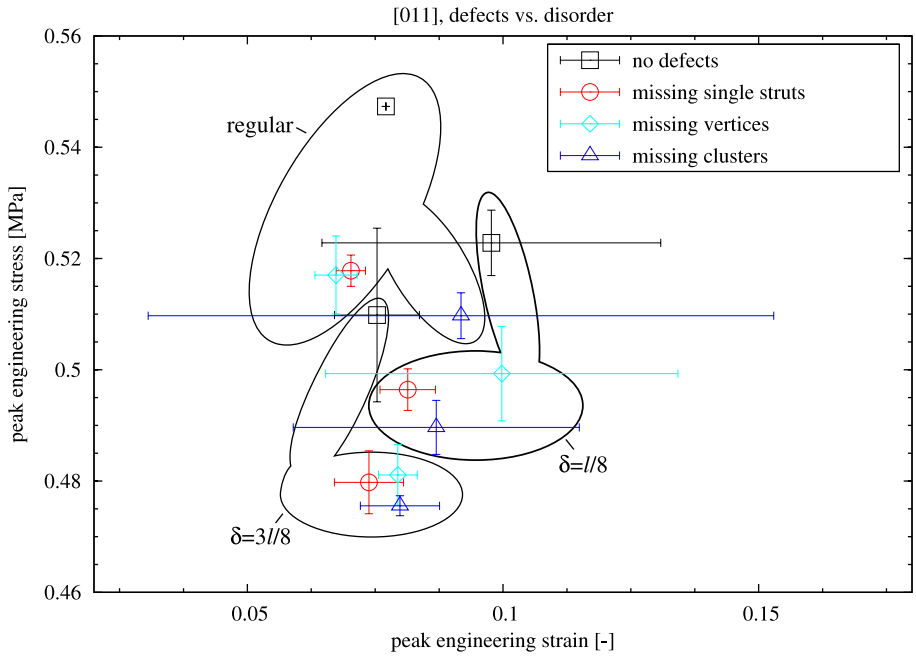

Figure 6.9 Averages of the peak stresses and the peak strains of regular and disordered cylindrical Simple Cubic structures with and without defects and lattice orientation [011]. The error bars indicate the standard deviations.

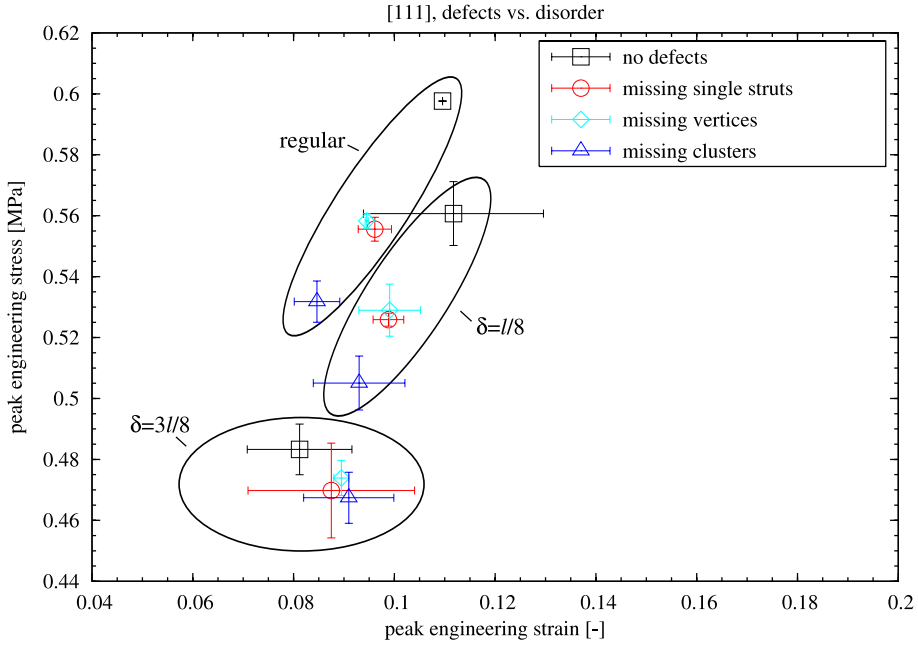

Figure 6.10 Averages of the peak stresses and the peak strains of regular and disordered cylindrical Simple Cubic structures with and without defects and lattice orientation [111]. The error bars indicate the standard deviations.

Table 6.2 Averages of the peak stresses, $\bar{\Sigma}_{33,\max}$, peak strains, $\bar{\Gamma}_{33,\max}$, and the corresponding standard deviations, s, of regular and disordered cylindrical Simple Cubic structures with and without defects and lattice orientations [001] and [021]. The percentages for the structures with defects refer to the particular structure without defects. The percentages for the structures without defects refer to the particular regular structure. Values marked by asterisks are partly obtained from results which do not exhibit a definite peak.

	regular				$\delta = l/8$				$\delta = 3l/8$			
	$\bar{\Gamma}_{33,\max}$ $\times 10^{-2}$	s $\times 10^{-2}$	$\bar{\Sigma}_{33,\max}$ [MPa]	s $\times 10^{-2}$ [MPa]	$\bar{\Gamma}_{33,\max}$ $\times 10^{-2}$	s $\times 10^{-2}$	$\bar{\Sigma}_{33,\max}$ [MPa]	s $\times 10^{-2}$ [MPa]	$\bar{\Gamma}_{33,\max}$ $\times 10^{-2}$	s $\times 10^{-2}$	$\bar{\Sigma}_{33,\max}$ [MPa]	s $\times 10^{-2}$ [MPa]
[001]												
no defects	2.454		1.810		1.908	0.105	1.359	3.405	2.976	0.196	0.877	1.848
					-22.24%		-24.89%		55.95%		-35.48%	
missing	2.143	0.052	1.555	1.136	1.868	0.122	1.258	3.531	2.750	0.296	0.809	3.060
struts	-12.66%		-14.09%		-2.13%		-7.49%		-7.59%		-7.70%	
missing	2.139	0.018	1.619	0.862	1.825	0.062	1.283	2.393	2.866	0.113	0.824	0.896
vertices	-12.84%		-10.54%		-4.37%		-5.60%		-3.69%		-6.10%	
missing	2.098	0.074	1.597	3.328	1.797	0.073	1.268	2.434	2.910	0.278	0.807	2.642
clusters	-14.53%		-11.78%		-5.81%		-6.73%		-2.22%		-8.03%	
[021]												
no defects	5.285		0.553		5.353	0.300	0.525	0.227	5.851	0.258	0.506	0.636
					1.29%		-5.11%		9.30%		-3.69%	
missing	4.970	0.136	0.529	0.476	5.149	0.281	0.504	0.194	5.415*	0.733	0.478*	1.150
struts	-5.95%		-4.38%		-3.80%		-4.10%		-7.45%		-5.42%	
missing	4.842	0.149	0.531	0.245	5.082	0.351	0.505	0.329	5.556	0.322	0.488	0.406
vertices	-8.37%		-3.98%		-5.06%		-3.90%		-5.05%		-3.45%	
missing	4.514	0.197	0.522	0.511	4.484	0.208	0.495	0.323	5.492	0.134	0.485	0.882
clusters	-14.58%		-5.71%		-16.23%		-5.81%		-6.13%		-4.03%	

Table 6.3 Averages of the peak stresses, $\bar{\Sigma}_{33,\max}$, the peak strains, $\bar{\Gamma}_{33,\max}$, and the corresponding standard deviations, s, of regular and disordered cylindrical Simple Cubic structures with and without defects and lattice orientations [011] and [111]. The percentages for the structures with defects refer to the particular structure without defects. The percentages for the structures without defects refer to the particular regular structure. Values marked by asterisks are partly obtained from results which do not exhibit a definite peak.

	regular				$\delta = l/8$				$\delta = 3l/8$			
	$\bar{\Gamma}_{33,\max}$ $\times 10^{-2}$	s $\times 10^{-2}$	$\bar{\Sigma}_{33,\max}$ [MPa]	s [MPa]	$\bar{\Gamma}_{33,\max}$ $\times 10^{-2}$	s $\times 10^{-2}$	$\bar{\Sigma}_{33,\max}$ [MPa]	s [MPa]	$\bar{\Gamma}_{33,\max}$ $\times 10^{-2}$	s $\times 10^{-2}$	$\bar{\Sigma}_{33,\max}$ [MPa]	s [MPa]
[011]												
no defects	7.709		0.547		9.772	3.314	0.523	0.588	7.536	0.830	0.510	1.560
					26.75%		-4.48%		-22.88%		-2.48%	
missing	7.025	0.285	0.518	0.281	8.136	0.542	0.496	0.373	7.378*	0.677	0.480*	0.565
struts	-8.88%		-5.39%		-16.73%		-5.05%		-2.09%		-5.90%	
missing	6.734	0.413	0.517	0.702	9.977	3.446	0.499	0.849	7.944	0.379	0.481	0.546
vertices	-12.65%		-5.53%		2.10%		-4.50%		5.42%		-5.64%	
missing	9.178	6.118	0.510	0.412	8.694	2.799	0.490	0.485	7.985*	0.775	0.476*	0.179
clusters	19.06%		-6.87%		-11.03%		-6.35%		5.97%		-6.72%	
[111]												
no defects	10.957		0.598		11.173	1.787	0.561	1.048	8.118	1.039	0.483	0.831
					1.97%		-6.18%		-27.34%		-13.80%	
missing	9.612	0.330	0.556	0.393	9.883	0.305	0.526	0.213	8.748*	1.652	0.470*	1.555
struts	-12.28%		-7.04%		-11.54%		-6.21%		7.76%		-2.80%	
missing	9.450	0.031	0.558	0.239	9.906	0.610	0.529	0.856	8.949	0.152	0.474	0.576
vertices	-13.75%		-6.59%		-11.34%		-5.65%		10.23%		-1.94%	
missing	8.465	0.452	0.532	0.678	9.300	0.909	0.505	0.887	9.095*	0.895	0.467*	0.838
clusters	-22.75%		-11.02%		-16.76%		-9.92%		12.03%		-3.28%	

6.4 Conclusions

The influences of missing single struts, missing vertices, and missing clusters on the linear elastic and nonlinear behavior of Simple Cubic structures with different lattice orientations and various levels of structural disorder are investigated in this chapter.

Regarding the linear elastic behavior it is shown that the defects always result in a decrease of stiffness. Independently of the lattice orientation and the level of disorder, the structures with missing single struts always exhibit the strongest decrease of stiffness. The highly disordered structures with lattice orientation [111] show a stiffer behavior than the corresponding regular structure. This confirms the findings of the unit cell simulations from Chapter 3, which predicted an increase of the Young's modulus in this direction for highly disordered Simple Cubic structures.

The nonlinear investigations show that for lattice orientations [001] and [111] the structural disorder results in a less pronounced decrease of the peak stresses when defects are introduced to the structures, i.e. slightly disordered structures with lattice orientations [001] and [111] are more robust against defects than the particular regular structures. For all lattice orientations the peaks of the stress–strain curves move together with increasing levels of disorder, i.e. for highly disordered structures the characteristic of a defect becomes less dominant.

Chapter 7

Summary

In the present work numerical simulations regarding the mechanical behavior of regular and irregular open cell structures are carried out with the focus on open cell structures fabricated by Rapid Prototyping.

Various Finite Element modeling concepts for open cell structures are discussed in Chapter 2. Continuum element based unit cell models are utilized as reference models and are compared to beam element based models with and without an adaptation of stiffness in the vicinity of the vertices. The accuracy of the beam element based models is found to be dependent on the structures' geometries and on the governing deformation mechanisms, respectively. However, the mechanical behavior of all structures is represented very well by the beam models, which are shown to be suitable for modeling of such structures. Constitutive characterization of four different structures in terms of density and directional dependence of their normalized Young's moduli is done and the governing deformation mechanisms are identified. Both the mechanical properties and the deformation behavior are found to be strongly dependent on the structure's architecture, as well as on the loading scenario. Finite samples are employed to investigate the influence of free surfaces and load introduction. Both influences strongly depend on the structures' architecture and on the sample orientation. The results of the simulations are compared to experimental results by means of uniaxial compression tests. It is shown that for structures with rather high

directional sensitivity imperfections play a significant role and the results deviate. For all other structures the simulation results agree very well with the experimental results.

In Chapter 3 the nonlinear behavior of open cell materials is investigated, taking into account elastic-plastic bulk material behavior, large strain theory, and deformation localization. The entire elastic tensors are predicted for six regular three–dimensional generic structures. Out of the six, the Simple Cubic and the Kelvin type structures are studied further. Various degrees of structural disorder are introduced and the effects on the linear elastic and nonlinear behavior are predicted. For the Simple Cubic structure the disorder leads to a decrease of anisotropy. The Young's modulus in the principal structure direction is reduced, while in the other directions the stiffness increases. The Kelvin type structure shows a moderate decrease of the Young's moduli in all directions due to the disorder. Then, the effect of the structural disorder on the localization of the deformation is studied under uniaxial compression. The overall stress–strain responses of finite samples are predicted for different lattice orientations. The statistical distributions of the total energy and the mesoscopic strain rates in the structures are used to assess the localization behavior. For the Simple Cubic structures localization is found for the regular and slightly disordered structures. At the highest level of disorder investigated localization is no longer occurring in Simple Cubic structures. The Kelvin structures do not exhibit a marked direction dependence in the nonlinear regime and no localization is found. Introduction of structural disorder changes the Kelvin structures towards isotropic behavior with respect to elasticity and strength. It is noted that the investigations are based on uniaxial compression load cases. For multiaxial loading scenarios additional simulations are likely to be required.

To assess the effect of the shape and the size of the simulated cuboidal finite structure models larger cylindrical samples are introduced in Chapter 4. A comparison between the different samples shapes in terms of the nonlinear overall behavior and the localization deformation is carried out. For some lattice orientations the mechanical responses deviate and different localization patterns are observed. The results show that adequate care has to be taken regarding the sample shape and size when the nonlinear mechanical behavior of cellular structures is to be determined.

In Chapter 5 new open cell structures with high overall stiffness at low elastic anisotropy are introduced. A structure, denoted as Reinforced Simple Cubic 1, turns out to be the best design. Compared to a Simple Cubic structure the elastic anisotropy has been reduced by a factor of about five and the Young's moduli in the principal directions are only 12% smaller.

Finally, the effect of three different types of defects on the linear elastic and nonliner mechanical behavior of regular and disordered open cell structures is investigated in Chapter 6. It is shown that the different classes of defects results in varying reductions of the stiffness and that structural disorder results in a less pronounced decrease of the peak stresses when defects are introduced to the structures. Furthermore it is observed that the peaks of the stress–strain curves get closer to each other with increasing level of disorder, i.e. for highly disordered structures the characteristic of a defect becomes less dominant.

Appendix A

Program Descriptions

Several software tools have been developed for the design of the structures, the generation of the FEM models, and the processing of the data for the fabrication by Rapid Prototyping. A short description of the developed tools is given in the following.

A.1 Generation of Open Cell Structures

The main function of the program `structuredesigner` is the generation of the beam element based Finite Element mesh for open cell structures. Furthermore an inputfile for visualization by raytracing is created. The topology of a structure is generated by duplication of the geometry of its base cell which is read from a file.

Synopsis:

```
structuredesigner  [-a <filename>] [-c] [-C] [-d <filename>]
                   [-D <filename>] [-E <filename>] [-h] [-l <value>]
                   [-n] [-m] [-o <value>] [-O] [-p] [-r] [-R <filename>]
                   [-s <value>] [-v] [-W] [-x <value>] [-X <value>]
                   [-y <value>] [-z <value>]
                   <basecell_filename> <jobname>
                   <xDim> <yDim> <zDim> <rotX> <rotY> <relDens>
```

Arguments:

`<basecell_filename>`	Name of the base cell definition file. For an explanation of the base cell definition file see later.
`<jobname>`	Job name for the output files to be created.
`<xDim>`	Number of base cells in x-direction.
`<yDim>`	Number of base cells in y-direction.
`<zDim>`	Number of base cells in z-direction.
`<rotX>`	Rotation angle around the x-axis.
`<rotY>`	Rotation angle around y-axis.
`<relDens>`	Relative density of the structure to be created.

Options:

`-D <filename>`, `--defects <filename>`	Reads defect definitions from file `filename` and applies them to the current structure.
`-d <filename>`, `--defectsoutput <filename>`	Writes the removed struts to a file with named `filename`. This option in combinatin with the `-d` option gives the possibility to apply the same defects to different structures.

`-E <filename>`, `--readdefects <filename>`	Reads previously generated (and stored with the `-d` option) defects from file and applies them to the current structure.
`-o <value>`, `--overridestrutradius <value>`	Set the radius of the struts directly and don't determine it from the given relative density.
`-n, --nomesh`	Avoids the generation of the Finite Element mesh. This option can save some time when only the povray files are needed.
`-m, --minimodel`	Avoids meshing struts which have been cut during the generation of the structure, and therefore have a free end. This option reduces the size of the Finite Element model for cylindrical samples, which normally exhibit a large number of struts which are only connected to one vertex.
`-C, --cylindricalsample`	Creates a cylindrical sample with a diameter of `xdim` base cells and a height of `ydim` base cells. The argument `zdim` must be given as well, but is not evaluated.
`-R <filename>`, `--removeucs <filename>`	Reads a list of coordinates from the file `filename` and removes the unit cells which enclose these positions.

`-W, --denswhole`	Use the volume of the bulk material of the whole structure for the determination of the strut radius. By default the base cell is used.
`-r, --norigid`	Do not create rigid elements in vertices. This option skips the adaptation of stiffness in the vicinity of the vertices as described in Section 2.2.1.
`-c, --cube`	Adjusts the dimensions of a cuboidal sample to fit a cube after the rotations.
`-X <value>, --perturbradius <value>`	Sets the radius of the sphere for the application of structural perturbations. To be used with the `-p` option. This value will not be scaled by the `-s` option.
`-p, --perturb`	Applies structural disorder to the structure, see Section 3.2.2. To be used with the `-X` option.
`-O, --cutplaneoverride`	Override the section planes for cuboidal samples. The `-x, -y,` and `-z` options are required to define the section planes.
`-l <value>, --beamelementlength <value>`	Sets the maximum length of a beam element.

`-z <value>, --zCut <value>`	Offset of the section plane parallel to the xy-plane. The `-O` option is required.
`-y <value>, --yCut <value>`	Offset of the section plane parallel to the xz-plane. The `-O` option is required.
`-x <value>, --xCut <value>`	Offset of the section plane parallel to the yz-plane. The `-O` option is required.
`-s <value>, --scale <value>`	The scale factor for the structure.
`-a <filename>, --alternatedensity <filename>`	Evaluates the strut radius, i.e. the relative density, from an alternative base cell definition file `filename`.

Syntax of the Base Cell Definition File

The base cell definition file describes the geometry of the base cell with points and lines. The following sample input file `sc.uc` defines a Simple Cubic base cell (see Figure 3.2).

```
point,1,0,0,0
point,2,1,0,0
point,3,0,1,0
point,4,0,0,1
line,1,2
line,1,3
line,1,4
```

Example

The following command line reads a base cell definition from the file `sc.uc`, generates a structure which consists of 6×6×6 base cells, scales it by factor 4, and rotates it by 45 degrees around the x-axis. The maximum length of a beam element is set to 0.5 and the radius is determined to achieve a relative density of 12.5%. The jobname is `sc001`.

```
structuredesigner -s 4 -l 0.5 sc.uc sc001 6 6 6 45 0 0.125
```

A.2 Generation of Rapid Prototyping Input

The program `climaker` is used for the generation of the data for the fabrication of a cellular structure by Rapid Prototyping. Therefor the structures are sliced into layers and the contours of the layers are stored using the Common Layer Interface (CLI) file format.

Synopsis:

```
climaker  [-H <height>] [-b <z-value>] [-t <thickness>] [-e
          <deflection>] [-r <radius>] [-j <jobname (*.dat)>] [-d
          <stldeflection>] [-S] [-X] [-p] [-s] [-G] [--] [-v] [-h]
```

Arguments:

`-H <height>, --height <height>`	Height of the sample.
`-b <z-value>, --base <z-value>`	z-value of the first layer.
`-t <thickness>, --layerthickness <thickness>`	Sets the thickness of the layers.

`-e <deflection>`, `--edgeDeflection <deflection>`	Sets the deflection for the curve discretization.
`-r <radius>`, `--radius <radius>`	Sets the radius of the struts.
`-j <jobname (*.dat)>`, `--job <jobname (*.dat)>`	Sets the jobname. The structure topology will be read from `jobname.dat` (must have been previously created with `structuredesigner`).
`-p`, `--noplates`	Prohibits the creation of plates at the top and the bottom of the sample.
`-s`, `--addspecimen`	Adds a tension specimen to the sample.

Bibliography

Aizenberg, J., Thanawala, M., Sundar, V., Weaver, J., Morse, D. and Fratzl, P. (2005). Materials science: Skeleton of euplectella sp.: Structural hierarchy from the nanoscale to the macroscale. *Science* 309(5732), pp. 275–278.

Albuquerque, J. M., Fatima Vaz, M. and Fortes, M. A. (1999). Effect of missing walls on the compression behaviour of honeycombs. *Scripta Materialia* 41(2), pp. 167–174.

Andrews, E. W. and Gibson, L. J. (2001). The influence of cracks, notches and holes on the tensile strength of cellular solids. *Acta Materialia* 49(15), pp. 2975–2979.

Anthoine, A. (1995). Derivation of the in-plane elastic characteristics of masonry through homogenization theory. *International Journal of Solids and Structures* 32(2), pp. 137–163.

Banhart, J. (2001). Manufacture, characterisation and application of cellular metals and metal foams. *Progress in Materials Science* 46(6), pp. 559–632.

Böhm, H. J. (2004). *CISM Courses and Lectures*, volume 464, chapter Mechanics of Microstructured Materials, pp. 41–56. Springer-Verlag, Vienna.

Charriere, E., Lemaitre, J. and Zysset, P. (2003). Hydroxyapatite cement scaffolds with controlled macroporosity: fabrication protocol and mechanical properties. *Biomaterials* 24(5), pp. 809–817.

Chen, C., Lu, T. J. and Fleck, N. A. (2001). Effect of inclusions and holes on the stiffness and strength of honeycombs. *International Journal of Mechanical Sciences* 43(2), pp. 487–504.

Christensen, R. M. (2000). Mechanics of cellular and other low-density materials. *International Journal of Solids and Structures* 37(1-2), pp. 93–104.

Currey, J. D. (2002). *Bones : Structure and Mechanics*. Princeton University Press.

Currey, J. D. (2003). The many adaptations of bone. *Journal of Biomechanics* 36(10), pp. 1487–1495.

Daxner, T. (2003). *Multi-Scale Modeling and Simulation of Metallic Foams*. Ph.D. Thesis, Vienna University of Technology, Vienna, Austria. Fortschritts-Berichte VDI, Reihe 18, No. 285. VDI Verlag, Düsseldorf.

Daxner, T., Böhm, H. J. and Rammerstorfer, F. G. (1999). Influence of micro- and meso-topological properties on the crash-worthiness of aluminium foams. In: J. Banhart, M. F. Ashby and N. A. Fleck (eds.), *Metal Foams and Porous Metal Structures*, pp. 283–288. Verlag MIT, Bremen.

Daxner, T., Denzer, R., Böhm, H. J., Rammerstorfer, F. G. and Maier, M. (2000). Simulation des elasto-plastischen Verhaltens von Metallschaum mit Hilfe von 2D und 3D Einheitszellen-Modellen. *Mater.-wiss. u. Werkst.-techn.* 31, pp. 447–450.

Deshpande, V. S., Ashby, M. F. and Fleck, N. A. (2001). Foam topology: bending versus stretching dominated architectures. *Acta Materialia* 49(6), pp. 1035–1040.

Elices, M. (2000). *Structural Biological Materials (Pergamon Materials Series)*. Pergamon.

Freyman, T. M., Yannas, I. V. and Gibson, L. J. (2001). Cellular materials as porous scaffolds for tissue engineering. *Progress in Materials Science* 46(3-4), pp. 273–282.

Gan, Y. X., Chen, C. and Shen, Y. P. (2005). Three-dimensional modeling of the mechanical property of linearly elastic open cell foams. *International Journal of Solids and Structures* 42(26), pp. 6628–6642.

Gebhardt, A. (2000). *Rapid Prototyping - Werkzeuge für die schnelle Produktentwicklung*. Hanser Fachbuch, München, 2nd edition.

Gibson, L. J. (2005). Biomechanics of cellular solids. *Journal of Biomechanics* 38(3), pp. 377–399.

Gibson, L. J. and Ashby, M. F. (1988). *Cellular Solids: Structure and Properties*. Pergamon Press, Oxford, UK.

Gibson, L. J. and Ashby, M. F. (1999). *Cellular Solids: Structure and Properties 2nd Edition*. Cambridge University Press.

Grenestedt, J. L. (1999). Effective elastic behavior of some models for perfect cellular solids. *International Journal of Solids and Structures* 36(10), pp. 1471–1501.

Guo, X. E. and Gibson, L. J. (1999). Behavior of intact and damaged honeycombs: a finite element study. *International Journal of Mechanical Sciences* 41(1), pp. 85–105.

Hohe, J. and Becker, W. (2003). Geometrically nonlinear stress-strain behavior of hyperelastic solid foams. *Computational Materials Science* 28(3-4), pp. 443–453.

Jacobs, P. F. (1992). *Rapid prototyping and manufacturing*. Society of Manufacturing Engineers, Dearborn.

Kwon, Y. W., Cooke, R. E. and Park, C. (2003). Representative unit-cell models for open-cell metal foams with or without elastic filler. *Materials Science and Engineering A* 343(1-2), pp. 63–70.

Li, K., Gao, X.-L. and Subhash, G. (2005). Effects of cell shape and cell wall thickness variations on the elastic properties of two-dimensional cellular solids. *International Journal of Solids and Structures* 42(5-6), pp. 1777–1795.

Liska, R., Schwager, F., Woesz, A., Pisaipan, A., Seidler, S. and Stampfl, J. (2003). A new route for the fabrication of biomimetic cellular materials. In: *Proceedings Radtech 2003, Berlin*, pp. 193–201.

Luxner, M. H., Stampfl, J. and Pettermann, H. E. (2004). Linear and nonlinear numerical investigations of regular open cell structures. In: *Proceedings of 2004 ASME International Mechanical Engineering Congress, Anaheim, USA, November 2004*. ASME, New York.

Luxner, M. H., Stampfl, J. and Pettermann, H. E. (2005). Finite element modeling concepts and linear analyses of 3D regular open cell structures. *Journal of Materials Science* 40(22), pp. 5859–5866.

Luxner, M. H., Stampfl, J. and Pettermann, H. E. (2006a). Numerical simulations of 3D open cell materials – Influence of structural perturbations on elasto-plasticity and deformation localization. *International Journal of Solids and Structures* Submitted.

Luxner, M. H., Stampfl, J., Woesz, A., Fratzl, P. and Pettermann, H. E. (2006b). Influence of structural disorder on the performance of 3D open cell structures. In: *Proceedings of ECCM2006, Lisbon, Portugal*. Submitted.

Marsagli, G. (1972). Choosing a point from surface of a sphere. *Annals of Mathematical Statistics* 43(2), pp. 645–646.

Moore, T. L. A. and Gibson, L. J. (2001). Modeling modulus reduction in bovine trabecular bone damaged in compression. *Journal of Biomechanical Engineering-Transactions of the ASME* 123(6), pp. 613–622.

Moore, T. L. A. and Gibson, L. J. (2002). Microdamage accumulation in bovine trabecular bone in uniaxial compression. *Journal of Biomechanical Engineering-Transactions of the ASME* 124(1), pp. 63–71.

Mosekilde, L. (2000). Age-related changes in bone mass, structure, and strengtheffects of loading. *Zeitschrift für Rheumatologie* 59, pp. 1–9.

Nye, J. F. (1985). *Physical Properties of Crystals*. Oxford University Press, Oxford, UK.

Pahr, D. H. (2003). *Experimental and Numerical Investigations of Perforated FRP-Laminates*. Fortschritt-Berichte VDI Reihe 18 Nr. 284. VDI-Verlag, Düsseldorf, Germany.

Pettermann, H. E. and Suresh, S. (2000). A comprehensive unit cell model: a study of coupled effects in piezoelectric 1-3 composites. *International Journal of Solids and Structures* 37(39), pp. 5447–5464.

Roberts, A. P. and Garboczi, E. J. (2002). Elastic properties of model random three-dimensional open-cell solids. *Journal of the Mechanics and Physics of Solids* 50(1), pp. 33–55.

Sanders, W. S. and Gibson, L. J. (2003). Mechanics of bcc and fcc hollow-sphere foams. *Materials Science and Engineering A* 352(1-2), pp. 150–161.

Shulmeister, V., Van der Burg, M. W. D., Van der Giessen, E. and Marissen, R. (1998). A numerical study of large deformations of low-density elastomeric open-cell foams. *Mechanics of Materials* 30(2), pp. 125–140.

Silva, M. J. and Gibson, L. J. (1997a). The effects of non-periodic microstructure and defects on the compressive strength of two-dimensional cellular solids. *International Journal of Mechanical Sciences* 39(5), pp. 549–563.

Silva, M. J. and Gibson, L. J. (1997b). Modeling the mechanical behavior of vertebral trabecular bone: Effects of age-related changes in microstructure. *Bone* 21(2), pp. 191–199.

Silva, M. J., Hayes, W. C. and Gibson, L. J. (1995). The effects of nonperiodic microstructure on the elastic properties of 2-dimensional cellular solids. *International Journal of Mechanical Sciences* 37(11), pp. 1161–1177.

Stampfl, J., Seyr, M. M., Luxner, M. H., Pettermann, H. E., Woesz, A. and Fratzl, P. (2004). Regular, low density cellular structures - rapid prototyping, numerical simulation, mechanical testing. In: J. Aizenberg, C. Orme, W. Landis and R. Wang (eds.), *Proceedings of 2004 MRS Spring Meeting - Biological and Bioinspired Materials and Devices*, volume 823, W8.8.

Wainwright, S. A. (1982). *Mechanical Design in Organisms*. Princeton University Press.

Wallach, J. C. and Gibson, L. J. (2001). Defect sensitivity of a 3D truss material. *Scripta Materialia* 45(6), pp. 639–644.

Williams, J. M., Adewunmi, A., Schek, R. M., Flanagan, C. L., Krebsbach, P. H., Feinberg, S. E., Hollister, S. J. and Das, S. (2005). Bone tissue engineering using polycaprolactone scaffolds fabricated via selective laser sintering. *Biomaterials* 26(23), pp. 4817–4827.

Woesz, A., Stampfl, J. and Fratzl, P. (2004). Cellular solids beyond the apparent density–An experimental assessment of mechanical properties. *Advanced Engineering Materials* 6(3), pp. 134–138.

Zhu, H. X., Hobdell, J. R. and Windle, A. H. (2000). Effects of cell irregularity on the elastic properties of open-cell foams. *Acta Materialia* 48(20), pp. 4893–4900.

Zhu, H. X., Knott, J. F. and Mills, N. J. (1997). Analysis of the elastic properties of open-cell foams with tetrakaidecahedral cells. *Journal of the Mechanics and Physics of Solids* 45(3), pp. 319–325.

Zhu, H. X. and Windle, A. H. (2002). Effects of cell irregularity on the high strain compression of open-cell foams. *Acta Materialia* 50(5), pp. 1041–1052.

Curriculum Vitae

Mathias H. Luxner

Date of Birth: 02.12.1975

Place of Birth: Zams, Austria

Citizenship: Austrian

Scientific Experience

since July 2003 **Research assistant** at the Institute of Lightweight Design and Structural Biomechanics, *Vienna University of Technology*, Vienna, Austria. Field of activity: numerical simulation of cellular solids; several industrial projects

Oct. – Nov. 2005 **Scholarship** of the Vienna University of Technology for short term studies abroad at the *Max Planck Institute of Colloids and Interfaces*, Prof. P. Fratzl, Potsdam, Germany.

Education

since June 2003 **PhD student** at the Institute of Lightweight Design and Structural Biomechanics, *Vienna University of Technology*, Vienna, Austria. Research field: numerical simulation of cellular solids.

May 2003 **Graduation** to "Diplom–Ingenieur" (MSc) for Mechanical Engineering at the *Vienna University of Technology*, Vienna, Austria.
Diploma–thesis: "Optimierung von Faserverbundbauteilen mit genetischen Algorithmen".

1994 – 2003 **Studies of Mechanical Engineering** at the *Vienna University of Technology*, Vienna, Austria.
Main topics: light weight design, numerical methods in engineering

1986 –1994 **High school** student and graduation from *BRG* high school in Imst, Austria.

Other Experience

1998 – 2001 **Incision Lasertec GmbH, Vienna**
Freelancer at the R&D department.
Field of activity: finite element simulations, design engineering